Aix*Marseille université
Socialement engagée

NNT/NL : 2021AIXM0557/071ED352

THÈSE DE DOCTORAT

Soutenue à Università degli Studi di Genova

le 25 janvier 2022 par

Carlo GUIDI

Titre de la thèse :
Systèmes de positionnement acoustique et surveillance acoustique passive des cétacés avec le télescope sous-marin à neutrinos KM3NeT

Discipline
PHYSIQUE & SCIENCES DE LA MATIERE

Spécialité
PHYSIQUE DES PARTICULES ET ASTROPARTICULES

École doctorale
Physique et Sciences de la Matière - N.352

Laboratoire/Partenaires de recherche
Aix-Marseille Université
Università di Genova
Centre de Physique des Particules de Marseille (CPPM)
Istituto Nazionale di Fisica Nucleare (INFN)

Composition du jury

Hervé GLOTIN University of Toulon	Rapporteur
Paolo PRATI Università degli Studi di Genova	Examinateur
Heide COSTANTINI Aix-Marseille Université - CPPM	Examinateur
Matteo SANGUINETI Università degli Studi di Genova	Examinateur
Vladimir KULIKOVSKIY INFN, Sezione di Genova	Examinateur
Vincent BERTIN CPPM	CoDirecteur de these
Mauro TAIUTI Università degli Studi di Genova	Directeur de thèse
Paschal COYLE CPPM	Directeur de thèse

Contents

Résumé

KM3NeT (Cubic Kilometre Neutrino Telescope) est un télescope sous-marin pour la détection des neutrinos. L'infrastructure se compose de deux sites différents: KM3NeT-ORCA (Oscillation Research with Cosmics in the Abyss) est situé en France, au large de Toulon à une profondeur de 2440 m, et KM3NeT-ARCA (Astroparticle Research with Cosmics in the Abyss) est situé en Italie, au large de Capo Passero, en Sicile, à une profondeur d'environ 3400 m. L'expérience détecte les photons produits par l'effet Cherenkov dû aux particules chargées résultant des interactions des neutrinos avec la matière. Les photomultiplicateurs sont logés dans des sphères en verre transparentes et résistantes à la pression, appelées DOM (Digital Optical Modules). Les DOM sont placés sur des structures verticales flexibles, appelées lignes, ou unités de détection (DU). Un schéma des structures du détecteur est présenté à la fig. 1.

Les principaux objectifs de KM3NeT sont l'observation des neutrinos cosmiques de haute énergie (ARCA) et la détermination de la hiérarchie des masses de neutrinos (ORCA), en exploitant les oscillations des neutrinos atmosphériques qui se produisent dans la matière pendant leur voyage à travers la Terre. La détection de neutrinos d'énergies différentes par les deux expériences est obtenue en faisant varier la densité des capteurs optiques, qui est plus élevée dans l'expérience française (énergies plus faibles, quelques GeV) et plus faible dans l'expérience italienne (énergies plus élevées, d'environ 10 TeV à environ 1 PeV). Un rôle fondamental est joué par le système de positionnement acoustique de l'expérience. Un capteur acoustique piézoélectrique est situé au pôle inférieur de chaque DOM et un hydrophone est positionné à la base de chaque DU. De plus, 3 émetteurs acoustiques autonomes, non synchronisés avec l'horloge maîtresse du détecteur, appelés Acoustic Beacons, sont disposés autour du détecteur. La fig. 2 montre la configuration actuelle de l'expérience française ORCA.

Lors du déploiement des DU dans ORCA, grâce à un système de positionnement appelé Navigation and Absolute Acoustic Positioning System (NAAPS), la position des émetteurs et des bases des lignes est déterminée avec une précision d'environ 1 m. Pendant la prise de données, cependant, un courant sous-marin (avec une vitesse typique jusqu'à 20 cm/s) peut être présent, ce qui peut décaler

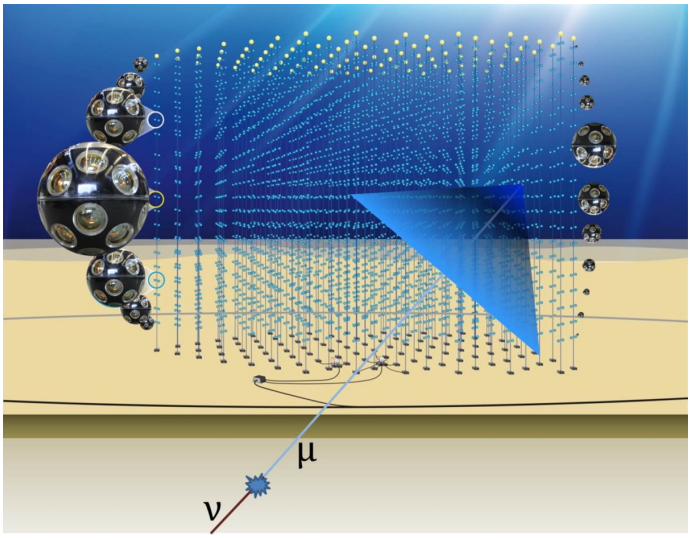

Figure 1: Schéma de la structure du détecteur KM3NeT.

les DOM les plus élevés par rapport à la verticale jusqu'à environ $7\,m$. L'objectif est d'atteindre une résolution temporelle de l'ordre de la nanoseconde afin de reconstruire correctement les traces des particules. La lumière parcourt environ $20\,cm$ dans l'eau de mer en $1\,ns$. Pour cette raison, il est nécessaire de disposer d'un système de positionnement toujours actif qui permette de connaître la position des capteurs optiques avec une précision d'au moins $20\,cm$. Les hydrophones disposés à la base des lignes peuvent également être utilisés pour détecter les sons émis par les cétacés, très présents dans les mers où se situent les deux expériences. Il est notamment possible de réaliser des études comportementales et statistiques sur différentes espèces de dauphins et de cachalots. Les individus de cette dernière espèce peuvent également être suivis en reconstruisant leur position dans le temps, en utilisant les délais entre les hydrophones pour détecter les clics très intenses que ces animaux émettent. Afin d'obtenir des trajectoires fiables, il est nécessaire de connaître la position relative des capteurs acoustiques avec une grande précision (environ $20\,cm$). La raison pour laquelle un système de positionnement efficace est essentiel est donc double. Dans cette thèse de doctorat, j'ai d'abord traité l'optimisation, les simulations et l'application à des données réelles du système de positionnement acoustique relatif KM3NeT. Par la suite, j'ai mis en place un programme d'identification automatique des clics des dauphins et des cachalots et j'ai réalisé des simulations du système de suivi des cachalots en utilisant différentes configurations d'hydrophones. Tous les programmes d'analyse ont été appliqués à des données réelles, notamment celles de l'expérience française ORCA, pour obtenir des résultats statistiques sur la présence de cétacés dans la zone. Enfin, j'ai analysé les données acoustiques de l'expérience WhaleSafe, un projet européen

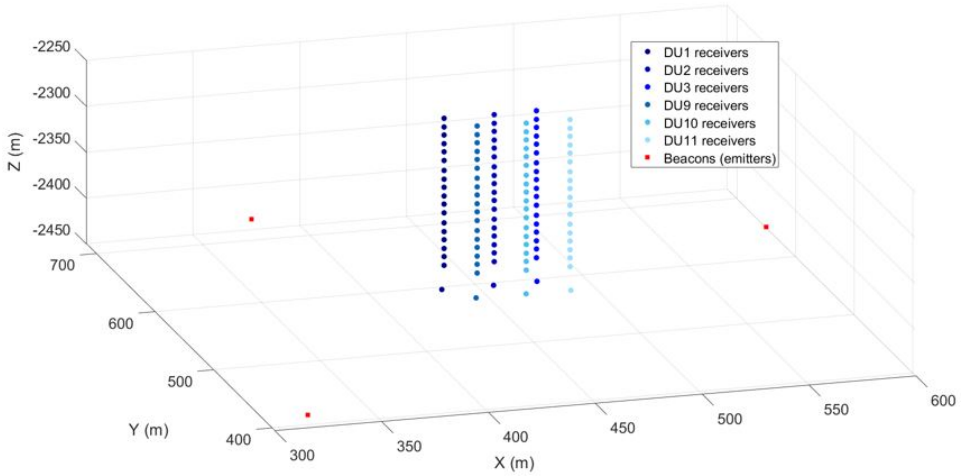

Figure 2: Configuration actuelle de l'expérience française ORCA. Les points bleus représentent les capteurs du système de positionnement, tandis que les carrés rouges représentent les émetteurs acoustiques ancrés autour du détecteur.

LIFE pour la protection et le suivi des cachalots dans la mer Ligure, en Italie, et j'ai compilé un catalogue des sons des orques stationnés dans le port de Gênes pendant environ 15 jours en décembre 2019. Pendant la première partie de mon doctorat, j'ai étudié les caractéristiques du système d'acquisition de données acoustiques KM3NeT. Le signal est traité en ligne par un logiciel, appelé Acoustic Data Filter (ADF), qui applique une fonction de corrélation croisée entre le signal connu des balises acoustiques (avec des énergies concentrées à différentes fréquences) et le signal mesuré, et attribue un facteur de qualité calculé comme le maximum de la fonction de corrélation croisée. J'ai mis en place un programme qui, sur la base de l'analyse des distributions des facteurs de qualité pour chaque capteur acoustique de l'expérience, permet de contrôler la réception des signaux sonores. La fig. 3 montre le résultat de ce programme, dans lequel le nombre de pings reçus toutes les 10 minutes par chaque capteur est mis en évidence (le nombre correct de pings émis étant 11). Actuellement, la page web de contrôle du système acoustique est publiée en ligne, fonctionnant à la fois pour ARCA et ORCA, et peut être consultée pour vérifier la bonne réception des signaux.

Il existe deux méthodes différentes pour reconstruire la position des éléments de détection en analysant les signaux acoustiques reçus des capteurs piézoélectriques et des hydrophones. La première méthode a été mise en œuvre au Laboratori Nazionali del Sud (LNS) en Italie et implique une approximation des temps d'émission (non connus a priori) et des positions des émetteurs et des hydrophones fixés sur les ancres des lignes (déterminées pendant le déploiement avec une précision d'environ 1 m). L'algorithme implique la minimisation d'une fonction qui considère

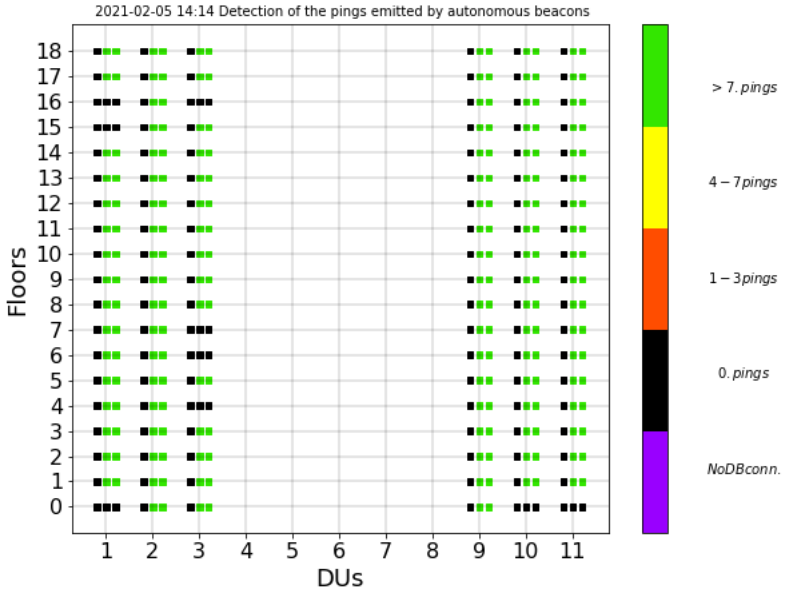

Figure 3: Tracé ORCA Acoustic Monitoring publié sur le site web de contrôle en temps réel du détecteur ORCA - Les trois colonnes de chaque ligne représentent les trois balises acoustiques. La colonne Acoustic Beacon 1 est noire car cet émetteur n'était pas actif pendant cette analyse. Les points verts signifient que la plupart des émissions acoustiques ont été détectées.

indépendamment chaque capteur et utilise la méthode des moindres carrés. J'ai mis en œuvre une deuxième méthode, plus générale et sans approximations, afin de vérifier que le résultat final était compatible avec la première méthode, plus rapide en temps de calcul. La méthode plus générale considère les positions et les temps d'émission des émetteurs comme des inconnues du système et considère les DU et les capteurs piézoélectriques de manière non indépendante. La minimisation est réalisée avec la librairie MINUIT. La fig. 4 montre la comparaison entre les deux méthodes, obtenue en effectuant des simulations du processus de reconstruction de la position relative entre les capteurs d'une seule ligne. Les deux méthodes étaient compatibles avec les incertitudes de la position déterminée pendant le déploiement de $1\,m$ et ont prouvé qu'elles garantissaient au moins la précision requise de $20\,cm$.

J'ai appliqué l'algorithme de reconstruction à des données réelles afin de tester son efficacité pendant une période de faibles courants sous-marins (lignes presque verticales) et pendant une période où un courant sous-marin non négligeable était présent (cordes inclinées). Dans les fig. 5 et fig. 6 il est possible d'observer le résultat de la reconstruction pendant deux prises de données différentes. L'inclinaison

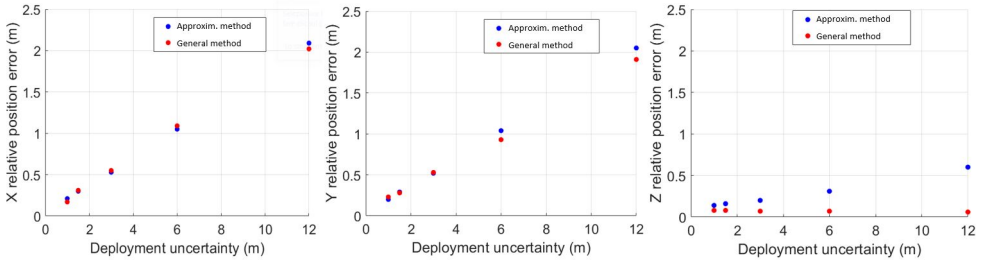

Figure 4: Erreur de position relative des coordonnées des DOM x, y et z en fonction de l'incertitude sur la position mésurée lors du déploiement - comparaison entre méthode générale et approchée.

des lignes en cas de courant important a été comparée à l'inclinaison prédite en utilisant les valeurs de courant mesurées par le courantomètre situé à proximité, confirmant la fiabilité de la reconstruction.

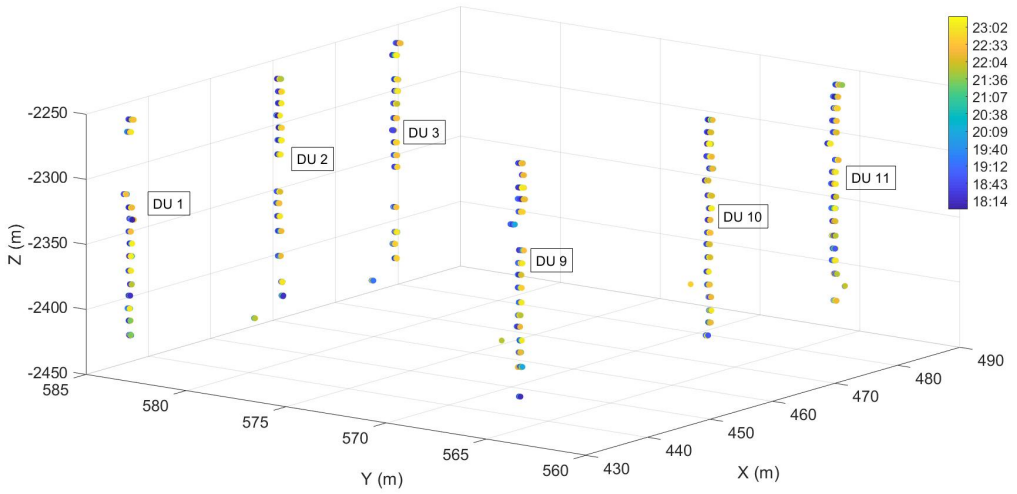

Figure 5: Positions reconstituées de 6 lignes ORCA en période de faible courant sous-marin (19/03/2020) - Les couleurs représentent l'évolution dans le temps (du bleu foncé au jaune - 6 heures au total - durée d'un run).

Pendant la deuxième partie de mon doctorat, j'ai participé à l'étude acoustique des cétacés en utilisant les signaux détectés par les hydrophones KM3NeT-ORCA. Les dauphins et les cachalots émettent des sons particuliers, appelés clics. Les principales différences entre les émissions de ces deux animaux sont l'Inter Click Interval (ICI), l'intervalle de temps entre deux clics consécutifs, et la gamme de fréquences. Les impulsions émises par les espèces de dauphins ont un ICI

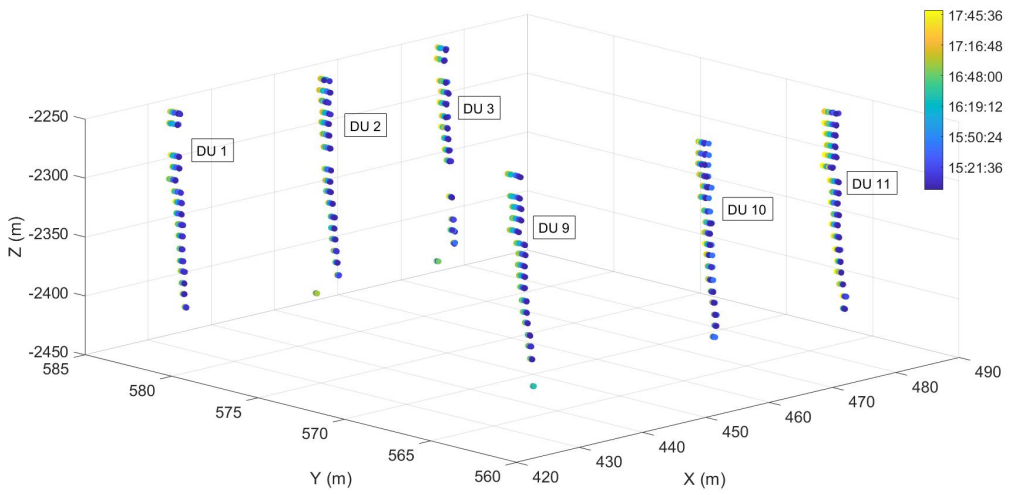

Figure 6: Positions reconstituées de 6 lignes ORCA en période de fort courant sous-marin (24/02/2020) - Les couleurs représentent l'évolution dans le temps (du bleu foncé au jaune - 6 heures au total - durée d'un run).

moyen d'environ $100\,ms$, tandis que les clics émis par les cachalots ont un ICI moyen d'environ $0.8\,s$. L'énergie des clics des dauphins est concentrée entre environ $20\,kHz$ et $50\,kHz$, tandis que la gamme de fréquences des clics des cachalots se situe entre quelques kHz et environ $20\,kHz$. A partir de ces informations, j'ai mis en place un programme automatique pour identifier les signaux émis par ces animaux, qui utilise des filtres de traitement et de nettoyage du signal, une analyse dans le domaine temporel, une analyse dans le domaine fréquentiel et quelques filtres empiriques finaux. La fig. 7 montre le taux de clics de cachalots détectés de mars 2020 à juillet 2021. L'analyse statistique a confirmé la tendance des cachalots à émettre des clics pendant la journée, mais n'a montré aucune préférence entre la nuit et le jour pour les dauphins. La distribution de tous les ICIs mesurés a été obtenue, montrant un ICI médian d'environ $0.8\,s$. Le signal unique émis par le cachalot est réfléchi plusieurs fois à l'intérieur de la tête de l'animal, ce qui donne lieu à un schéma typique d'impulsions multiples. Grâce à l'analyse de l'écart temporel entre les impulsions consécutives (Inter Pulse Interval, IPI), il a été possible d'estimer la taille de certains animaux.

La dernière étude que j'ai réalisée concernait l'implémentation de l'algorithme de reconstruction de la position du cachalot, en utilisant l'information du temps de retard entre la réception des signaux par les différents hydrophones. J'ai profité du fait que la différence entre les distances entre deux hydrophones et le cachalot est égale au produit de la vitesse du son sur le fond marin et du délai entre la

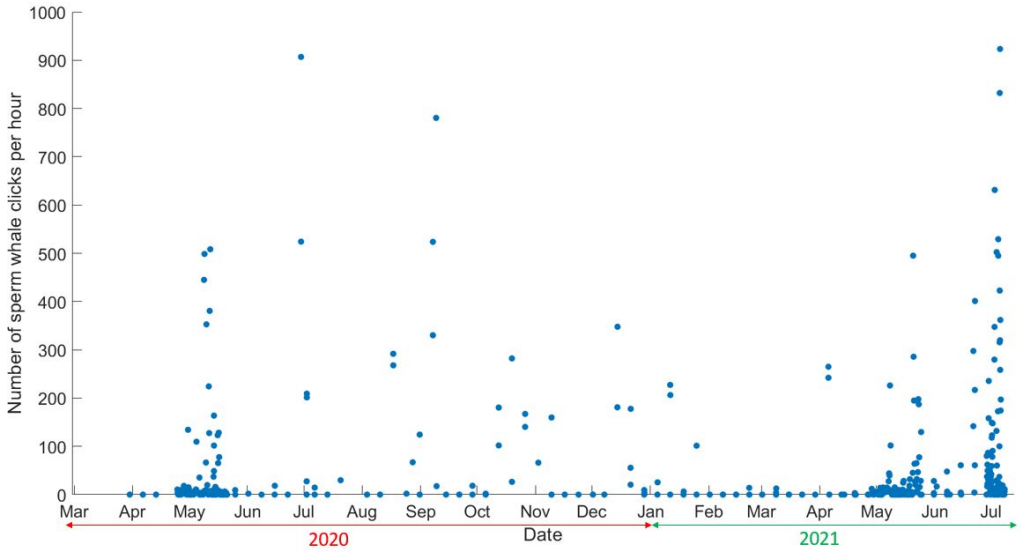

Figure 7: Nombre de clics de cachalot par heure détectés entre avril 2020 et juillet 2021.

réception du signal par les deux récepteurs acoustiques :

$$c_s \cdot \Delta t_{ij} = \sqrt{(x_i - x_w)^2 + (y_i - y_w)^2 + (z_i - z_w)^2} - \sqrt{(x_j - x_w)^2 + (y_j - y_w)^2 + (z_j - z_w)^2} \tag{1}$$

où les récepteurs i et j sont des paires d'hydrophones consécutives, x_w, y_w et z_w sont les coordonnées du cachalot, c_s est la vitesse du son sur le fond marin et Δt_{ij} est le temps de retard entre les hydrophones i et j. J'ai effectué des simulations pour identifier la meilleure configuration géométrique des récepteurs pour effectuer la reconstruction (fig. 8). J'ai montré que pour avoir une précision suffisante dans la reconstruction, il est nécessaire d'avoir au moins 16 hydrophones actifs sur les ancres des lignes. La configuration actuelle de l'expérience ORCA ne comporte que 3 hydrophones actifs. C'est pourquoi j'ai pensé à appliquer, comme test préliminaire, l'algorithme de reconstruction en utilisant également les capteurs piézoélectriques moins sensibles. Ces récepteurs ne peuvent cependant pas détecter tous les clics des cachalots, mais seulement les signaux les plus intenses. La fig. 9 montre l'amplitude en fonction du temps d'un clic de cachalot détecté par 10 capteurs acoustiques (un hydrophone et 9 capteurs piézoélectriques). Les délais indiqués sont calculés par un programme automatique que j'ai développé à cet effet. Actuellement, la principale difficulté pour la reconstruction précise des trajectoires des cachalots est due au fait que le système de positionnement, que j'ai

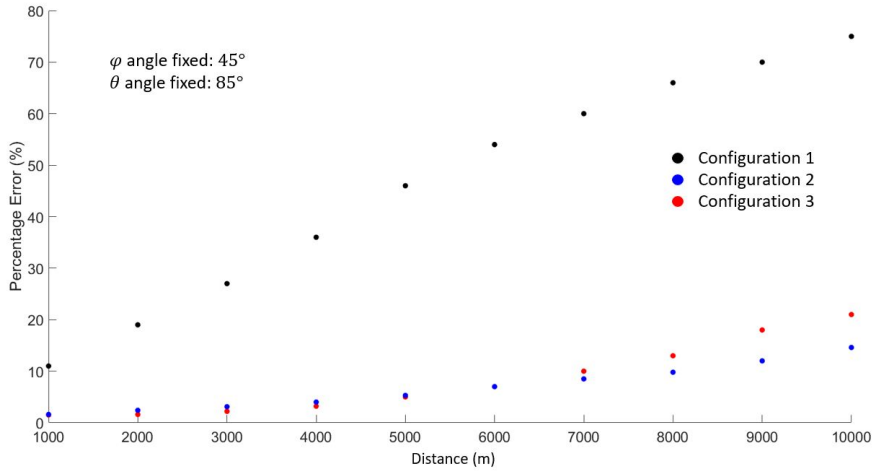

Figure 8: Résultats de la simulation : pourcentage d'erreur en fonction de la distance de la baleine (source avec angles zénithal et azimutal fixes) pour trois configurations différentes. Les points noirs font référence à une configuration avec 5 hydrophones de fond plus l'hydrophone CB, les points bleus font référence à une configuration avec 16 hydrophones de fond plus l'hydrophone CB, les points rouges font référence à une configuration avec 4 hydrophones de fond plus 2 récepteurs acoustiques à différentes altitudes (50 m et 100 m par rapport au fond marin).

décrit dans la première partie, n'est pas encore complètement opérationnel. En fait, l'émetteur 1 ne fonctionne pas en raison de problèmes de batterie et doit être remplacé. Cependant, une émission de clics de cachalot particulièrement intense a été enregistrée le 29 juin 2021 et il a été possible d'obtenir une reconstruction de la position de l'animal en fonction du temps (fig. 10).

En parallèle des activités liées à l'expérience KM3NeT, j'ai travaillé sur l'analyse des données du projet européen LIFE WhaleSafe, collectées les 12 et 13 juillet 2018 en mer Ligure. L'expérience comprenait 4 hydrophones disposés en tétraèdre sur une structure fixe et descendus à une profondeur d'environ 80 m au large de la côte de Savone, en Italie. J'ai développé une méthode pour reconstruire les trajectoires des animaux, qui ne dépend pas des influences que, surtout en été, la pression, la température et la salinité ont sur la vitesse du son. Tout d'abord, les directions d'arrivée de l'onde acoustique directe et de l'onde acoustique réfléchie par la surface de la mer sont calculées. Ensuite, la distance de l'animal au système d'hydrophones est estimée en croisant les deux lignes tridimensionnelles que forment les angles calculés à l'étape précédente. Sur la fig. 11, les trajectoires reconstruites sont visibles dans un graphique bathymétrique. Comme prévu, les animaux sont observés se déplaçant le long de la crête sous-marine, où il est facile de trouver des proies pour se nourrir.

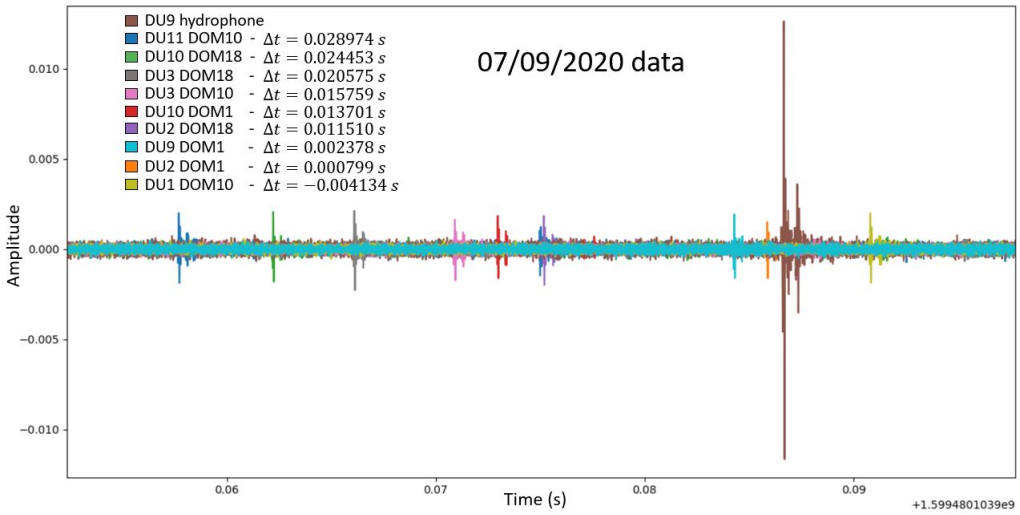

Figure 9: Clic de cachalot détecté par tous les capteurs actifs le 09/07/2020. Les temps de retard ont été calculés avec un programme automatique et comparés aux valeurs inférables du tracé.

Enfin, en raison de la présence exceptionnelle d'une famille (pod) de quatre orques dans le port de Gênes pendant le mois de décembre 2019, j'ai catalogué et catégorisé les sons enregistrés par un hydrophone fixe qui a été placé sur le fond marin à une profondeur de $10\,m$. Les émissions acoustiques ont été divisées en 3 macro-catégories : sons simples, sont composés et motifs. Au sein de chaque macro-catégorie, j'ai effectué une division plus fine, principalement basée sur l'observation des spectrogrammes.

Pendant les trois années de mon doctorat, j'ai traité tous les principaux problèmes des systèmes acoustiques visant à obtenir la position des sources sonores, en développant des simulations, des programmes d'identification du son et des algorithmes de reconstruction. Le système de positionnement relatif KM3NeT a été optimisé, atteignant la précision attendue et permettant une future reconstruction fiable des traces de particules et des mouvements des cétacés.

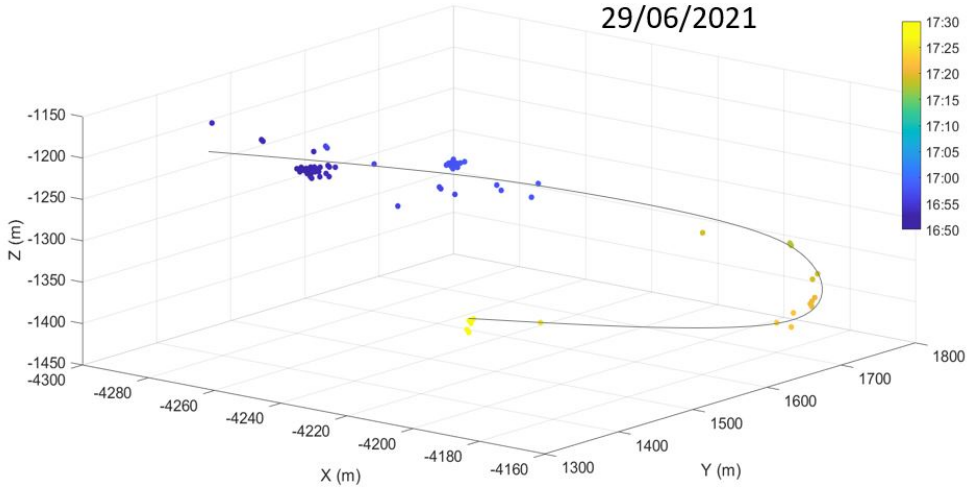

Figure 10: Reconstitution d'une trajectoire de cachalot enregistrée le 29/06/2021. Les couleurs représentent l'évolution dans le temps.

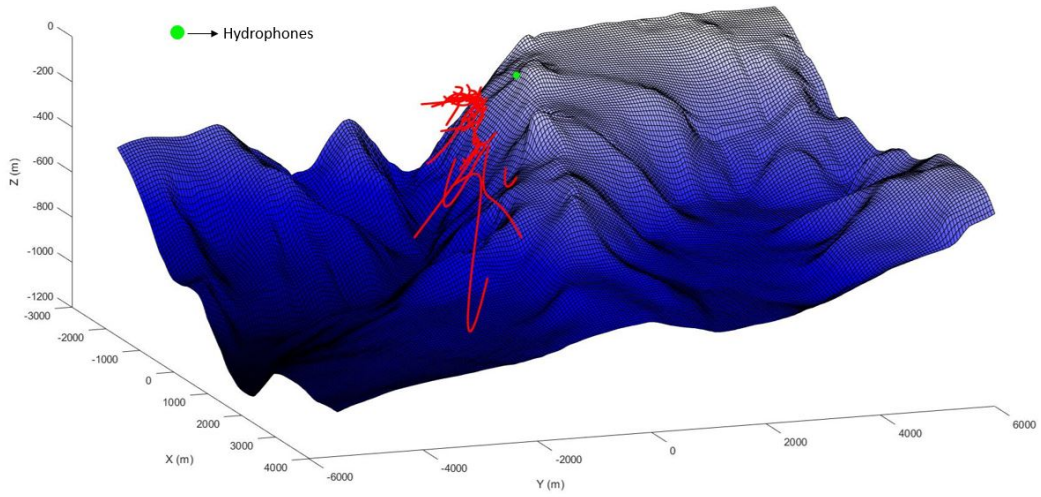

Figure 11: Diagramme bathymétrique avec toutes les trajectoires de cachalots reconstituées les 12 et 13 juillet 2018.

Abstract

KM3NeT (Cubic Kilometre Neutrino Telescope) is an underwater telescope for cosmic neutrinos detection and neutrino oscillation study. There are two detectors located in France, offshore the coast of Toulon (KM3NeT-ORCA, Oscillation Research with Cosmics in the Abyss) and in Italy, offshore Capo Passero, Sicily (KM3NeT-ARCA, Astroparticle Research with Cosmics in the Abyss).

Each experimental setup detects the photons produced by the Cherenkov effect due to charged particles, which derive from the interactions of neutrinos with matter. In order to correctly reconstruct the original neutrino direction, energy and the interaction type, it is necessary to know very accurately the position of the photomultipliers. So, acoustic systems are used to monitor the flexible detector geometry.

The detectors consist of several vertical structures, called Detection Units (DUs), along which 18 Digital Optical Modules (DOMs), each containing 31 photomultipliers, are positioned.

During the deployment of the DUs the position of all the elements is measured with an acoustic positioning system, called Navigation and Absolute Acoustic Positioning System (NAAPS), with an accuracy of about $1\,m$.

Subsequently, through a system of acoustic emitters and receivers (RAPS - Relative Acoustic Positioning System) the position of all the sensors is refined reaching an accuracy of $10\,cm$, sufficient for the reconstruction of the neutrino interaction events with the requested precision. Three autonomous emitters (called "Acoustic Beacons"), not synchronized with the master clock of telescope, are installed around the detector. On each DOM an acoustic piezo sensor is present and at the base of each line there is a hydrophone.

In this PhD thesis, I have tested and improved the methods that are used to reconstruct the positions of the optical modules and line bases of the detector. This was done by using simulations of progressively more realistic configurations and subsequently applying the developed and tested RAPS methods on real data.

In addition to the positioning of the optical sensors, the KM3NeT hydrophones can be used for different purposes. The RAPS algorithms are also used for the identification and tracking of the cetaceans. In particular, it is possible to detect

the clicks of some marine mammals, such as sperm whales, Cuvier's beaked whales and various species of dolphins. By observing the signal produced by these animals in different receivers it is possible to calculate the delay times and from these to reconstruct the position of the acoustic source.

In order to have a good accuracy in the reconstruction of the cetacean positions it is necessary to know very precisely the locations of the used receivers (in particular the hydrophones). For this reason the performance of the RAPS is very important also for this goal.

A statistical study on the presence of marine cetaceans in the area of the KM3NeT-ORCA experiment was then conducted. This type of research is very useful for studying the distribution, behaviour and habits of these animals.

My thesis work has demonstrated that the KM3NeT acoustic system, in addition to provide an accurate positioning of the optical sensors of the detector, is able to identify the sounds emitted by various species of cetaceans, in particular sperm whales, and to reconstruct their trajectory, at least when they move close to the detector (several kilometres).

A collaboration with Edgelab company was started in order to develop a mobile sound system for generic sources including marine animals. Due to the limitations imposed by the COVID-19 pandemic, the collaboration took place mostly remotely and it was not possible to carry out the tests on site.

The experience gained from my participation to similar experiments, such as WhaleSafe, a European project with the goal of tracking sperm whales in the Ligurian Sea, Italy, was particularly useful. The skills obtained analysing the WhaleSafe data taken in Summer 2018 have been successfully used to apply very similar reconstruction algorithms to the data coming from the KM3NeT hydrophones.

Numerous tracks of cetaceans have been reconstructed and it has been possible to evaluate the presence of different cetacean species and their movements.

Thanks to the KM3NeT-ORCA acoustic receiver system, located near the port of Toulon, the study of the underwater background was performed to evaluate the impact of anthropogenic activity on the marine ecosystem.

Finally, the exceptional presence of killer whale pod was observed in Genoa Pra during December 2019. I have participated in the self-organized acoustic data campaigns and performed analyses to make the repertoire catalogue of the signals in order to compare with known catalogues of killer whales around the world.

This PhD was founded by Regione Liguria (D.R. n. 1917 - 25/06/2018) and it took place in co-tutorship with the CPPM (Centre de Physique des Particules de Marseille), Aix-Marseille Université, France. The collaborative work with the French institute was assiduous throughout the duration of the PhD, but the periods of attendance were severely limited by the COVID-19 pandemic.

Chapter 1

Acoustics in sea water

1.1 Introduction

Very different applications require a thorough knowledge of the theory of acoustic waves in the underwater environment. Sound signals are used for calibration and positioning of elements (such as for the optical sensors of KM3NeT) and for the study of marine mammals. It is very difficult to observe cetaceans during their underwater life. For this reason, acoustics play a vital role in the monitoring, protection and behavioural study of these animals. In this chapter I will briefly describe the main theoretical notions on the propagation of acoustic waves in sea water.

1.2 Acoustic wave equation

The propagation of sound waves is directly linked to Newton's second law:

$$\frac{d}{dt}\vec{u} = \frac{1}{m}\vec{F} \tag{1.1}$$

where m is the mass of a moving particle, $\vec{u}$ is its speed and $\vec{F}$ is the force acting on it. A sound wave is generated by a pressure variation with respect to the equilibrium condition, operated by a force per unit area P (in N/m^2). A pressure gradient is generated in the medium and, if the force generating the displacement is removed, the particles tend to return towards the equilibrium condition. The restoring force is given by:

$$\vec{F} = -V\nabla P \tag{1.2}$$

where $V = m/\rho$ is the volume of the particle with density ρ on which the pressure gradient acts. Combining eq. 1.1 and eq. 1.2 we get:

$$\frac{d}{dt}\vec{u} = -\frac{1}{\rho}\nabla P \tag{1.3}$$

The continuity equation states that:

$$\frac{1}{\rho}\frac{d}{dt}\rho + \frac{d}{dx}u_x + \frac{d}{dy}u_y + \frac{d}{dz}u_z = 0 \tag{1.4}$$

Combining eq. 1.3 and eq. 1.4 we obtain a relationship between the variation of the medium density and the pressure gradient:

$$\frac{d^2}{dt^2}\rho = \nabla^2 P \tag{1.5}$$

We can express the pressure in a medium as a function of the density ρ and assume that the relationship is linear:

$$\delta P = c^2 \delta\rho \tag{1.6}$$

where c^2 is a positive constant of proportionality.
Consequently, we obtain:

$$\frac{d^2}{dt^2}P = c^2\frac{d^2}{dt^2}\rho \tag{1.7}$$

and combining with eq. 1.5 we obtain the general wave equation:

$$\frac{d^2}{dt^2}P = c^2\nabla^2 P \tag{1.8}$$

In spherical coordinates the wave equation becomes:

$$\frac{d^2(rP)}{dt^2} = c^2\frac{\partial^2(rP)}{\partial r^2} \tag{1.9}$$

The general solution of this equation (considering only outgoing waves) is given by:

$$rP = f(ct \pm r) \tag{1.10}$$

Eq. 1.10 relates the distance r and time t by the constant c, which represents the speed at which the disturbance travels in the acoustic medium.

We now introduce the periodic solution of the wave equation (considering only outgoing waves):

$$f(r - ct) = A(ct - r) = \cos\omega t - kr \tag{1.11}$$

where $k = \frac{2\pi f}{c}$ is called wave number and is measured in units of m^{-1}, $\omega = 2\pi f$ is the angular frequency measured in rad/s and f is the frequency, measured in Hz.

Let us consider the general solution of an outgoing planar wave that propagates only along the x axis. We assume that the velocity of the particle u satisfies the wave equation and therefore that $u = u(ct - x)$. By differentiating we get:

$$\frac{d}{dt}u(ct - x) = -c\frac{d}{dx}u(ct - x) \tag{1.12}$$

From eq. 1.3, we know that:

$$\rho\frac{d}{dt}u = -\frac{\partial}{\partial x}P \tag{1.13}$$

and consequently we obtain:

$$\frac{\partial}{\partial x}P = \rho c\frac{d}{dx}u \tag{1.14}$$

After integrating we have:

$$P = Zu \tag{1.15}$$

where $Z = \rho c$ is called acoustic impedance. This quantity in general is a complex number and it is real only if pressure and velocity of the particles are in phase. This is the typical case of plane waves, for which $P = \rho_0 cu$, where ρ_0 is the mean density of the propagation medium.

We can represent a spherical acoustic wave in this way:

$$P = \frac{A}{r}e^{i(\omega t - kr)} \tag{1.16}$$

where A is the amplitude and k the wavenumber.

Applying the eq. 1.3 to the spherical wave described by eq. 1.16, we obtain:

$$u = \frac{1}{\rho_0}\left(\frac{1}{r} + ik\right)\frac{P}{i\omega} = \frac{1}{\rho_0 c}\left(1 - \frac{i}{kr}\right)P \tag{1.17}$$

In this case the acoustic impedance is represented by a complex number. However, the imaginary part can be neglected if $kr \gg 1$. Therefore, whenever the distance r is significantly larger than the wavelength λ, we can approximate a spherical wave with a plane wave, since the speed of the particles becomes directly proportional to the sound pressure.

As we will see in sec. 4.2, the sound emissions of sperm whales have peaks of the order of kHz or a few tens of kHz. The speed of sound in water is about $1500\, m/s$. Therefore, the wavelength is of the order of metres or centimetres. The

distance at which we want to observe the animals is certainly significantly larger than the order of magnitude of this wavelength, making it possible to approximate the sound waves that reach the hydrophones as plane waves.

The acoustic emitters used in the KM3NeT positioning system (see sec. 3.3) generate sweep signals from $26\,kHz$ and $36\,kHz$ with wavelength from $\sim 4\,cm$ to $\sim 6\,cm$. Also in this case the distance between the source and the hydrophones (hundreds of metres) is significantly larger than the wavelength, so the plane wave approximation is still valid.

1.3 Acoustic wave absorption in sea water

During propagation, an acoustic wave loses intensity mainly due to two factors:

- geometric divergence,
- absorption.

The energy is spread over increasing surfaces as it moves away from the source. The intensity decreases proportionally to the inverse of the surface area. The simplest case is a point source radiating in all directions in a homogeneous and infinite medium. The transmitted energy is conserved, but it is diffused through spheres of larger radius. If we imagine two concentric spheres of radii R_1 and R_2 with the source positioned at the centre we have:

$$\frac{I_2}{I_1} = \frac{\Sigma_2}{\Sigma_1} = \frac{4\pi R_1^2}{4\pi R_2^2} = \left(\frac{R_1}{R_2}\right)^2 \tag{1.18}$$

The intensity decreases as $\frac{1}{r^2}$, while the sound pressure as $\frac{1}{r}$. Intensity losses due to geometric divergence (Transmission Loss) can be expressed in decibel (dB) as follows:

$$TL = 20 \log\left(\frac{R}{R_{1m} = 1\ m}\right) \tag{1.19}$$

Sea water is a dissipative medium since part of the transmitted energy is absorbed and dissipated due to the viscosity or chemical reactions. The decrease in intensity is proportional to the intensity itself. So, the sound pressure decreases exponentially with distance. For example, for a spherical wave, the pressure is:

$$p\,(R,t) = \frac{p_0}{R} e^{-\gamma R} e^{j\omega\left(t - \frac{R}{c}\right)} \tag{1.20}$$

The attenuation is quantified by the parameter γ (expressed in $1/m$). Conveniently, the attenuation coefficient α (in dB/m) is used, given by $\alpha = 20\gamma \log e \approx 8.686\gamma$.

In sea water, absorption is caused by three main factors:

- the viscosity of pure water (this effect increases with the square of the frequency),
- chemical dissociation of molecules of $MgSO_4$ (magnesium sulphate) for frequencies below $100\,kHz$,
- chemical dissociation of molecules of $B(OH)_3$ (boric acid) for frequencies below $1\,kHz$.

Chemical dissociation consists in the separation of ionic components in a solution, caused by local pressure variations due to the propagation of acoustic waves. This is the dominant absorption process in seawater.

There are several models that describe the absorption coefficient. One of the most used is the Francois-Garrison model [1] [2], it states:

$$\alpha = A_1 P_1 \frac{f_1 f^2}{f_1^2 + f^2} + A_2 P_2 \frac{f_2 f^2}{f_2^2 + f^2} + A_3 P_3 f^2 \tag{1.21}$$

The first two terms are related to chemical dissociation processes, the third to the viscosity of pure water. We call α the attenuation coefficient expressed in dB/km, z the depth, S the salinity in $p.s.u.$ (Practical Salinity Unit), T the temperature in $^\circ C$ and f the frequency in kHz.

The contribution of boric acid is given by:

$$A_1 = \frac{8.86}{c} \cdot 10^{(0.78pH-5)} \tag{1.22}$$

$$P_1 = 1 \tag{1.23}$$

$$f_1 = 2.8\sqrt{\frac{S}{35}} \cdot 10^{\left(4-\frac{1245}{T+273}\right)} \tag{1.24}$$

$$c = 1412 + 3.21T + 1.19S + 0.0167z \tag{1.25}$$

The contribution of magnesium sulphate is given by:

$$A_2 = \frac{21.44S}{c}(1 + 0.025T) \tag{1.26}$$

$$P_2 = 1 - 1.37 \cdot 10^{-4} z + 6.2 \cdot 10^{-9} z^2 \tag{1.27}$$

$$f_2 = \frac{8.1710^{\left(8 - \frac{1990}{T+273}\right)}}{1 + 0.0018\,(S - 35)} \tag{1.28}$$

Finally, the contribution due to the viscosity of pure water is given by:

$$P_3 = 1 - 3.83 \cdot 10^{-5} z + 4,9 \cdot 10^{-10} z^2 \tag{1.29}$$

if $T < 20\,°C$:

$$A_3 = 4.937 \cdot 10^{-4} - 2.59 \cdot 10^{-5} T + 9.11 \cdot 10^{-7} T^2 - 1.510^{-8} T^3 \tag{1.30}$$

if $T > 20\,°C$:

$$A_3 = 3.964 \cdot 10^{-4} - 1.146 \cdot 10^{-5} T + 1.45 \cdot 10^{-7} T^2 - 6.5 \cdot 10^{-10} T^3 \tag{1.31}$$

Absorption increases very rapidly with frequency. For frequencies of $1\,kHz$ or lower, the sound attenuation is below hundredths of a dB/km and is negligible for many applications. At $10\,kHz$ there is an attenuation of about $1\,dB/km$, at $100\,kHz$ it reaches tens of dB/km.

The absorption strongly depends on depth. If the frequency is high enough, the effect due to the chemical dissociation of magnesium sulfate predominates and the depth, due to the P_2 factor, plays a fundamental role. For example, in the Mediterranean Sea, the attenuation at $100\,kHz$ at the surface is $40\,dB/km$, while it drops to $30\,dB/km$ at $2000\,m$ depth.

It is possible to use the fundamental equation of passive sonar to estimate the distance at which it is possible to detect a typical click of a sperm whale, subject of interest of this study[3]:

$$L_{\frac{S}{N}} = SL - TL - NL - BW \geq \ DT \tag{1.32}$$

where $L_{\frac{S}{N}}$ is the signal to noise ratio at the receiver, SL is the sound level of the source, TL is a factor that takes into account the losses due to transmission in the medium, NL is the ambient noise density, BW is the frequency band of the noise and DT is the detection threshold. The value of the detection threshold DT represents the minimum signal to noise ratio expressed in dB below which the signal to be detected is no longer distinguishable from the noise. In our case we can choose about $10\,dB$ as the DT value, which is acceptable for systems of hydrophones similar to the KM3NeT one. The average source level (SL) of the

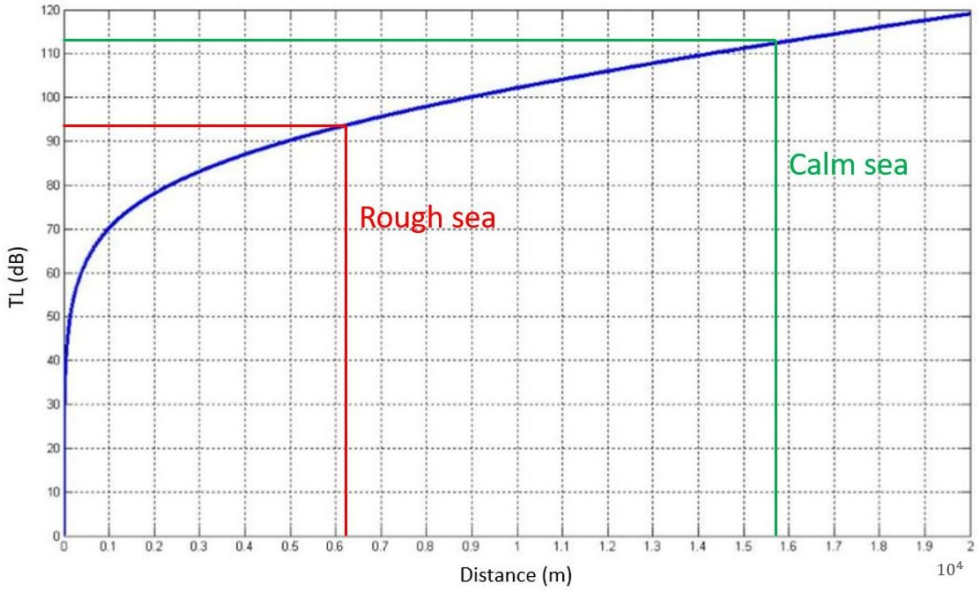

Figure 1.1: Trend of the attenuation term TL as a function of the distance in metres from the acoustic system (calm sea state).

sperm whale is about $200\,dB$. NL, which depends on the sea state according to the Douglass scale, for calm sea (degree 0) is $37\,dB$ and for very rough sea (degree 4) $57\,dB$, which correspond to the two limit conditions. Since NL represents the average spectral density in the band, we must add the contribution of the integration with respect to the frequency band of interest, which in our case is $1 - 10\,kHz$, band in which most of the energy of sperm whale clicks should be concentrated, given by the term $BW = 40\,dB$. Now imposing that the minimum $L_{\frac{S}{N}}$ is equal to DT we have:

$$TL = SL - NL - BW - DT \tag{1.33}$$

In the fig. 1.1 it is possible to observe the trend of TL as a function of the distance from the acoustic source.

$$TL_0 \;=\; 200 - 37 - 40 - 10 \;=\; 113\ dB \tag{1.34}$$

$$TL_4 \;=\; 200 - 57 - 40 - 10 \;=\; 93\ dB \tag{1.35}$$

$$TL = 10\log(r) + a\,(r-1)\cdot 10^3 \tag{1.36}$$

For a frequency of around $7\,kHz$, typical sperm whale frequency peak, the absorption coefficient is approximately $1\,dB/km$ and thus we obtain that the de-

tection range is around $6\,km$ in the case of rough sea ($TL \sim 93\,dB$) and $16\,km$ in the case of calm sea ($TL \sim 113\,dB$), as can be deduced from fig. 1.1.

1.4 Speed of sound variations in sea water

The speed of sound is formally defined as the parameter that relates pressure variations and density variations in an acoustic medium:

$$c^2 \equiv \frac{\partial P}{\partial \rho} \tag{1.37}$$

If a large change in pressure is required to have small changes in density, as in liquids and solids, the speed of sound is higher. In gases, where small changes in pressure modify significantly the density, the speed of sound is lower.

It is necessary to find a relationship between pressure and density. In general, we can assume that the volume reacts proportionally to small pressure variations:

$$dV = -\kappa\, V dP \tag{1.38}$$

where κ is called "compressibility coefficient".

Differentiating with respect to density, we obtain:

$$\frac{\partial V}{\partial \rho} = \frac{\partial}{\partial \rho}\left(\frac{m}{\rho}\right) = -\frac{1}{\rho}\left(\frac{m}{\rho}\right) = -\frac{V}{\rho} = -\kappa\, V \frac{\partial P}{\partial \rho} \tag{1.39}$$

or

$$c^2 \equiv \frac{\partial P}{\partial \rho} = \frac{1}{\kappa \rho} \tag{1.40}$$

For pure water at $20\,^{\circ}C$, we have $\kappa = 0.46 \cdot 10^{-9}\, Pa^{-1}$ and $\rho = 1000 kg/m^3$. So, we get $c = 1474 m/s$. In seawater, the speed of sound is not constant, it mainly depends on three factors:

- temperature,
- salinity,
- hydrostatic pressure (and therefore depth).

The local and temporal variations are larger in shallow waters, due to water mixing close to the surface, the influence of solar heat, currents and external agents. In deeper waters the variations due to these aspects are increasingly negligible going towards the seabed. Below a certain depth (about $1000\,m$ in open oceans and smaller depths in closed seas: for example in the Mediterranean $100 - 200\,m$)

the average temperature remains stable, decreasing very slowly with depth and varying even less horizontally.

The hydrostatic pressure increases the speed of sound with depth, due to the variation in the compressibility coefficient. With a good approximation, we can consider this linear increase and quantify it in about $0.017\,m/s$ for each metre in depth.

The hydrostatic pressure can be calculated with good precision with the Leroy formula (1969) [4]:

$$P = \left[1.0052405\left(1 + 5.28 \cdot 10^{-3} sin^2\varphi\right) z + 2.36 \cdot 10^{-6} z^2 + 10.196\right] \cdot 10^4 \quad (1.41)$$

where the pressure P is measured in Pascal, φ is the latitude in degrees, and z is the depth (in m).

Sea water is composed of a mixture of pure water and dissolved salts ($NaCl$, $MgSO_4$, ...). Salinity is defined by the mass percentage of salts and is expressed in "Practical salinity units" or $p.s.u.$, corresponding to parts per thousand of mass. In the great oceans (Atlantic, Pacific and Indian) the average salinity is about $35\,p.s.u.$, but it can vary locally due to hydrological conditions. In closed seas, the average value can be very different depending on whether evaporation is more important (for example, there is a salinity of $38.5\,p.s.u.$ in the Mediterranean Sea) or whether freshwater entry is predominant (as in the Baltic Sea, in which has a salinity of 14 psu). Salinity usually does not vary much with depth (at most $1 - 2p.s.u.$), with the exception of the most superficial layers where there can be large variations, due for example to fresh water inlets near the mouths of rivers.

In 2008 Leroy [5] found a simplified but very precise empiric formula to describe the speed of sound as a function of all the parameters of interest, expressed in m/s:

$$\begin{aligned} c = 1402.5 + 5T - \left(\frac{T}{4.288}\right)^2 + \left(\frac{T}{16.8}\right)^3 + \left[1.33 - \left(\frac{T}{81.3}\right) + \left(\frac{T}{107.2}\right)^2\right] S + \\ \left(\frac{Z}{64.1}\right) + \left(\frac{Z}{1980.3}\right)^2 + \left(\frac{z}{5155}\right)^3 + \left(\frac{Z}{18519}\right)\left(\frac{\Phi}{45} - 1\right) - \\ \left(\frac{Z}{10172}\right)^3 + \left[\left(\frac{T}{57.74}\right)^2 + \left(\frac{S}{69.93}\right)\right]\left(\frac{Z}{1000}\right) \end{aligned} \quad (1.42)$$

where ϕ is the latitude expressed in degrees.

To estimate the speed of sound in the sea, it is therefore necessary to measure the temperature and salinity as a function of depth. This operation is

typically carried out using an oceanographic instrument called "CTD profiler" (Conductivity-Temperature-Depth). However, very often it is only possible to measure the temperature with a device called XBT (eXpandable BathyThermograph) and the salinity is extrapolated from the databases or assumed constant. The function of the sound speed as a function of the depth is called Sound Velocity Profile (SVP). In the first few metres below the surface there is a homogeneous layer in which the speed of sound remains constant, because of the mixing due to the surface agitation.

Lower down there is a layer where the speed of sound increases with depth. This transition is often due to the superficial isothermal layer present during the winter months but can also be caused by very cold water near the surface (for example in the case of melting ice) or by the entry of fresh water near the estuary of rivers.

Further down there is the so-called thermocline layer, in which the speed often decreases monotonously with depth, due to the decrease in temperature. This layer can be seasonal or permanent. In the Mediterranean Sea it is highly seasonal, being almost non-existent in winter and being at an altitude of about $50 - 100m$ in the warmer months.

Below the thermocline layer there is an isothermal layer in which the speed of sound increases with depth just due to the changes in hydrostatic pressure.

The KM3NeT-ORCA acoustic sensors are located at a depth between $2240\,m$ and $2440\,m$ and the sperm whales emit echolocation clicks during the descent to the ridges of the submarine canyons and during the ascent to the surface in a depth range between around 100 and 1500 metres below sea surface. The path taken by the sound waves, therefore, lies below the thermocline layer in the Mediterranean Sea and the speed of sound depends almost exclusively on the hydrostatic pressure:

$$c\,(z) = c_0 + g\,(z - z_0) \tag{1.43}$$

where g is the velocity gradient, c_0 is the sound speed at a certain z_0 reference depth.

Sound waves travel according to the Snell's law, which takes the following form:

$$\cos\beta(z) = \frac{c\,(z)}{c_0}\cos\beta_0 = \left(1 + \frac{g}{c_0}\,(z - z_0)\right)\cos\beta_0 \tag{1.44}$$

For each circle in the plane $(x,\, y)$, the general relationship between the Cartesian coordinates of a point, the slope angle β (defined by the tangent to the circle), and the radius R_c is:

$$z - z_0 = R_c\,(\cos\beta - \cos\beta_0) \tag{1.45}$$

where $(x_0,\, y_0)$ and β_0 define a reference point along the circle. The cosine of the angle for a given point of the circle can be expressed as a function of z in this way:

$$\cos\beta(z) = \cos\beta_0 + \frac{z - z_0}{R_c} \tag{1.46}$$

Eq. 1.45 is formally similar to eq. 1.44. So, in the case of a linear velocity profile, the sound waves travel through circles of radius R_c given by the starting angle β_0 to a depth where the speed of sound has a certain value c_0:

$$R_c = \frac{c_0}{g\cos\beta_0} \tag{1.47}$$

When $\cos\beta_0 = 1$ we obtain the minimum value of the radius R_c, approximately equal to $80\,km$.

As we will see in detail in the sec. 4.3, to reconstruct the position of the animal it is necessary to calculate the delay times between the arrival of the sound wave at the different hydrophones. If we compare the difference between the straight paths between source and hydrophones and the difference between the curvilinear paths due to the SVP, we get a discrepancy of a few metres, comparable with the size of the animal that emits the sounds. For this reason, we can consider the effects due to the variation of the speed of sound with depth to be negligible both for acoustic positioning and cetaceans detection.

1.5 Doppler effect

The doppler effect consists of a shift in the frequency of the sound signal due to a change in the length of the path between the source and the receiver during the transmission of the wave, caused by the changing relative position between source and receiver.

Let's consider a Dirac delta-shaped pulse of period T, directed towards a receiver at a distance D. If D does not vary with time, the receiver will pick up the pulse after a time $t = D/c$. The period of the signal, therefore, is not modified, and the recorded frequency remains $f_0 = 1/T$.

If instead D decreases, for example, with respect to time ($D(t) = D - v_r t$), due to the relative speed between source and receiver v_r, the interval between two pulses will be varied.

If the first pulse (transmitted at time $t = 0$) arrives at time $t_1 = D(t_1)/c$, the second pulse (transmitted at time $t = T$) will arrive at time t_2, given by:

$$t_2 = T + \frac{D(t_2)}{c} = T + \frac{D\,(t_1) - v_r(t_2 - t_1)}{c} \tag{1.48}$$

The interval between the receptions of the two signals will be:

$$t_2 - t_1 = \frac{T}{1 + v_r/c} \tag{1.49}$$

and therefore it will be lower than T. The frequency seen by the receiver will therefore be changed to:

$$f = \frac{1 + v_r/c}{T} = f_0 \left(1 + v_r/c\right) \tag{1.50}$$

In our specific case of Passive Acoustics for the detection of sperm whales, the doppler effect is negligible. If we assume a sperm whale moving at $15\,km/h$ with respect to the hydrophones there would be a variation of around $27\,Hz$ for a $10\,kHz$ signal, therefore about $0.3\,\%$.

1.6 Conclusions

The KM3NeT experiment uses acoustics to calibrate the position of all the elements of the detector and to detect the sounds emitted by cetaceans in order to track their movements. As has been pointed out, for these purposes the effects due to absorption in seawater can be neglected. The variations of the speed of sound as a function of depth can be relevant for the reconstruction of the position of the KM3NeT optical sensors, but at the depth at which the experiment is located (around $2400m$) the functional trend is known and mostly depends on the hydrostatic pressure. A correction, therefore, can be easily applied. As has been observed, however, it is possible to completely neglect this effect for the reconstruction of the sperm whale routes.

Chapter 2

KM3NeT – general description

2.1 Introduction

KM3NeT (Cubic Kilometer Neutrino Telescope) [6] is an underwater telescope for the detection of cosmic neutrinos and for neutrino physics. Its two detectors are located at two different sites in the Mediterranean Sea: KM3NeT-Fr (offshore the coast of Toulon, France) and KM3NeT-It (off Capo Passero, Sicily, Italy).

The French site hosts the KM3NeT-ORCA (Oscillation Research with Cosmics in the Abyss) detector, located $40\,km$ offshore at a depth of $2440\,m$, while the Italian site hosts the KM3NeT-ARCA (Astroparticle Research with Cosmics in the Abyss) detector, located $100\,km$ offshore at a depth of about $3400\,m$.

The construction of the infrastructure of the two experiments began in 2012 and the first data from a partially installed detector has been collecting since 2016.

The main goals of KM3NeT are the observation of high-energy cosmic neutrinos and the determination of the mass hierarchy of neutrinos, exploiting the oscillations of atmospheric neutrinos that occur in matter during their travel through the Earth.

The motivation to build an experiment such as KM3NeT arises from two important results obtained from other experiments:

1. From 2013 to 2016 the IceCube experiment showed evidence of cosmic neutrinos coming both from above and below the horizon with energies ranging from about $10\,TeV$ to over $1\,PeV$ [7]. IceCube has reconstructed 54 events with energy higher than $30\,TeV$, 39 of the "cascade" type and 14 of the "track" type. The neutrino telescopes better discriminate the upgoing neutrinos from the background so the event selection is enhanced for the Southern Hemisphere.

2. The Daya Bay [8] (2012 [9] and 2016 [10]) and RENO [11] (Reactor Experiment for Neutrino Oscillations) (2012) experiments managed to give an

accurate estimate of one of the fundamental parameters of the mixing matrix between the neutrino states, the mixing angle between the first with the third neutrino.

KM3NeT-ARCA aims to collect a large amount of data to significantly increase the statistics available and thus be able to identify the position of astrophysical neutrino sources, in particular from galactic origin (for details see sec. 2.4.1).

Starting from the important measurements of Daya Bay, RENO and other similar experiments, the ORCA experiment aims to determine the neutrino mass hierarchy (for details see sec. 2.4.2).

In particular, in the ARCA configuration the Optical Modules are more spaced both horizontally and vertically in order to detect neutrinos of very high energy (TeV–PeV energy range) and therefore respond to the first of the two main objectives. The ORCA experiment, on the other hand, will have a higher density, useful for detecting atmospheric neutrinos (in the $2 - 30\,GeV$ energy range) and studying problems relating to neutrino oscillations.

An experiment with similar purposes, called ANTARES [12] (Astronomy with a Neutrino Telescope and Abyss environmental RESearch), progenitor of KM3NeT, was built at a site near ORCA, between 2006 and 2008 and it is still taking data after more than a decade. The experience gained from the construction of ANTARES and from the analysis of the data collected was fundamental for the implementation of a more performing and powerful system, in KM3NeT.

In this chapter, after a general description of the design and technology of the detector, I will discuss the main physics goals of the two KM3NeT configurations (ARCA and ORCA).

2.2 Detector design and Technology

KM3NeT detection of neutrinos is based on the Cherenkov light produced by charged relativistic particles that arise from the interactions of neutrinos with matter. An array of optical modules in the transparent medium can be capable to detect this light and reconstruct the events topology. Therefore, the goal of KM3NeT is to equip the sea water volume with optical modules, reaching a density sufficient to reconstruct the neutrino interactions.

The great depth at which the experiment is located ($2440\,m$ for ORCA and $3400\,m$ for ARCA) presents a dark environment, no light from the surface is detected. An easily recognizable background comes from the light produced by the bioluminescence of small fish, algae and microorganisms. The great depth is also useful for shielding the detector as much as possible from cosmic particles coming from above and their secondary atmospheric particles.

The photomultipliers are hosted in transparent pressure-resistant glass spheres, called DOMs (Digital Optical Modules). DOMs are placed on flexible vertical structures, called strings, or lines, or Detection Units (DUs).

The Detection Units (see fig. 2.2, left) are formed by two thin Dyneema ropes to which the DOMs are connected by a titanium collar. Each string supports 18 DOMs.

DOMs (see fig. 2.3, left) are formed by two separate hemispheres. The two hemispheres are held together before deployment by a pressure decrease to about $200\,mbar$ inside the sphere. 31 photomultipliers (PMTs) (See fig. 2.3, right) are positioned on the surface of the DOMs in 5 rings of 6 sensors plus a single sensor pointing downwards. Around the PMT a reflector ring increases the photon collection efficiency by $20 - 40\,\%$.

The optical module also contains three calibration sensors: one LED nanobeacon, one compass-tiltmeter and a piezoelectric acoustic sensor glued to the inner surface of the sphere.

Several distances between the DOMs and between the DUs have been studied in order to obtain a different density of the optical sensors. In this way neutrinos of lower energies ($\sim GeV$), as it happens in ORCA, or higher energies ($\sim TeV$ and more), as it happens in ARCA can be efficiently detected.

KM3NeT-ARCA will count two building blocks, each consisting of 115 DUs. The signal is transported via one electro-optical cable with 24 optical fibres, connected to four primary Junction Boxes. Each primary Junction Box is connected to 3 secondary Junction Boxes, which can be connected to 12 DUs. The main electro-optical cable is connected to a power supply ($50\,kVA$) located on the shore, in Porto Palo di Capo Passero. On average the space between the strings in ARCA is $95\,m$.

ORCA will consists of 1 building block of 115 DUs. The signal is transported

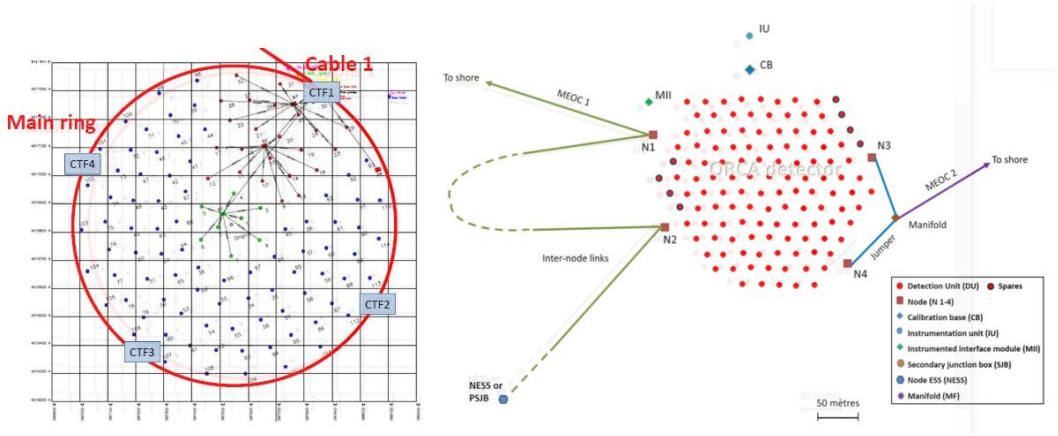

Figure 2.1: Layout of an ARCA building block (left) and layout of the full ORCA array (right).

via 2 electro-optical cables with 36/48 optical fibres, connected to 5 Junction Boxes. Each Junction Box has 8 connectors, each of which can be connected to 4 DUs in series. Some of these may include a Calibration Unit (laser beacons and / or hydrophone acoustic emitters). In ORCA the power is transferred in Alternating Current to be converted in Direct Current at each DU level. The electro-optical cables are connected to a power supply ($92\,kVA$). The control room is located at the Institute Michel Pacha, La Seyne-sur-Mer. On average, the space between the strings in ORCA is $20\,m$.

In ARCA the lines are about $700\,m$ high and the distance between the DOMs is about 36m, starting from $80\,m$ above the seafloor. In ORCA, on the other hand, the lines are about $200\,m$ high and the distance between the DOMs is about $9\,m$, starting from about $40\,m$ above the seafloor. The main electro-optical cable is connected to the ropes and contains 2 copper wires for power transmission and 18 optical fibres for data transmission.

All analog data recorded by PMTs that exceed a certain threshold are digitized and then sent to shore where they are analyzed in real time. A dedicated software selects the physical data from the background data.

In parallel, the acoustic data are also processed, useful for the positioning system and for bioacoustics analysis. These data represent approximately one third of the optical data.

Before deployment, the DOMs are located inside cavities set up in a structure used as a launcher (see upper part of fig. 2.2, right) and an anchor (see lower part of fig. 2.2, right). The anchor houses an interlink cable and the base container. The line is lowered to the sea bottom by the deep winch cable of the deployment ship ended by a releasable acoustic transponder which, thanks to the combined

Figure 2.2: The Detection Unit (left) and the launcher vehicle (right).

action with emitters present on the surface vessel, allows to determine the position of the base of the string with an accuracy of $1\,m$.

Moreover, during deployment, a Remote Operated Vehicle (ROV) is used to connect the interlink cables from the base of the string to the Junction Box.

Once the connections are made, the line is firstly released from the winch cable, then the launcher is released and due to its positive buoyancy it begins to slowly rise up freeing the DOMs. At the end of the operation the launcher is recovered from the surface vessel.

Figure 2.3: A Digital Optical Module (left) and a photomultiplier (right).

2.3 KM3NeT acoustic hardware [13]

As we will see in sec. 3.3, the Relative Acoustic Positioning System (RAPS) is composed of at least 3 emitters (Acoustic Beacons), positioned around the detector, a hydrophone placed on the base of each DU and a piezoelectric sensor placed on the bottom hemisphere of each Digital Optical Module.

2.3.1 Piezoelectric sensors

A piezoelectric sensor is a device able to measure changes in pressure converting them to an electrical charge. Inside the transducer, infact, a piezoelectric crystal is present, that proportionally converts in electric signal the mechanical stresses caused by the propagation of the acoustic waves. These crystalline materials polarize generating a potential difference when subjected to mechanical deformation.

The KM3NeT piezoelectric sensors (fig. 2.4) have a sensitivity of $-160 \pm 6\,dB\,re\,1\,V/\mu Pa$ at $50\,kHz$ with $\pm 3\,dB$ variation in the range $10\,kHz - 70\,kHz$.

Power spectral density is shown in fig. 2.5. In the range between $10\,kHz$ and $80\,kHz$ the behaviour is very flat. Above $80\,kHz$ the power spectral density drops rapidly. For frequencies below $5\,kHz$ the noise increases considerably. For this reason, a high pass filter will be required to avoid signal saturation. The peak at $0\,Hz$ is due to a DC offset of about $3 - 4\,mV$ at the analogue input of the ADC (Analog to Digital Converter). It is not significant compared to the full input range of $4\,V$ and can be easily removed during the analysis. The sensitivity of sensors strongly depends on the operation conditions. Precise sensitivity measurements were then performed on some piezos installed on the DOMs in a calibration water pool facility.

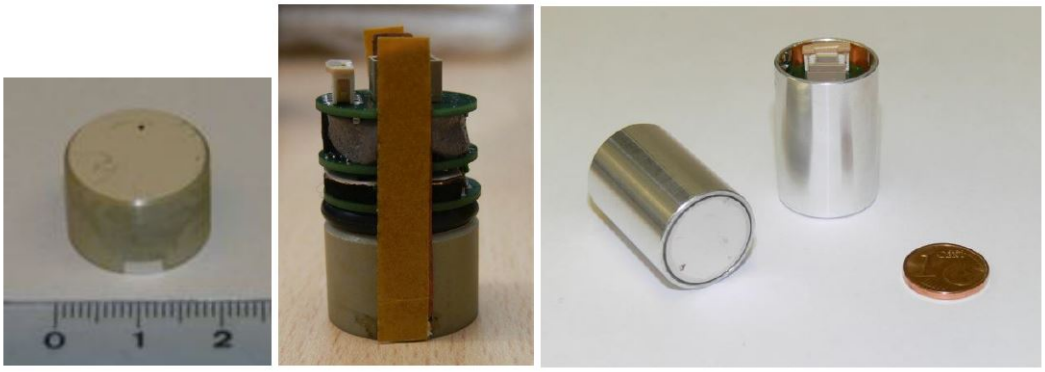

Figure 2.4: A piezo ceramic; The integrated piezo and electronics before insertion into the aluminum tube; Fully assembled prototypes of the piezo sensors with digital readout.

The time response of the piezo, the delay time between the reception of the signal and the time stamp by CLB, is a parameter that depends on the electronics and configuration of the FPGA and it is the same for all piezos. This parameter has also been studied with tests carried out in the water pool facility and it has been estimated to be around $170\,\mu s$.

Tests have shown that piezos are sensitive to electromagnetic interference when the photomultipliers on DOMs are powered. These interferences generate spikes in the spectrum at specific frequencies, as can be seen in figure fig. 2.6. This does not create problems for positioning since the beacon signal (between $20\,kHz$ and $40\,kHz$) is a high amplitude sweep signal. There are no significant problems even for the clicks of the cetaceans. In fact, for example, sperm whales typically emit clicks with a frequency between a few kHz and $18/20\,kHz$.

2.3.2 Hydrophones

The selected hydrophones (DG0330) are produced by Colmar s.r.l. [1] and consist of a spherical piezo-ceramic element, read-out by an analogue board with two gain options ($+46\,dB$ and $+26\,dB$). The audio stream is sampled from a commercial 24-bit stereo ADC and converted to the AES (Advanced Encryption Standard) protocol using a Digital Interface Transmitter (DIT). The sampling frequency of the device is $195.3\,kHz$. In fig. 2.7 an image of the hydrophone is shown.

The sensitivity of the hydrophones, placed at the base of each Detection Unit, is approximately $-173\,re\,1\,V/\mu Pa$ and the change in sensitivity as a function of pressure is less than $1\,dB$. The typical sensitivity curve is shown in figure fig. 2.8

[1] https://colmaritalia.it/it/home/

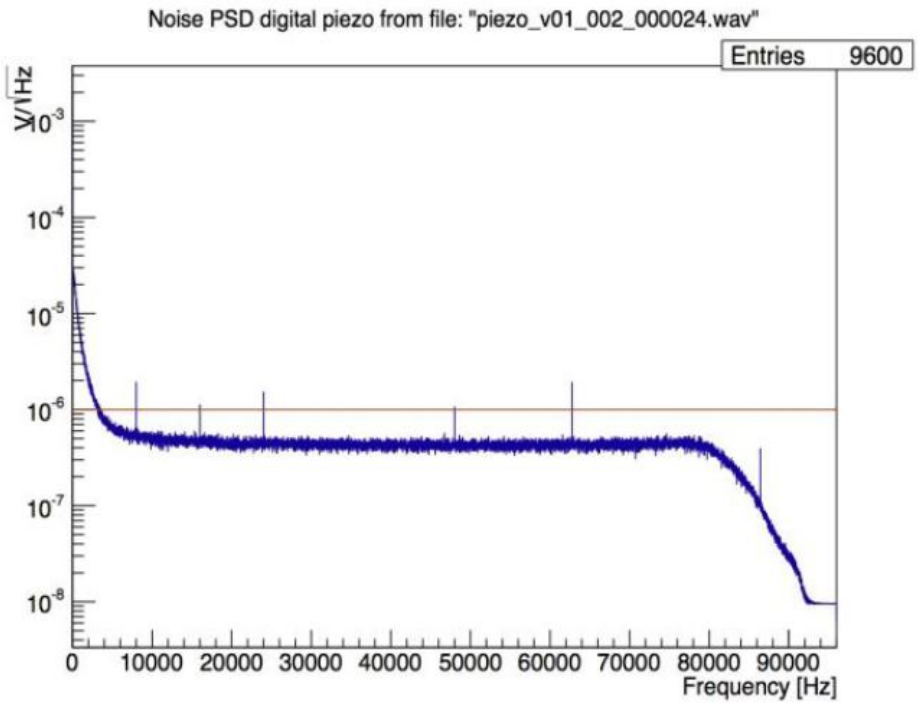

Figure 2.5: Power spectral density of a prototype digital piezo sensor. The red line indicates the requirement of a spectral noise density less than -120 dB re 1 V^2/Hz between 10 and 70 kHz. A few spikes are seen, which are mostly derived from the digitization rate.

The time latency of the electronics of the hydrophones was measured and corresponds to $50.65 \pm 0.25\,\mu s$ for the low gain channel and $50.71 \pm 0.25\,\mu s$ for the high gain channel. The intrinsic noise of the hydrophones was estimated with a dedicated setup for the two channels (see fig. 2.9).

Since the sensitivity of hydrophones is much greater than that of piezoelectric sensors, hydrophones are particularly suitable for the measurement of bioacoustic signals emitted by cetaceans.

2.3.3 Acoustic Beacons

The active elements of the KM3NeT positioning system are the Acoustic Beacons, produced by Mediterraneo Señales Maritimas (Spain). The beacons currently deployed are autonomous and therefore not synchronized with the detector master clock. They are installed on mechanical tripods with a battery pack that ensures operation for a duration of ∼3 years (see fig. 2.10).

The Acoustic Beacon is a broadband range acoustic emitter ($20\,kHz - 50\,kHz$),

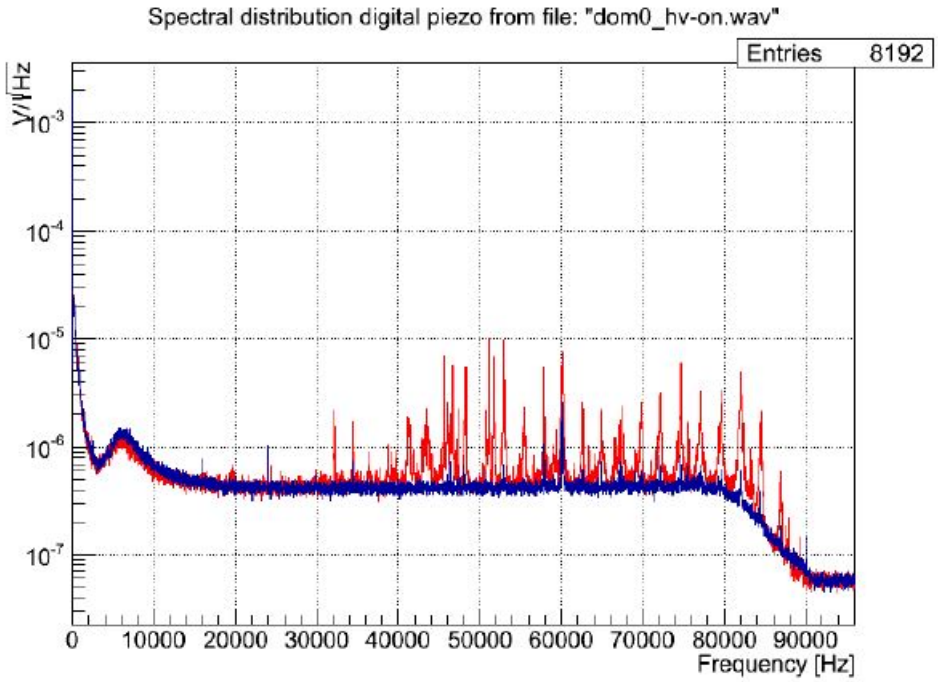

Figure 2.6: Piezo power spectral density as measured within a DOM in the laboratory. The blue curve shows the distribution for PMT power off, the red curve for PMT power on.

capable of operating at depths of up to 440 $bars$ in an underwater environment. It consists of a piezo-ceramic transducer and an integrated electronic board. The transducer is a commercial Free Flooded Ring SX30 manufactured by Sensor Technology Ltd. The electronic board includes a serial interface communication via RS-232 for signal configuration from shore. It can emit short intense signals (Sound Pressure Levels of 180 $dB\,re\,1\,\mu Pa\,@1\,m$ at 34 kHz) with a duration between 0 and 50 ms. The signals can be monochromatic or sine sweep between 1 kHz and 80 kHz. The simulations have shown that the use of sweep signals in a frequency range of 5 kHz between 20 kHz and 50 kHz optimizes the performance of the RAPS [13]. In fig. 2.11 the spectrogram of a sweep signal emitted by one of the ORCA beacons is visible.

Figure 2.7: Picture of a Colmar hydrophone.

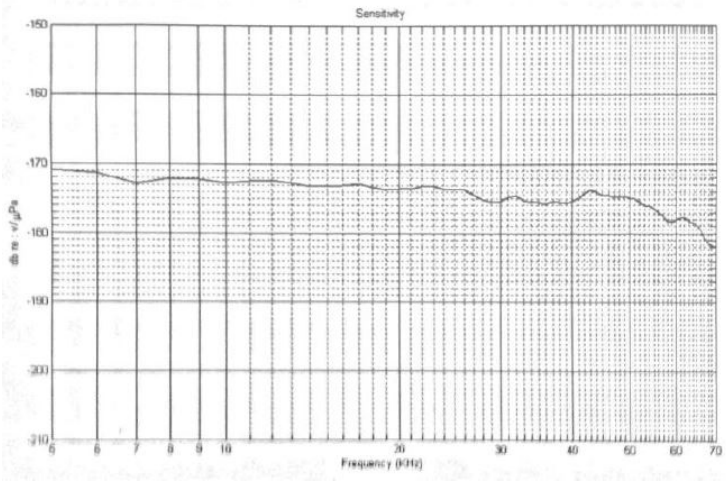

Figure 2.8: Typical sensitivity curve (low gain, $+26\,dB$), at $10\,kHz$, of the Colmar DG0330 hydrophone.

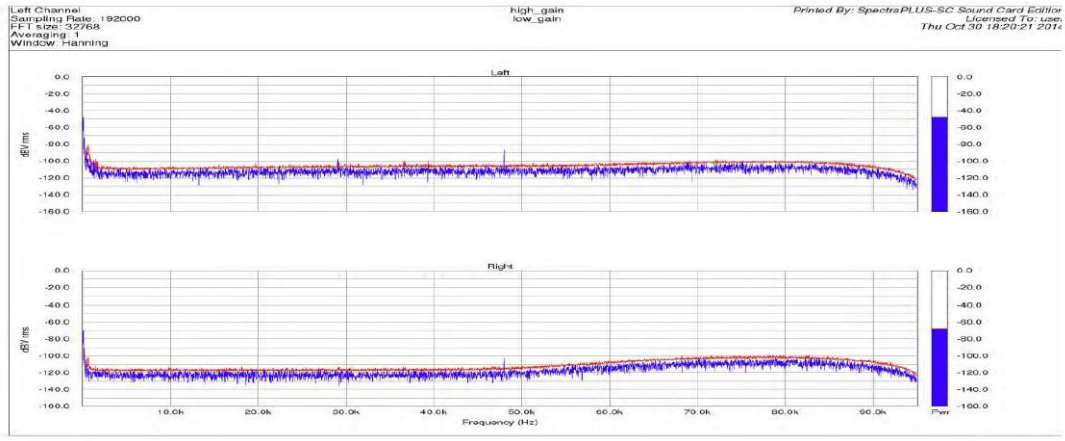

Figure 2.9: Typical noise spectrum (instantaneous: blue, averaged: red) and total noise (blue bar on the right) of a filtered (600 Hz hi-pass filter) DG0330 hydrophone, measured during hydrophone acceptance test at INFN-LNS. Upper plot shows the high-gain channel, lower plot the low-gain channel.

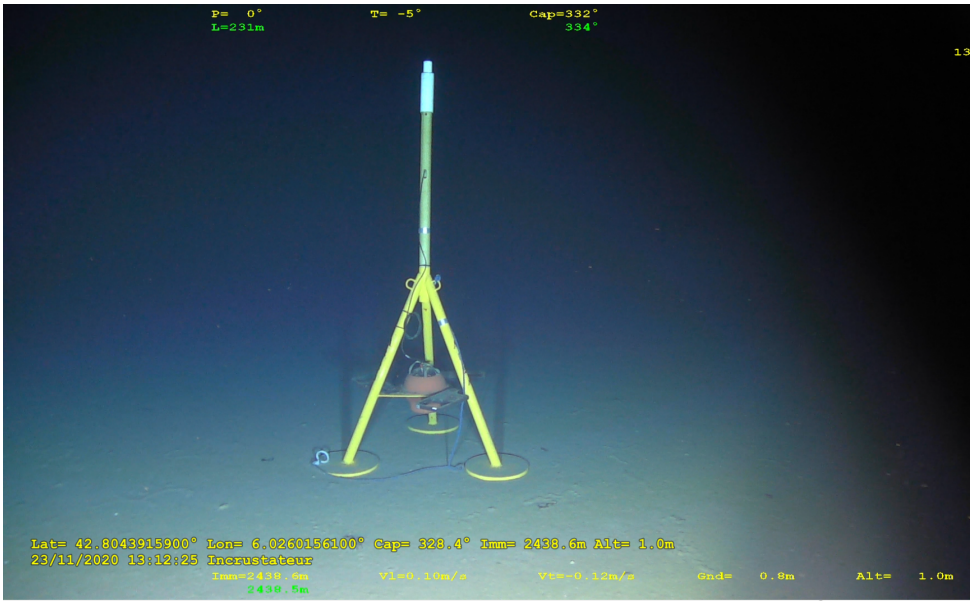

Figure 2.10: Picture of a tripod hosting an Acoustic Beacon.

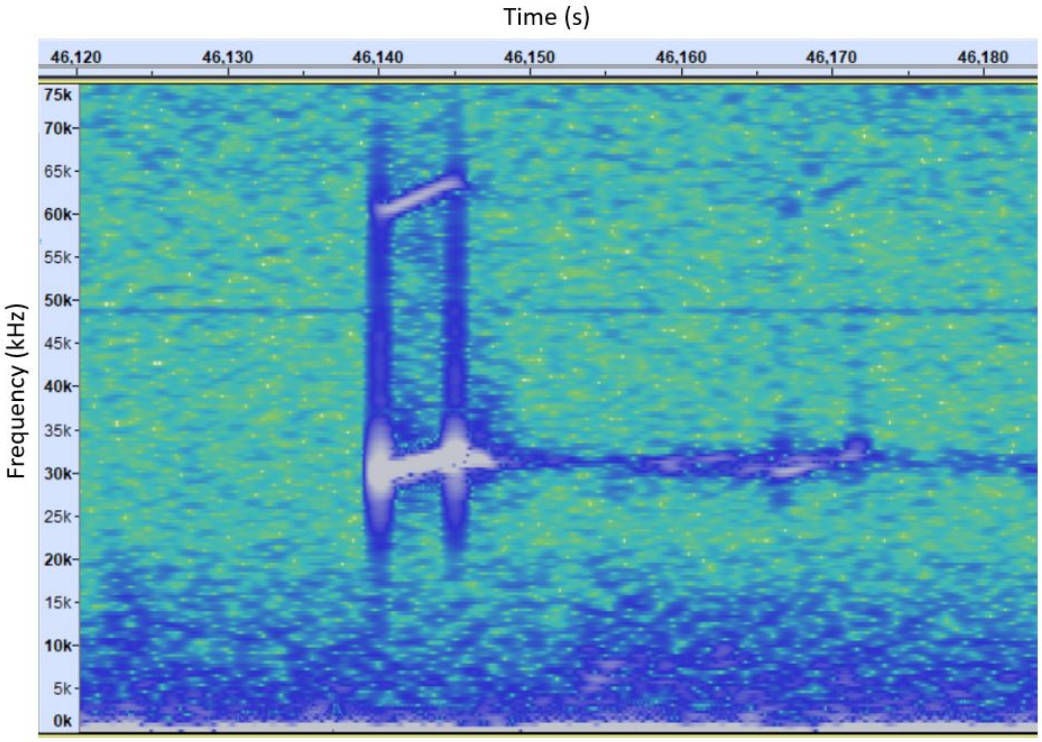

Figure 2.11: Spectrogram (graphic representation of the intensity of a sound as a function of time and frequency) of a sweep signal emitted by one of the ORCA beacons, recorded by DU9 hydrophone - 07/09/2020.

2.4 Physics research with KM3NeT

KM3NeT detectors have several scientific goals in the field of astrophysics and particle physics [6] [14] [15] [16]. The detection of high-energy muon neutrinos exploits the emission of Cherenkov light by the muon and other charged secondary particles produced in an interaction of neutrinos. Muons moving upwards can only arise from the local interactions of neutrinos as the Earth filters out all other particles. Moreover, muons can travel long paths in water and rock in the energy range of interest. Consequently, muons can be generated far from the instrumented volume and still be detected.

Cherenkov radiation is emitted by charged particles passing through an insulating medium with a velocity that exceeds the speed of light in the medium. The coherent radiation is emitted along a cone with a characteristic angle θ_C given by $\cos\theta_C = \frac{1}{\beta n}$ where n is the refractive index of the medium and β is the speed of the particle in units of c.

For relativistic particles ($\beta \sim 1$) in sea water ($n \sim 1.364$) the Cherenkov angle is $\theta_C \sim 43°$.

The number of Cherenkov photons, N_C, emitted per unit of wavelength $d\lambda$ and unit of distance dx from a charged particle e is given by:

$$\frac{d^2N_C}{dxd\lambda} = \frac{2\pi}{137\lambda^2}\left(1 - \frac{1}{n^2\beta^2}\right) \tag{2.1}$$

From eq. 2.1 it can be seen that smaller wavelengths contribute more to the number of photons. In water, the absorption of light strongly suppresses photons with a wavelength below $300\,nm$. Typically the number of Cherenkov photons emitted per metre is about $3.5 \cdot 10^4$.

But how are these superluminal muons generated?

Neutrinos interact with a nucleon N of a nucleus through weak charged current (CC) interactions ($l = e, \mu, \tau$):

$$\nu_l + N \rightarrow l + X \tag{2.2}$$

or neutral current (NC):

$$\nu_l + N \rightarrow \nu_l + X \tag{2.3}$$

The neutrino cross section is proportional to the energy up to about $10^4\,GeV$. At higher energies the linear trend changes and bends downwards (see fig. 2.12).

The muon channel, given its greater sensitivity due to the length of the muon track in water or rock, is the main signature that is considered for the optimization of the detector and the estimation of its sensitivity. At high energies the direction of the muon is closely aligned with that of the neutrino. The average difference

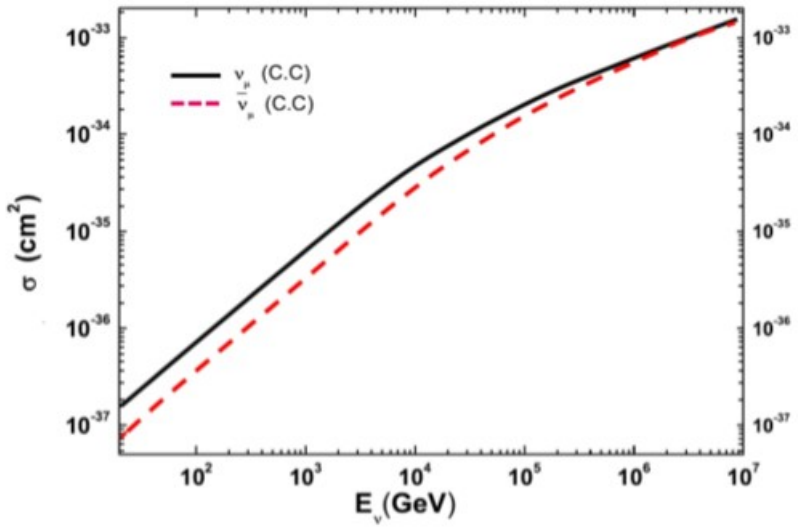

Figure 2.12: cross section of ν_μ and $\bar{\nu}_\mu$ as a function of the neutrino energy.

between the direction of the neutrino and the muon is small, and with energies greater than $100\,TeV$ the direction of the neutrino can be determined with an accuracy better than 0.1 degrees (See fig. 2.13).

A significant advantage of neutrinos over photons for astrophysical observations is related to not being absorbed by the microwave background, interstellar medium or dust. While a $1\,TeV$ photon in water has an interaction length of about $42\,m$, a neutrino of the same energy has $2 \cdot 10^9 m$. The increase in the neutrino cross section with energy is such that at $1\,PeV$ its interaction length becomes a thousand times smaller. At energies of the order of $200\,TeV$ the Earth becomes opaque for neutrinos.

The charged particles produced by the neutrino interactions travel through the medium until they interact or decay for a distance that depends on their energy and the energy lost in the medium. Charged current interactions of muon neutrinos in or near the detector produce long tracks. In fact, for example, a $200\,GeV$ muon travels about $1\,km$.

The showers, on the other hand, are produced by the neutral current interactions and the charged current interactions of electronic and tau neutrinos inside the detector volume. Their length is of the order of metres, so they are seen as a point-like events in such sparse detector.

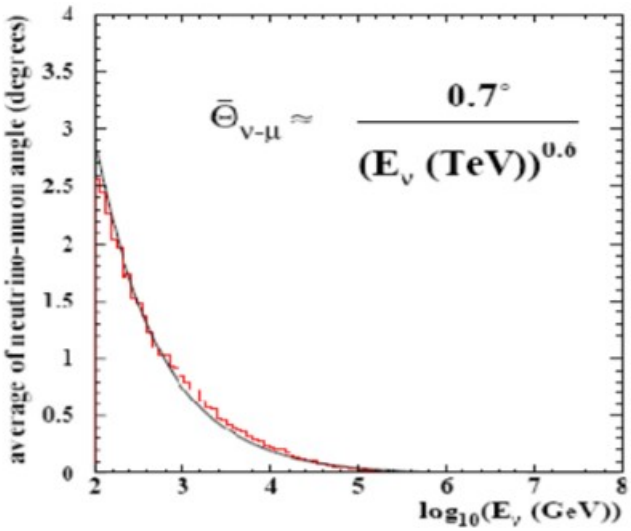

Figure 2.13: Average of neutrino-muon angle (degrees) as a function of energy.

2.4.1 ARCA Physics research

The ARCA experiment aims to detect cosmic neutrinos of very high energy (from about $10\,TeV$ to over $1\,PeV$). The astrophysical production of neutrinos at these energies can occur by the decay of charged pions produced in the proton-proton interactions in dense matter or by photoproduction from the interactions of cosmic rays protons with photons of the surrounding environment.

When two protons interact, they can generate different particles:

$$p + p \rightarrow \pi^{\pm}, \pi^0, K^{\pm}, K^0, p, n, ... \tag{2.4}$$

π^0, π^+, π^- are produced in practically equal quantities. π^0 immediately decays into two γ rays: $\pi^0 \rightarrow 2\gamma$.

Charged pions, on the other hand, decays as

$$\pi^- \rightarrow \mu^- \bar{\nu}_\mu \tag{2.5}$$

and

$$\pi^+ \rightarrow \mu^+ \nu_\mu \tag{2.6}$$

and subsequently

$$\mu^- \rightarrow e^- \bar{\nu}_e \nu_\mu \tag{2.7}$$

and

$$\mu^+ \rightarrow e^+ \nu_e \bar{\nu}_\mu \tag{2.8}$$

Therefore, 3 neutrinos are produced for each pion and 6 neutrinos for each γ ray.

A part of the detectable neutrinos derives from these processes. The alternative source is the photoproduction process.

When a proton interacts with a photon, this mostly likely reaction occurs:

$$p + \gamma_e \rightarrow \Delta^+ \rightarrow \pi^0 + p \tag{2.9}$$

or

$$p + \gamma_e \rightarrow \Delta^+ \rightarrow \pi^+ + n \tag{2.10}$$

The following chain reactions occur, with the production of 3 neutrinos:

$$\pi^0 \rightarrow 2\gamma \tag{2.11}$$

$$\pi^+ \rightarrow \mu^+ \nu_\mu \tag{2.12}$$

$$\mu^+ \rightarrow e^+ \nu_e \bar{\nu}_\mu \tag{2.13}$$

But where do these reactions between particles take place?

The most accepted hypothesis is that very high energy neutrinos are generated in Active Galactic Nuclei (AGN) [17]. An AGN is a compact region located at the centre of a galaxy powered by the energy generated by matter falling into a supermassive black hole with a mass between 1 million and 10 billion times that of the Sun. When matter falls towards the black hole, its angular momentum forms an accretion disk around the black hole. Friction heats matter and changes its state to plasma, and this charged moving material produces a strong magnetic field. The material moving inside this magnetic field produces large amounts of synchrotron radiation and thermal radiation in the form of X-rays. In the vicinity of the supermassive black hole the density is high enough for cosmic rays to interact with the ambient photons and establish photoproduction mechanisms from which, as we have seen, very high energy neutrinos are emitted.

Supernova remnants (SNRs) could be the main source of galactic cosmic rays up to energies of about $10^{15}\, eV$. A fraction of the accelerated particles interact within the supernova remnants and produce γ rays and consequently high energy neutrinos.

Other possible sources of very high energy neutrinos are the Gamma-Ray Bursts [18]. Most likely these very intense electromagnetic emissions are generated by the accretion of matter in a black hole. The black hole/accretion disk

system can be generated by various phenomena, such as the gravitational collapse of a rotating star, the coalescence of two neutron stars or a neutron star and a black hole.

Very high-energy neutrinos could also be generated inside galaxy clusters [19], structures that consist of hundreds to thousands of galaxies that are held together by gravity. Cosmic rays that accumulate in galaxy clusters in cosmological times can interact with the thermal protons of the Intra-Cluster Medium (ICM), a super-heated plasma composed mainly of ionized hydrogen and helium, and thus produce the proton-proton reactions mentioned above.

Finally, even in the Starburst galaxies [19], galaxies in which the star formation process is exceptionally intense, it is possible that hadronic reactions generate very high energy neutrinos.

2.4.2 ORCA Physics research

Depending on the density of the DOMs, KM3NeT can observe Cherenkov photons that arise from neutrinos of different energies. The ORCA experiment has a higher density of optical sensors and therefore aims to detect neutrinos at low energies, few GeV. In particular the measurement of the oscillation pattern of the atmospheric neutrinos of this energy range is sensitive to their mass ordering, one important observable still to be determined.

Neutrinos produced in physical interactions can have 3 distinct flavours (sets of quantum numbers that characterize the elementary particles): electronic ν_e, muon ν_μ and tau ν_τ. Neutrinos that have defined mass (the so-called mass eigenstates, ν_1, ν_2 and ν_3) do not coincide with the three flavour states, ν_e, ν_μ and ν_τ. There is a linear relationship between the mass eigenstates and the flavour eigenstates through the unitary 3×3 matrix:

$$\begin{pmatrix} \nu_e \\ \nu_\mu \\ \nu_\tau \end{pmatrix} = U \cdot \begin{pmatrix} \nu_1 \\ \nu_2 \\ \nu_3 \end{pmatrix} \tag{2.14}$$

with

$$\begin{aligned} U = \begin{pmatrix} 1 & 0 & 0 \\ 0 & \cos\theta_{23} & \sin\theta_{23} \\ 0 & -\sin\theta_{23} & \cos\theta_{23} \end{pmatrix} \times \begin{pmatrix} \cos\theta_{13} & 0 & \sin\theta_{13}e^{i\delta} \\ 0 & 1 & 0 \\ -\sin\theta_{13}e^{i\delta} & 0 & \cos\theta_{13} \end{pmatrix} \\ \times \begin{pmatrix} \cos\theta_{12} & \sin\theta_{13} & 0 \\ -\sin\theta_{13} & \cos\theta_{12} & 0 \\ 0 & 0 & 1 \end{pmatrix} \end{aligned} \tag{2.15}$$

The matrix U is the mixing matrix or Pontecorvo-Maki-Nakagawa-Sakata matrix.

From the oscillation measurements it is known that two neutrinos have a smaller mass difference between them than the mass difference with the third state. Conventionally the closest states are named 1 and 2 with masses $m_1 < m_2$ respectively. It is currently unknown whether m_3 is larger or smaller than $m_{1,2}$. This ambiguity is called "hierarchy": if $m_3 > m_{1,2}$ the hierarchy is called "normal", otherwise "inverted".

In the simplified scenario with only the two flavours, electronic and muonic, therefore with only two mass eigenstates, the probability of conversion at a distance L from the source is:

$$P_{\nu_\mu \to \nu_e} = \sin^2 2\theta \sin^2 \left(\frac{\Delta m^2 L}{4\hbar c e} \right) \tag{2.16}$$

where θ is the mixing angle and $\Delta m^2 = m_2^2 - m_1^2$.

In the three-generation case, obviously, the oscillation formula is more complex and it involves two oscillation scales, one due to the square mass difference $\Delta m^2_{12} = m_2^2 - m_1^2$ and another from the square mass difference larger $\Delta m^2_{13} = m_3^2 - m_1^2$. The sign of Δm^2_{13} determines the mass hierarchy (positive for the normal hierarchy and negative for the inverted hierarchy).

When we replace a neutrino with its antiparticle, we perform a CP transformation. This is due to the fact that neutrinos are chiral objects, i.e., they have their spin substantially oriented in the direction opposite to the motion, while the antineutrinos have their spin substantially oriented in the direction of motion. A violation of CP in the oscillations is equivalent to saying $P_{\nu_a \to \nu_b} \neq P_{\nu_b \to \nu_a}$.

Operationally, the oscillation probability for antineutrinos is obtained by replacing the mixing matrix U with its complex conjugate. With only two generations there would be no CP violation. In the case of three generations this is equivalent to replacing δ with $-\delta$. Only in the case $\delta = 0, \pi$ there would be no violation of CP. Currently there is still no clear indication of the value of δ. This is one of the goals of future neutrino research.

In ordinary matter, the electronic component has a peculiar coupling with electrons. In fact, neutrinos of all flavours can interact through neutral current interaction by exchanging virtual Z^0 bosons with the quarks and electrons in the medium they pass through. Electronic neutrinos also have a second possibility, in which the neutrino and the electrons in the crossed medium exchange through an interaction of charged current (with the emission/absorption of a virtual W boson). Therefore, the electron component of the neutrino acquires an "effective" quadratic mass given by:

$$A = 2\sqrt{2}(\hbar c)^3 G_F N_e E \tag{2.17}$$

where G_F is the Fermi constant, N_e is the electron density of the matter crossed by the neutrinos and E the energy.

This gives rise to a modification of the flavour evolution equation. This is known as the Mikheyev-Smirnov-Wolfenstein (MSW) effect. If the neutrino passes through a portion of constant density matter, it can be seen that the probability of oscillation can be rewritten as:

$$P^M_{\nu_\mu \to \nu_e} = 1 - \sin^2 2\theta^M \sin^2 \left(\frac{4\pi L}{\lambda^M_\nu} \right) \tag{2.18}$$

where θ^M and λ^M_ν are the mixing angle and the wavelength of effective oscillation in the matter:

$$\sin 2\theta^M = \frac{s_{2\theta}}{\sqrt{\left(\frac{A}{\Delta m^2 - c_{2\theta}} \right)^2 + s^2_{2\theta}}} \tag{2.19}$$

$$\lambda^M_\nu = \frac{\lambda_\nu}{\sqrt{\left(\frac{A}{\Delta m^2 - c_{2\theta}} \right)^2 + s^2_{2\theta}}} \tag{2.20}$$

where $c_{2\theta} = \cos 2\theta$ and $s_{2\theta} = \sin 2\theta$.

Due to the changes in the probability of oscillation caused by the crossed matter and due to the different cross section and atmospheric flux for neutrinos and antineutrinos, the rate of events that ORCA expects for neutrinos between 3 and $20\,GeV$ is different for the normal hierarchy and for the inverted one. Furthermore, ORCA aims to improve the measurement of θ_{23} and Δm^2_{32}

2.4.3 Backgrounds and neutrino detection techniques

The backgrounds in a neutrino telescope is caused by random light, not associated with particles passing through the detector or muons, and neutrinos generated in the interactions of cosmic rays in the Earth's atmosphere. Seawater contains small amounts of the natural radioactive isotope of potassium, ^{40}K. This isotope decays mainly with β decay releasing electrons that produce Cherenkov light and therefore a stable and isotropic background of photons with rates of the order of $350\,Hz/cm^2$. Many life forms that inhabit the deep sea also emit light. This bioluminescence has two contributions, a continuous component usually attributed to bioluminescent bacteria and a component described as a series of localized

"pulses" of high-frequency light, likely linked to macroscopic organisms passing through the detector.

Numerous high-energy muons are produced in the interaction between cosmic rays and the atmosphere. Although the detector is at great depth, many muons reach it. The flux of atmospheric muons is, however, many orders of magnitude larger than any flux of muons induced by neutrinos. However we can exploit the fact that atmospheric muons come from above in order to reject this background.

A large number of charged pions and kaons are produced in the interactions of cosmic rays in the atmosphere. Their successive decays produce neutrinos, generating a large flux of high-energy atmospheric neutrinos that are very difficult to discriminate. Up to about $100\,TeV$ muons and neutrinos are mainly produced by the decays of charged pions and kaons, their spectrum is related to the kinematics of the $\pi \to \mu_\nu$ and $K \to \mu_\nu$ decays. In addition, other neutrinos of lower energy are produced by muon decays. The flux of atmospheric neutrinos generated by charged pions and kaons is dominated by muon neutrinos. This flux is usually called the conventional atmospheric neutrino flux and measured in $cm^{-2}s^{-1}sr^{-1}GeV^{-1}$. At energies above $1\,TeV$ and up to about $100\,TeV$ this flux can be expressed with a simple spectrum with power law:

$$\frac{d\Phi_\nu}{dE}(E) \propto E^{-\alpha_\nu} \tag{2.21}$$

where $\alpha_\nu \simeq \alpha + 1$. The quantity $\alpha \simeq 2.7$ corresponds to the spectral index measured for cosmic rays at certain energies.

A large-volume neutrino telescope can identify a signal using two methods:

- For track-like events, through the observation of an excess of events above the expected background in a region of the sky described by a very small solid angle.
- For all neutrino interaction candidates, through the observation of an excess of events above a certain observed energy. The expected cosmic signal has a harder spectrum than that of atmospheric neutrinos. It is expected to be $\frac{d\Phi_\nu}{dE} \propto E^{-\alpha_\nu}$, with $\alpha_\nu \sim 2$ while for the background $\alpha_\nu^A \sim 3.7$.

A muon passing through the detector produces a clean experimental signature, which allows an accurate reconstruction of the muon direction, closely correlated with the neutrino direction. Since neutrinos are not deflected by magnetic fields, it is therefore theoretically possible to individuate the astrophysical source that produced the neutrino. In order to reconstruct with the required accuracy the tracks of muons, and therefore of neutrinos, it is necessary to know with great precision the position and orientation of each photomultiplier. For this reason it is necessary to implement an acoustic positioning system, as described in the next chapter (see chapter 3)

Chapter 3

KM3NeT Acoustic Positioning Systems

3.1 Introduction

One of the goals of KM3NeT, in particular for KM3NeT-ARCA, is the determination of the direction of the reconstructed muons and therefore also the direction of the original neutrino. In order to obtain the required angular resolution (about 0.2°) it is necessary that the PMTs have a temporal resolution of $d \sim 1\,ns$ (See fig. 3.1). Considering that the refractive index in sea water is about $n \sim 1.34$, we can say that in 1 ns the light travels a distance of $d \sim 0.22\,m$. For this reason it is necessary to know the position of each photomultiplier with an accuracy of at least about $20\,cm$.

For this purpose, two positioning systems have been implemented that use sound waves to determine the position of all the elements of the detector:

- NAAPS (Navigation and Absolute Acoustic Positioning System)
- RAPS (Relative Acoustic Positioning System)

NAAPS is the system used during the deployment of the lines and allows to determine the position of the bases of each string with a precision of about $1\,m$ for KM3NeT-ORCA and about $2.5\,m$ m for KM3NeT-ARCA.

The RAPS, on the other hand, is a real time positioning system that allows to refine the position of the bases calculated with the NAAPS and also plans to reconstruct the position of each DOM with an accuracy of $10\,cm$.

Once the position of the base of a line is determined, we do not automatically know the position of each optical module. In fact, the lines may not be perfectly vertical due to the presence of an underwater current that changes their shape. In

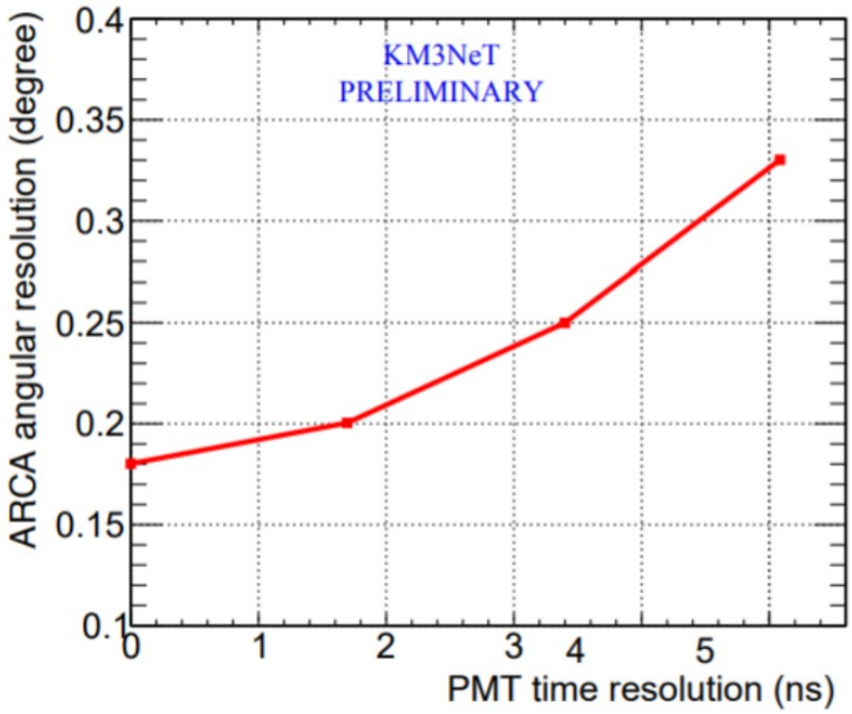

Figure 3.1: ARCA angular resolution of muons (degrees) as a function of temporal resolution of PMTs (ns), considering an energy spectrum of E^{-2} for cosmic neutrinos with $E_\nu > 10\,TeV$ [20].

addition, there is also a stretching effect of the line due to the forces acting on the Dyneema ropes.

The presence of hydrophones (one for each string base) and of piezoelectric acoustic sensors (one on each DOM), primary used by the RAPS to reconstruct the geometry of the detector, extends the field of research to very different studies, such as underwater bioacoustics, studies on underwater background noise and on the effect of anthropogenic activity on the marine ecosystem.

In particular, it is possible to focus on the detection of cetacean clicks (especially sperm whales, Cuvier's beaked whales and various species of dolphins). As we will see in the chapter 4, it is possible to reconstruct the position and movements over time of these animals by calculating the delay times between the different acoustic receivers. As described in detail in the sec. 4.3, it is essential to know the position of the receivers with an accuracy of about $10/20\,cm$ in order to reconstruct the position of marine mammals with good precision.

Therefore, acoustic positioning systems are fundamental for the reconstruction of the muon tracks and therefore of the direction of arrival of the neutrinos, but

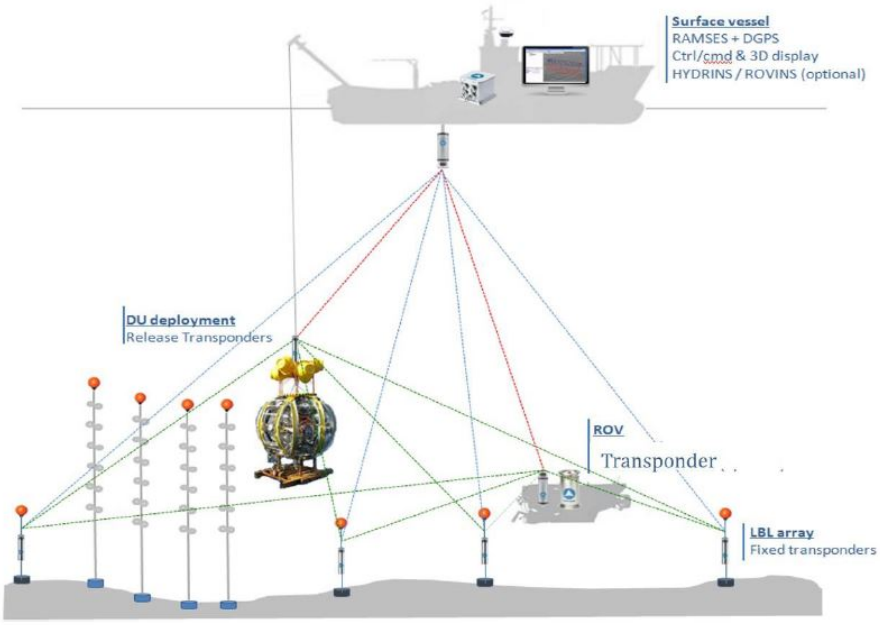

Figure 3.2: Sketch of the NAAPS of ORCA.

they could be also exploited to reconstruct the position and movements of the large marine mammals that pass through the area.

In this chapter the two positioning systems (NAAPS and RAPS) will be described in detail and all the work I have carried out in order to monitor the reception of the signals emitted by the Acoustic Beacons, refine the position reconstruction algorithms and test the algorithms on the real data will be presented.

3.2 Navigation and Absolute Acoustic Positioning System

The NAAPS (Navigation and Absolute Acoustic Positioning System) [13] (see fig. 3.2) is used during the deployment phase of all elements of the system. It is used to measure with an accuracy of about $1\,m$ (in KM3NeT-ORCA) and about $2.5\,m$ (in KM3NeT-ARCA) the position of the ROV (Remotely Operated Vehicle) and all the mechanical structures anchored to the seabed in a geo-referenced coordinate system. An auxiliary commercial acoustic system is used to geo-reference the area (USBL - Ultra Short BaseLine - in ARCA and LBL - Long BaseLine - in ORCA).

A commercial Ultra Short BaseLine (USBL) acoustic system is used for the Italian site of KM3NeT (ARCA), consisting of arrays of sensors, which can act as receivers and emitters, installed on the ROV and on all the structures that

must be deployed in depth. The ship's position is determined using GPS (Global Positioning Satellites). In addition, there is a gyroscope on the ship, which provides heading, pitch and roll information. A transceiver is installed under the ship, which communicates with the acoustic sensors on the ROV and on the detector elements.

For the French site of KM3NeT (ORCA) a Long BaseLine (LBL) acoustic system is used, made by iXBlue company. The system is based on a Low Frequency (LF) range meter system, called RAMSES, installed on the ship on the sea surface. The position of the ship is determined thanks to a Differential Global Positioning System (DGPS) with an accuracy of around $30\,cm$. In addition, four fixed acoustic transponders are placed on the seabed. An acoustic sensor is also placed on the ROV, useful for communicating with the other sensors in the system. Signals with frequencies between 8 and $16\,kHz$ are used, usually not monochromatic, in order to avoid disturbances due to underwater background noise. The RAMSES system is coupled to an Inertial Navigation System (INS), to improve the accuracy of global positioning, by monotoring the movements of the ship and calculating in real time the accurate position of the RAMSES transducer with respect to the DGPS antenna.

The LBL system is used for four different purposes:

- NAAPS-LBL calibration
- DU Deployment
- DU calibration
- ROV positioning

The transponders positioned on the sea bottom around the implementation site of the ORCA detector, which form the Long Base Line, must be calibrated before they can be used. Calibration takes place thanks to the RAMSES internal Kalman filter (efficient recursive filter that evaluates the state of a dynamic system starting from a series of noisy measurements). Numerous range measurements are performed between the sensors under the ship on the surface and the four sensors, using different angles and distances. The INS system serves to compensate for the error committed by combining the information from RAMSES and DGPS (system for geo-locating the ship on the surface). The system outputs the calibrated positions of the four transponders positioned on the sea bed.

The LOM (Launching vehicle of Optical Modules), a structure that contains all the DOMs of the Detection Unit, is attached to the anchor via a hook. The release of the LOM from the anchor is performed by the ROV pulling a string which opens the hook. At the end of the cable that supports the LOM there is an acoustic beacon, used for the deployment of the LOM. The RAMSES system

under the ship sends an acoustic signal to the LOM beacon. This beacon then communicates with the LBL transponders which, in turn, sends a signal to the RAMSES system. The acoustic communication between these systems allows the DU to be deployed in the desired position with an accuracy of about $1\,m$. The position of the DU is then calibrated and fine-tuned using the same system once it has been placed at the sea bottom.

The ROV also has an acoustic sensor, useful for determining its position during the operations it must perform, such as connecting the DU interlink to the node infrastructure.

3.3 Relative Acoustic Positioning System

The RAPS (Relative Acoustic Positioning System) [13] was implemented in order to refine the measurement of the positions of all elements of the detector with respect to the output provided by the NAAPS. As explained in the introduction, in order to correctly reconstruct the tracks of muons and marine mammals, it is necessary to know the position of the sensors with an accuracy of $10\,cm$. The NAAPS provides the position of the base of each DU with an accuracy of $1\,m$ in ORCA and $2.5\,m$ in ARCA. For this reason, an additional positioning system is needed to improve this reconstruction.

Furthermore, the NAAPS only provides us the position on the sea bottom of the deployed elements. The strings, however, are vertical structures of few hundred metres height and can change their shape following the underwater currents (see fig. 3.4). The lines are therefore not perfectly vertical and the highest DOMs can be moved horizontally even up to $3.5\,m$ in ORCA and $14\,m$ in ARCA, in case of high sea currents (see fig. 3.5).

A mechanical model of the line shape was studied for ANTARES [21] and it can be applied in a similar way also for KM3NeT lines [22].

We can express the zenith angle of the line at a certain height as the ratio between the horizontal forces and the vertical forces summed over all line elements j above the point i (see fig. 3.3):

$$\tan(\alpha_i) = \frac{\sum_{j=i}^{N} F_j}{\sum_{j=i}^{N} W_j} \tag{3.1}$$

$$\tan(\alpha) = \frac{dr}{dz} = \frac{F(z)}{W(z)} = g(z) \tag{3.2}$$

$F(z)$ is the horizontal force due to the flow resistance and is parallel to the speed of the underwater current. It depends on the drag of the element j in the

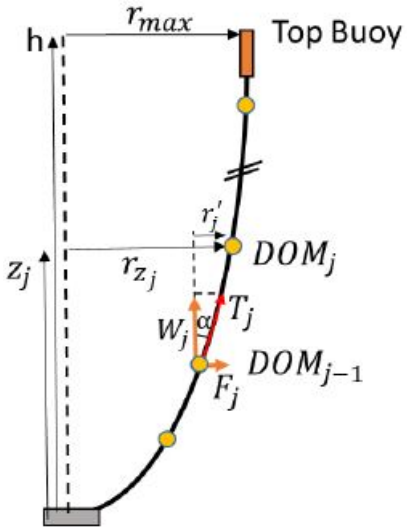

Figure 3.3: Line shape mechanical model.

water and on the square of the current speed. $W(z)$ is the vertical force, instead, which represents the buoyancy of j element.

The resulting force is given by the sum of the contributions of the storey and the cable that supports each DOM, the main cable that runs through the entire DU and the top buoy.

$$F(z) = \left[\left(18 \cdot (f_{storey} + f_{cable}) + f_{cable1}\right)\left(\frac{h-z}{h}\right) + f_{topbuoy}\right] v^2 = f(z) \cdot v^2 \quad (3.3)$$

Similarly for the vertical force $W(z)$:

$$W(z) = (18 \cdot (W_{storey} + W_{cable}) + W_{cable1})\left(\frac{h-z}{h}\right) + W_{topbuoy} \quad (3.4)$$

where "cable1" is the cable between the base and DOM 1 and "cable" is the cable between the other DOMs.

By integrating $g(z)$ between 0 and a height z, we can obtain the displacement $r(z)$ with respect to the vertical:

$$r(z) = \int_0^z g(z')\, dz' = \left[\frac{n}{q}z - \left(\frac{mq - np}{q^2}\right)\ln\left(1 - \frac{q}{p}z\right)\right] v^2 \quad (3.5)$$

where the parameters m, n, p and q are:

$$m = 18(f_{storey} + f_{cable}) + f_{cable1} + f_{topbuoy} \quad (3.6)$$

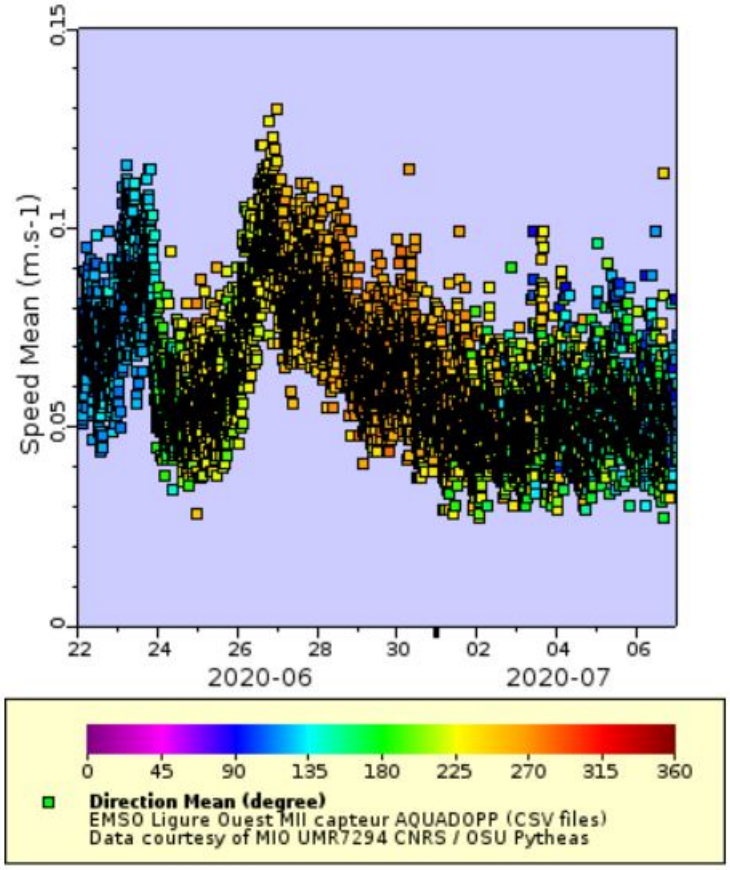

Figure 3.4: Current speed and direction measured closed to the sea bed on the ORCA site - June and July 2020.

$$n = \frac{18}{h}(f_{storey} + f_{cable}) + \frac{1}{h}f_{cable1} \tag{3.7}$$

$$p = 18W_{storey} + W_{cable1} + W_{topbuoy} \tag{3.8}$$

$$q = \frac{18}{h}(W_{storey} + W_{cable}) + \frac{1}{h}W_{cable1} \tag{3.9}$$

The numerical values of the various components of the horizontal and vertical forces have been estimated [23] and can be viewed in tab. 3.1 (ORCA).

This mechanical model is used to correct the shape of the line, after the reconstruction obtained with the Relative Acoustic Positioning System, in case some piezo sensors are not working or systematic time offsets, as we shall see later.

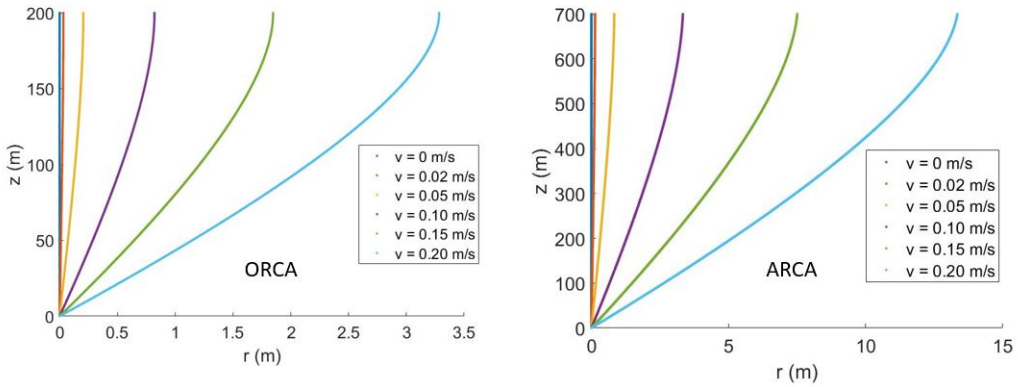

Figure 3.5: Line shape for different sea current speeds in ORCA (left) and ARCA (right).

Element j	**storey**	**cable1**	**cable**	**top buoy**
$f_j[Ns^2/m^2]$	44	284	96	160
$W_j[N]$	126	0	0	1226

Table 3.1: Estimated values of horizontal and vertical forces (ORCA) [23]

In addition to the effect of underwater currents, there is also a stretching effect of the strings, due to the pull of the top buoy on the Dyneema ropes.

For these reasons, it is even more necessary to estimate the position of each optical module using an acoustic positioning system. Since the underwater currents vary over time, the system will have to provide the positions of all elements periodically in real time.

Three autonomous acoustic emitters, not synchronized with the master clock of the detector, called Acoustic Beacons, were placed on the seabed around the system (See Fig. 3.6). The 3 Acoustic Beacons emit different sound patterns in order to be easily recognized (See Tab. 3.2). Every 10 minutes each beacon emits 11 pulses spaced by about 5 s.

On the base of each DU there is a hydrophone, which receives the signal from the beacons. Furthermore, as described in sec. 2.2, on each DOM there is a piezoelectric acoustic sensor capable of detecting the vibrations on the glass sphere caused by the signals emitted by the beacons.

The position of each receiver is calculated by measuring the Times of Arrival of the beacons signals for the different hydrophones or piezo sensors and then applying the multilateration algorithm, described in sec. 3.6.

By combining the RAPS output with the data provided by the compass and

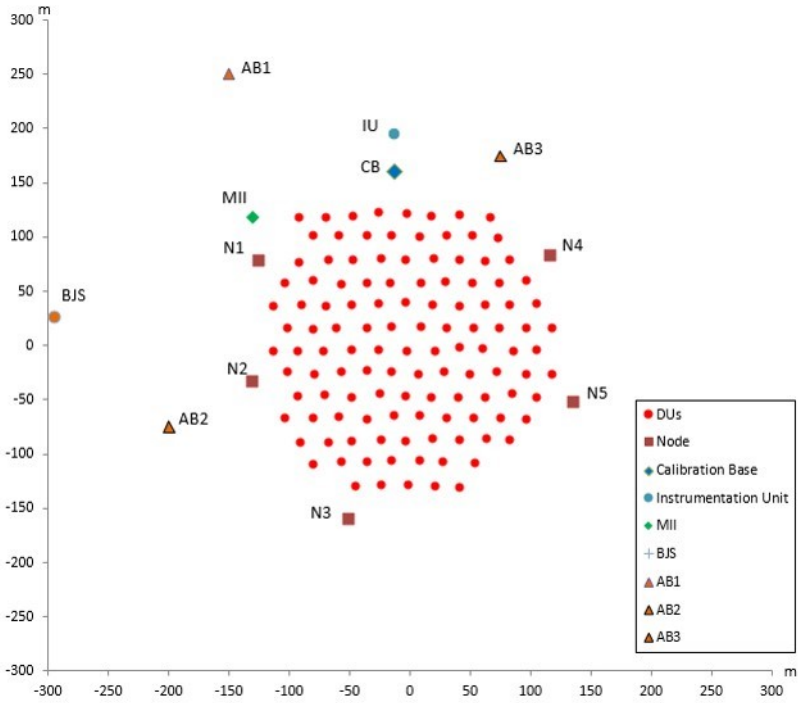

Figure 3.6: Footprint of the ORCA infrastructure (AB stands for Acoustic Beacon)

Beacon number	**emitterid**	**Emitted pattern**
1	12	sweep $26\,kHz - 28\,kHz$ $5\,ms$
2	14	sweep $30\,kHz - 32\,kHz$ $5\,ms$
3	16	sweep $34\,kHz - 36\,kHz$ $5\,ms$

Table 3.2: Pulses emitted by KM3NeT beacons

the inclinometer housed on each DOM, it is possible to obtain the position of each photomultiplier of the DOMs with an accuracy better than $20\,cm$, sufficient to match the timing resolution of the detector of 1ns.

The analogue signal of the receivers is pre-amplified and digitized by an electronic board. In order to convert the data into standard PCM-like format there is a DIT (Digital Interface Transmitter) for the hydrophones and a Field Programmable Gate Array (FPGA) for the piezo sensors. These systems as a whole are called DARs (Digital Acoustic Receivers).

The DARs are perfectly synchronized with the master clock of the detector provided by the CLB (Central Logic Board) of each DOM (clock frequency: $25\,MHz$). Acoustic data, on the other hand, are sampled at $195.3\,kHz$. The signal can be amplified through two distinct channels, one with low gain and one with high gain.

The acoustic data is thus timestamped with the master clock synchronized with the GPS. The CLB continuously sends the data stream to shore via optical fibres. The acoustic data, at this point, are processed by the Acoustic Data Filter (described in sec. 3.4) and then they are used to reconstruct the positions of all the elements of the detector.

It is also possible to save raw acoustic data on the KM3NeT servers, useful for multidisciplinary analyses such as underwater bioacoustics, tracking of various species of cetaceans, the study of underwater background noise and the impact of noise pollution caused by boats on Mediterranean Sea ecosystem. Due to disk space problems, this storing operation is usually performed only for short periods of time (few hours a week).

3.4 Acoustic Data Filter (ADF)

The acoustic signal coming from the receivers (sampling frequency: 195312 Hz), after being digitized, is transferred by the CLB, via UDP (User Datagram Protocol) protocol, to a Data Queue (DQ) and then, via TCP (Transmission Control Protocol) protocol, to the Acoustic Data Filter (ADF).

The purpose of this step is to filter the raw acoustic signal, recognize the patterns emitted by the beacons and reconstruct the Times of Arrival that are saved in the DataBase.

The positioning program takes the ADF acoustic data output from the DataBase to reconstruct the positions of all the receivers.

The data flow of each DOM is analyzed by making the cross correlation between the measured signal and the reference patterns expected from the beacons.

For each time window a Quality Factor is calculated as the maximum of the cross correlation function. If I cross-correlate the signal of one beacon with the known pattern of another I get a Quality Factor higher than the pure noise but lower than the correct signal, as shown in fig. 3.8.

AcousticDataFilter class uses two IO services: one to handle connections and the other to perform the analysis.

The data in an ADF output are saved in the Database in the format shown in fig. 3.7.

3.5 Acoustic Monitoring Program description

Starting from the output of the ADF, described in the previous paragraph, I implemented a program to monitor the quality of the data from the acoustic beacons as recorded by the hydrophones and piezo sensors of each line.

RUN	UnixTimeBase	DOMid	Emitterid	ToAs	Quality Factor
7155	1579037490.63109120	808967761	12	0.666493	11391
7155	1579037490.63109120	808967761	14	0.667487	8647
7155	1579037490.63109120	808967761	16	0.666099	10720
7155	1579037490.63109120	808972698	12	0.457852	1025
7155	1579037490.63109120	808972698	14	0.073013	971
7155	1579037490.63109120	808972698	16	0.116338	1138
7155	1579037490.63109120	808981528	12	0.536871	722
7155	1579037490.63109120	808981528	14	0.651247	732
7155	1579037490.63109120	808981528	16	0.487745	786
7155	1579037491.26218240	808967761	12	0.668685	11154
7155	1579037491.26218240	808967761	14	0.667773	9734
7155	1579037491.26218240	808967761	16	0.668634	8925
7155	1579037491.26218240	808981528	12	0.616651	682
7155	1579037491.26218240	808981528	14	0.020156	732
7155	1579037491.26218240	808981528	16	0.391172	797
7155	1579037491.89327360	808967761	12	0.670451	11017
7155	1579037491.89327360	808967761	14	0.110579	9460
7155	1579037491.89327360	808967761	16	0.011410	7955
7155	1579037491.89327360	808981528	12	0.217501	711
7155	1579037491.89327360	808981528	14	0.454465	709
7155	1579037491.89327360	808981528	16	0.359955	959
7155	1579037492.52436480	808967761	12	0.666135	11407
7155	1579037492.52436480	808967761	14	0.666099	10303
7155	1579037492.52436480	808967761	16	0.666125	9103
7155	1579037492.52436480	808981528	12	0.391305	729
7155	1579037492.52436480	808981528	14	0.541991	727
7155	1579037492.52436480	808981528	16	0.285710	775
7155	1579037493.155456	808967761	12	0.469803	9465

Figure 3.7: Data Format of Acoustic data stream saved in the DB.

This section of my thesis represents part of the service work I was asked to develop from the KM3NeT collaboration.

The acoustic data are saved in the database in the format shown in fig. 3.7

- RUN indicates the run number
- UnixTimeBase indicates the time elapsed since 1 January 1970 in seconds
- DOMid identifies the DOM. Emitterid identifies the signal emitted by the beacon
- ToAs are the Times of Arrival of the acoustic signal to the receivers on the DOMs or on the bases (piezo or hydrophones)
- The Quality Factor is the maximum of the cross-correlation function between the expected signal and the measured one

In order to monitor the acoustic reception of the beacons signals it is necessary to filter the acoustic data to isolate the signal from the noise, using the information of the number of expected pulses and the value of the Quality Factor. An ad-hoc Quality Factor threshold will be defined for each emitter/receiver couple.

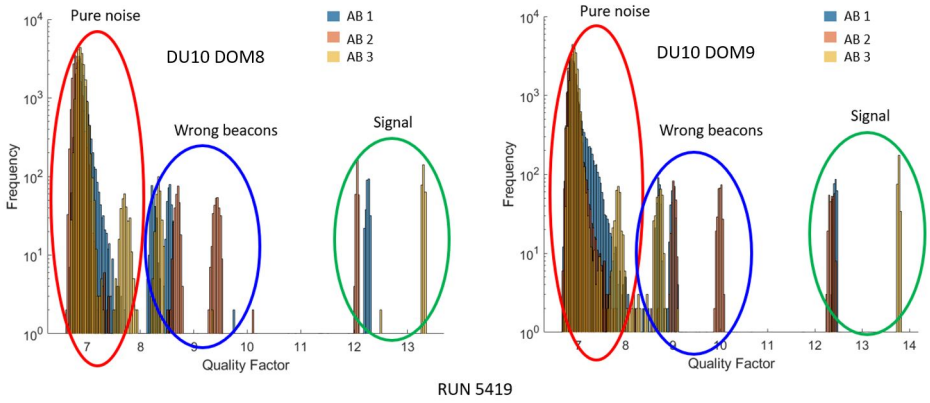

Figure 3.8: Distributions of the Quality Factors (DU10-DOM8 and DU10-DOM9 - RUN 5419).

In fig. 3.8 the distribution of Quality Factors in two different cases (ORCA DU10-DOM8 and DU10-DOM9) is shown. In this case the signal is clearly distinguishable from the noise and it is possible to establish a threshold on Quality Factors. Three different populations of data are clearly visible. On the left of the plot, data can be attributed to pure noise, intermediate Quality Factor are due to the recognition by the Acoustic Data Filter of the beacon signals that are not emitting at that moment, while the distribution with the largest Quality Factors represents the signal from the correct beacon.

As can be seen in fig. 3.9, the Quality Factor is independent of the DOM location. Each beacon emits trains of 11 pulses, one every 5 seconds, with a repetition rate of 10 minutes.

An automatic system is required that identifies the thresholds for each emitter/receiver couple and that filters the data from the noise.

The time windows in which only noise is present and those in which the signal is present have been identified considering the highest Quality Factor and the known time interval between each series of emissions.

The data inside the windows must be filtered in order to isolate the signal from the noise. First of all it is necessary, within each window, to order the data from the lowest to the highest Quality Factor. Subsequently a series of cascaded filters was applied to each of the windows:

1. In order not to skip some pulse, starting from the data with the highest Quality Factor, take a number of signals equal to twice the number of pings emitted by the beacon every 10 minutes. (for safety: sometimes it happens that the same signal is saved twice in the database) (first filter);

2. Delete the signals with the same ToA (second filter);

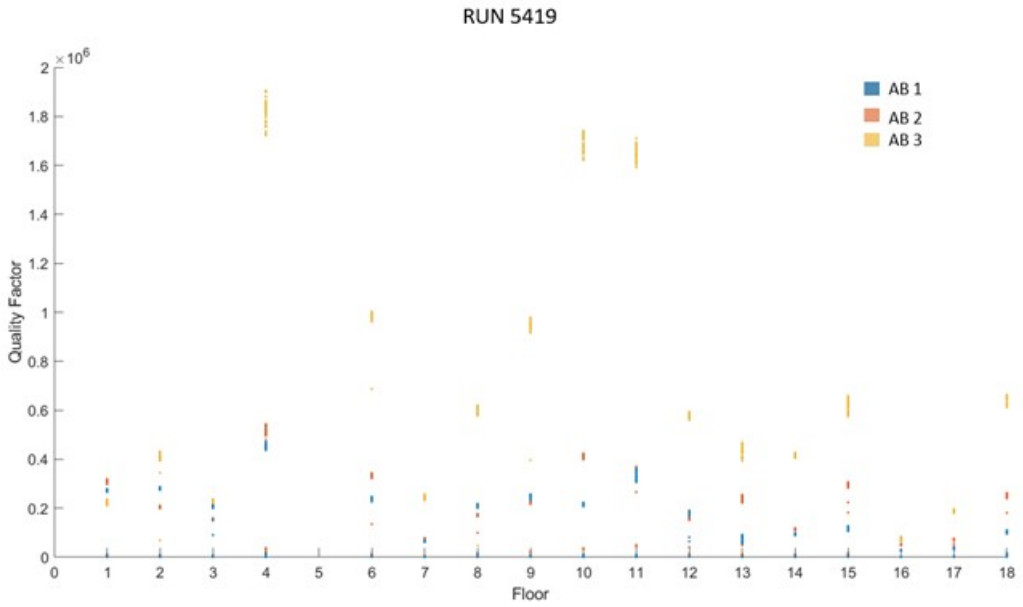

Figure 3.9: Quality factors as a function of the floors - ORCA DU10 - RUN 5419.

3. If more than 11 signals remained, delete the ones with the lowest QF (third filter);

4. Delete signals that have QF less than the maximum QF of the noise (fourth filter);

5. Delete the signals that are not coherent with the $\sim 5\,second$ time interval between each pulse (fifth filter).

Observing the results of the monitoring system over time, it has been shown that with this chain of filters the number of signals lost or incorrectly recognized as signals are less than 1 %.

At this point it is possible to set the threshold for each emitter/receiver couple, taking the minimum QF of the selected signals and subtracting three times the standard deviation of the QFs. An application of this method is visible in fig. 3.10.

Two versions of this program have been implemented, one offline and the other online, included among the official KM3NeT online monitoring tools. Every 10 minutes the plot is updated and this allows to monitor in real time the detection of the beacon signals from all receivers of the system.

Since November 2020, a modification in the Acoustic Data Filter has been implemented. The threshold is set before the data are stamped in the database stream. This allows lower disk usage in the database and required a small change in the monitoring program, which has been updated.

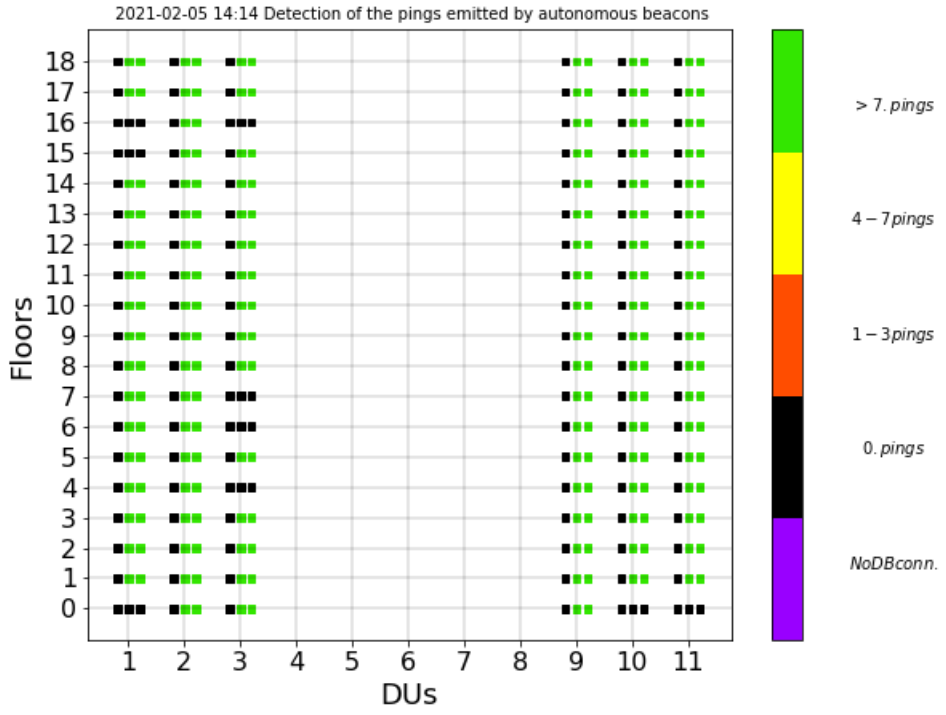

Figure 3.10: ORCA Acoustic Monitoring plot published in the Orca Monitoring page - The three columns for each line represent the three Acoustic Beacons. Acoustic Beacon 1 column is black because this emitter was not active during this run 9414. Green spots mean that the most part of the pulses has been detected.

3.6 Acoustic Positioning System algorithms

The KM3NeT acoustic system, as described in sec. 3.3, is made up of piezoelectric receivers (one for each DOM) placed in the inner surface of the glass sphere surrounding the Optical Modules and more sensitive hydrophones positioned at the base of each string. Each Detection Unit, therefore, has 19 acoustic receivers. Three acoustic emitters (Acoustic Beacons) are positioned around the detector, as seen in fig. 3.6. Each emitter generates every 10 minutes a series of 11 pulses (see tab. 3.2) with an interval of around 5 seconds.

The beacons are autonomous, not synchronized with the master clock of the detector. For this reason, we do not know the Times of Emission of these signals. The acquisition system stores in the Database the absolute Times of Arrival of the signals to each receiver. The different pulses emitted by the beacons are recognized on the basis of a Quality Factor, defined as the maximum of the cross correlation

between the expected signal and the measured one.

The position of each line, as illustrated in sec. 3.2, is measured during deployment operations with an accuracy of around $1\,m$ in ORCA and around $2.5\,m$ in ARCA. The hydrophones on the base of each string keep their position over time, being anchored to the seabed. The piezoelectric sensors on DOMs, on the other hand, can deviate from the vertical position with respect to the axis of the base. The reason for this behaviour is the possible presence of underwater currents, which can act in different directions and have speeds up to about $20\,cm/s$. In fig. 3.5 it is possible to observe the effect that these currents can cause to the lines. Furthermore, the lines undergo a stretching phenomenon due to the buoyancy of the line.

In order to improve the accuracy of the measurements made during deployment and therefore reconstruct the positions of all elements of the system with sufficient precision, it is necessary to implement an effective algorithm that uses all the information. There are two different approaches to the problem:

1. General method (developed by me): the unknowns of the system are the coordinates of the receivers, the Times of Emission of the beacons and the coordinates of the beacons; the nominal positions, measured during deployment, are the initial conditions for the minimization problem; the measured Times of Arrival are the physical information of the problem [24].

2. Approximate method: the unknowns of the system are only the coordinates of the receivers. The nominal beacon coordinates measured during deployment are considered exact and the Times of Emission are approximated exploiting the fixed position of the hydrophones at the base of each string.

In an initial phase these two different approaches were tested through simulations, which showed very similar results. The second algorithm, computationally simpler and faster, was applied to real data and provided the first reasonable results.

Subsequently, a Dutch group in Nikhef, implemented a third algorithm, conceptually similar to the first approach, but which adds a preliminary tuning phase of the initial parameters based on the measurement history.

This section will describe my work done to test the efficiency of the different approaches to the problem of reconstructing the position of the receivers and the results of the first applications to real data will be discussed.

3.6.1 General method

The most general method to reconstruct the positions of the KM3NeT receivers considers as unknowns of the system, parameters of the minimization problem,

the x, y and z coordinates of the receivers (x_h, y_h, z_h), the x, y and z coordinates of the beacons (x_b, y_b, z_b) and the Times of Emission of the three emitters. The nominal positions are used as initial values of the minimization process. The algorithm was implemented in Python using the MINUIT package (https://iminuit.readthedocs.io/en/stable/).

In a first phase a two-dimensional problem was studied, in which only the three emitters and a variable number of hydrophones at the same depth were considered. For each pair Beacon/Hydrophone the measured Time of Arrival (ToA) is equal to the Time of Flight (ToF) plus the Time of Emission (ToE):

$$ToA_{bh} = ToF_{bh} + ToE_b = \frac{\sqrt{(x_h - x_b)^2 + (y_h - y_b)^2}}{c_{sound}} + ToE_b \tag{3.10}$$

where c_{sound} is the speed of sound in sea water. x_h, y_h, x_b, y_b and ToE_b are unknown parameters, but the nominal values, determined during the deployment with an accuracy of around $1\,m$ in KM3NeT-ORCA and $2.5\,m$ in KM3NeT-ARCA, are known. b and h respectively stand for beacons and hydrophones.

If we sum the squares of eq. 3.10 for each pair Beacon/Hydrophone and divide the function by the square of the error on measured Times of Arrival and by the number of terms, we obtain the following function to minimize:

$$\frac{\sum_{b=0}^{N_b}\sum_{h=0}^{N_h}\left[ToA_{bh} - ToE_b - \frac{\sqrt{(x_h-x_b)^2+(y_h-y_b)^2}}{c_{sound}}\right]^2}{\Delta^2 \cdot N_b N_h} \tag{3.11}$$

where Nb represents the number of beacons and Nh the number of receivers.

The uncertainty on the measured Times of Arrival (Δ) is estimated to be $50\,\mu s$.

Several simulations were performed in order to determine the behaviour and the results of the minimization process. The configuration of the ORCA detector used in the simulations is shown in fig. 3.11. It corresponds to the layout of the detector elements deployed in June 2019. The following are the main steps of the simulation algorithm:

1. Randomly extract a true initial beacon/hydrophone configuration compatible with the nominal positions and uncertainties.

2. Arbitrary choose the Times of Emission of the beacons.

3. According to this configuration, calculate the Times of Arrival

4. Randomly extract the starting parameter values x_h, x_b, y_h, y_b within an uncertainty of $\pm 1\,m$ with respect to their nominal values.

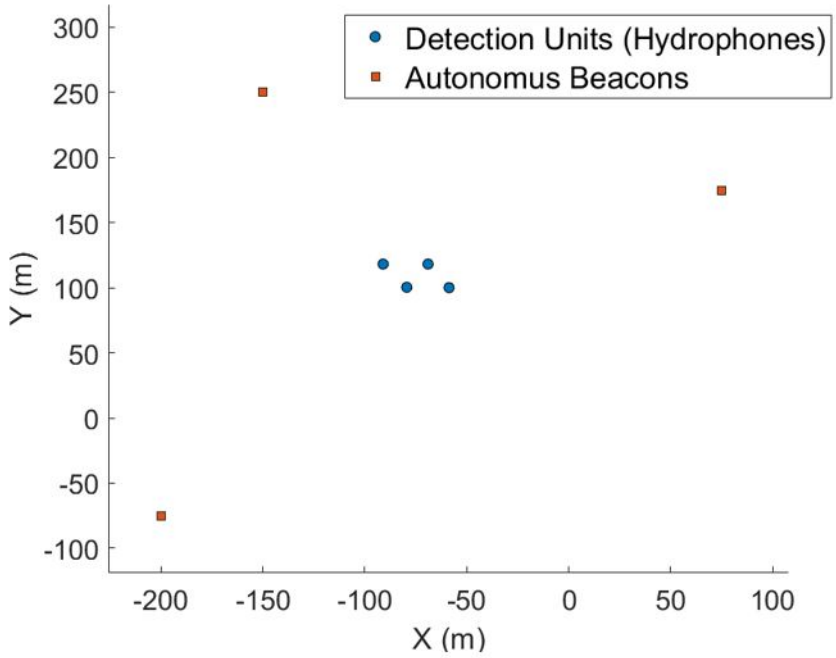

Figure 3.11: ORCA layout after deployment of June 2019. Blue circles represent the hydrophones. Red squares represent the beacons.

5. Run the Python package IMINUIT [25] N times with different starting values of the parameters ($N = 3000$ appears to be sufficient) to obtain N sets of solutions, different for different starting conditions.

6. Use as upper limit for the relative position error the quantity: $Err = MAX(diff) - MEAN(diff)$ in which diff is an array containing the differences between average reconstructed position and the true one, separately for receivers and emitters.

7. In order to compensate for a possible dependence of this uncertainty from particular true values, repeat M times the procedure and average the M error estimations.

Many solutions found by the minimizer represent a rigid shift or a rotation with respect to the true positions. Actually, the minimizer finds also solutions that do not represent rigid shifts, rotation or even combinations between the two. This is due to the geometry of the system. As can be seen in fig. 3.12, we can notice that the reconstructed positions of hydrophones are very similar to a rigid shift compared to true positions. This does not happen for beacons, whose reconstructed positions are more indeterminate. The effect is linked to the layout

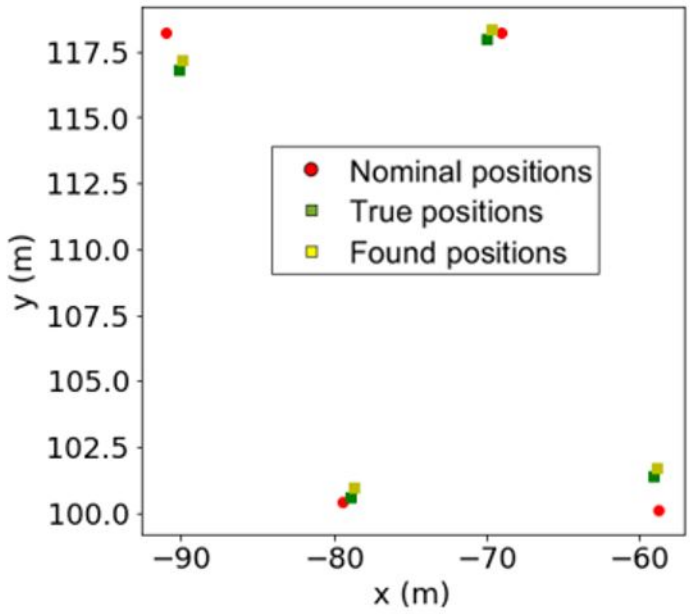

Figure 3.12: Nominal positions (red circles), true positions (green squares) and average found positions (yellow squares) of the DU bases of the 4 lines considered in the simulation.

Coordinate	**Hydrophones**	**Beacons**
x	$Err = 6\,cm$	$Err = 58\,cm$
y	$Err = 4\,cm$	$Err = 46\,cm$

Table 3.3: Estimated average uncertainty on receiver and emitter x and y coordinates (ORCA)

configuration. In fact, reversing the positions of hydrophones and beacons, the positions of the beacons are now determined with much larger accuracy than those of the hydrophones. This effect is clearly visible in fig. 3.13.

Following steps 6) and 7) of the simulation the accuracy on the position of the hydrophones and beacons can be determined (see tab. 3.3).

The method can be also applied to the three-dimensional case, where the ToA of the acoustic signals measured by the piezo sensors mounted in each DOM can be used to determine the shape of the lines, which depends on the direction and intensity of the sea current.

In order to simulate the true position of each element of the line, the code fixes a direction and a speed of the sea current and then uses the parameters and equations of line fit shape studies [22] [23].

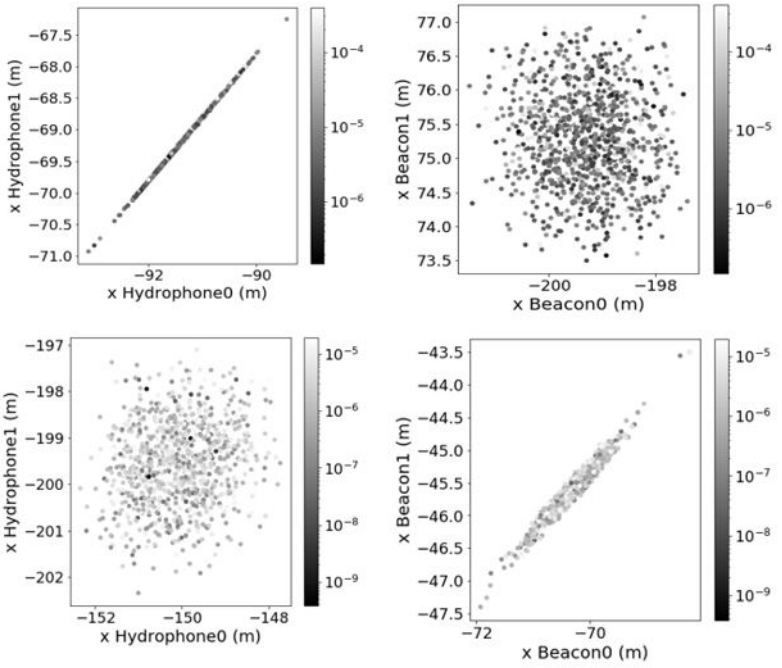

Figure 3.13: At the top, the reconstructed positions of a hydrophone (or beacon on the top right) versus the reconstructed position of another hydrophone (or another beacon on the top right) in the "normal" configuration in which the hydrophones are in the centre and the beacon around. At the bottom, instead, the same plots in the opposite case, with the beacons in the centre and the hydrophones around. The sharp correlation observed in the top left plot indicates that all the found positions of the hydrophones differ one fom the other by a rigid translation.

Initially, a subset made up of 3 beacons, 2 hydrophones and 4 DOMs (two for each detection unit) is considered. The true position of the elements of the layout (beacons and hydrophones) is extracted within the deployment error ($1\,m$). The true coordinates of the DOMs are calculated assuming a certain speed and direction for the sea current. The minimization process gives as output the three Times of Emission, the coordinates of the beacons, the coordinates of two hydrophones and the coordinates of four piezos. At this point the lowest receiver is removed, a third DOM is added and now the positions of the beacons, of the first two DOMs and the values of the ToEs are fixed to the values found at the previous step. The minimizer is run again with the following subset and the process is iterated till the top DOM.

As you can see in fig. 3.14, also in this case the reconstructed positions of each DOM seem shifted with respect to the true positions of the elements of the system.

The estimated accuracy of this three dimensional algorithm is shown in tab. 3.4.

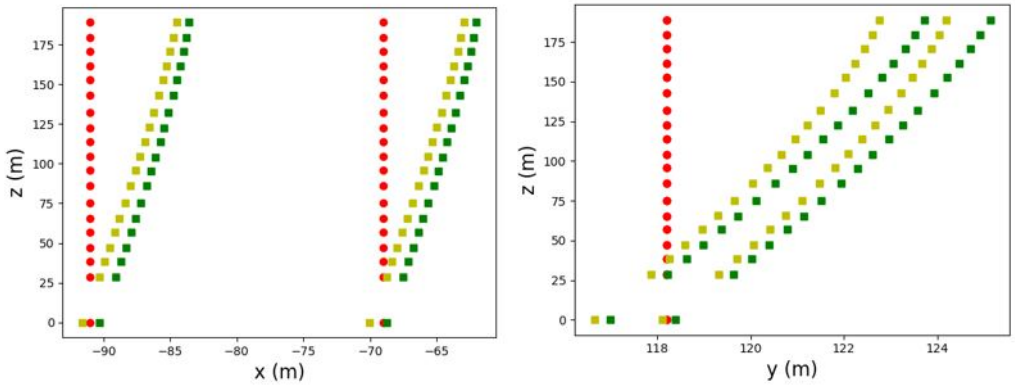

Figure 3.14: Nominal x (left) and y (right) (red circles), true x (left) and y (right) (green squares) and average reconstructed x (left) and y (right) (yellow squares) of the bases and the DOMs of the two lines considered in the 3D simulation. A current with a speed of $0.25\,m/s$ and a heading of 45 degrees was used.

Coordinate	**Receivers**	**Beacons**
x	$Err = 20\,cm$	$Err = 35\,cm$
y	$Err = 20\,cm$	$Err = 31\,cm$
z	$Err = 8\,cm$	$Err = 1\,cm$

Table 3.4: Estimated uncertainty on receivers (averaged on all piezo sensors and hydrophones) and emitters positions (ORCA) (A current with a speed of $0.25\,m/s$ and a heading of 45 degrees was set)

This general method gives comforting results reaching the required accuracy in the determination of the positions of the Digital Optical Modules. The algorithm is, however, computationally heavy and slow.

In the next paragraph a second possible approach to the problem will be described, which approximates the Times of Emission of the beacons assuming the knowledge of the exact position of the hydrophones.

3.6.2 Approximate method

An alternative method, usefull to cross chek my results, is the one developed at LNS (Laboratori Nazionali del Sud) - Catania, that approximates the calculation of the Times of Emission of the beacons assuming the knowledge of the exact position of the hydrophones. Improvements and adjustments were implemented by me and subsequently tests were performed using simulations and the algorithm was applied to real data. In this paragraph the details of the program will be

described.

The input parameters of the algorithm are:

- Sound speed at the sea bottom ($1546.365\,m/s$)
- Duty cycle beacons ($600\,s$)
- Time offset piezos ($170 \cdot 10^{-6}\,s$)
- Time offset hydrophones ($50 \cdot 10^{-6}\,s$)
- Nominal positions of the hydrophones
- Nominal positions of the beacons

First of all the script checks for each run which hydrophones are working properly. Then the number of pulses emitted by each beacon is measured and for each piezo/emitter couple the threshold on the Quality Factors is roughly estimated. At this point the program gets the Times of Arrival and calculates the Times of Emission of the beacons. The beacons are autonomous and, therefore, in principle the Times of Emission are unknown. This algorithm calculates the Times of Emission just using the Times of Arrival of the Hydrophones and the nominal positions of hydrophones and beacons. In order to mitigate the uncertainty the final Times of Emission are an average between the Times of Emission calculated using the different fixed hydrophones. Subsequently, a multilateration algorithm is applied independently for each receiver. This is one of the main differences with respect to the general method. The position of each receiver is reconstructed using the multilateration algorithm, based on the following known equation:

$$ToA = ToE + ToF \tag{3.12}$$

3.6.3 Comparison between the two algorithms

General and approximate methods have been compared:

- by calculating the relative position between the DOMs of a single string (ORCA DU1 used as test line),
- in calculating the relative position between the bases of two different strings (ORCA DU1 and DU2 used as test lines).

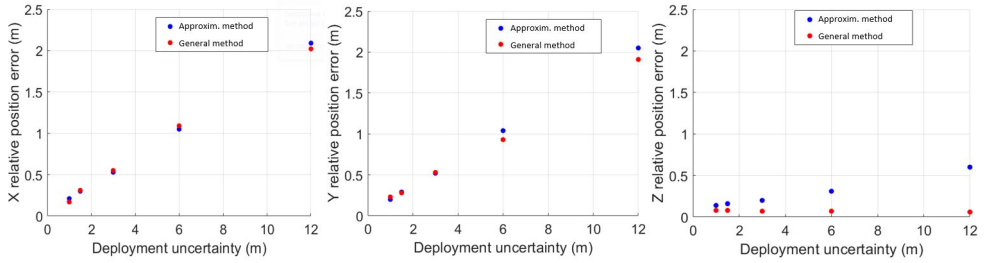

Figure 3.15: Relative position error of x, y and z DOMs coordinates as a function of the deployment uncertainty - comparison between general and approximate method.

The difference between the found positions and the true ones, separately for x, y and z, was calculated for 1000 different simulated true positions, uniformly extracted within different depolyment uncertainties. The results of the two methods were compared (see fig. 3.15).

The relative position error for x and y coordinates of the DOMs as a function of the deployment uncertainty is comparable for the two methods. With a deployment uncertainty of $1\,m$ (KM3NeT-ORCA theoretical uncertainty) there is an error on the relative position of around $10\,cm$. For the z coordinate a greater difference between the two methods can be noticed, probably due to the lack of constraints on this variable in the approximate method.

Subsequently, the uncertainty on the relative position between different strings using the two methods was compared. The difference between the true coordinates (separately x and y) of two different strings was calculated as:

$$\Delta_{true} = coord^{true}_{DU1} - coord^{true}_{DU2} \tag{3.13}$$

while the difference between the found coordinates (separately x and y) of two different strings was calculated as:

$$\Delta_{found} = coord^{found}_{DU1} - coord^{found}_{DU2} \tag{3.14}$$

To estimate the relative position error for different string the quantity $Diff = |Diff_{true} - Diff_{found}|$ was calculated for 5000 different simulated true positions, uniformly extracted within the deployment uncertainty.

In the histograms in fig. 3.16 we can see that the error on the relative position between two different strings is about $20/30\,cm$ using both the first and the second method.

In fig. 3.17, instead, we can see the value of the FWHM as a function of the deployment uncertainty. Considering that ORCA deployment uncertainties are less than $1.5\,m$ the two methods are comparable. For greater initial uncertainties the

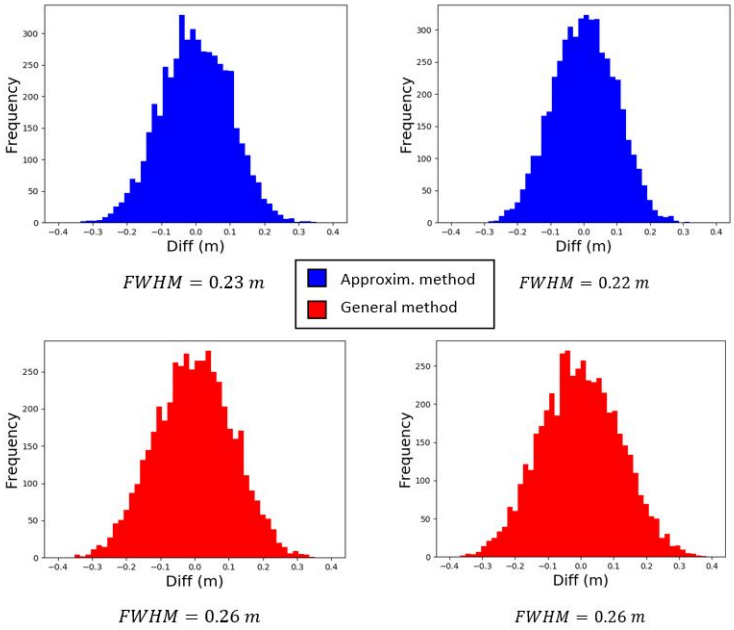

Figure 3.16: Difference between x (left) and y (right) true and found coordinates - Distributions of 5000 different true positions - Comparison between general and approximate method.

general method may work better compared to approximate method. The general method results were essential to confirm that the assumptions of the approximate method did not affect the quality of the reconstruction.

3.6.4 Application of the approximate algorithm to the real data

Due to the compared performances of the two approaches for the currrent deployment uncertainties (few meters) and to the easier implementation, the approximate method was applied to real data confirming the reliability of the algorithm.

In fig. 3.18 we can see the position of the receivers during a period of calm sea. Consistent with what is expected, the lines appear vertical. In fig. 3.19, instead, we can observe the positions of the receivers during a period in which a consistent underwater current was present (around 11 cm/s [26]). In this case the lines appear consistently inclined in the direction of the water flow. In fig. 3.20 it is possible to observe the results of the fit of the line using the mechanical parameters, as described in sec. 3.3 [22] [23]. The current speeds estimated on the basis of the inclination of the different lines is consistent with the measured one within around 2 cm/s [26].

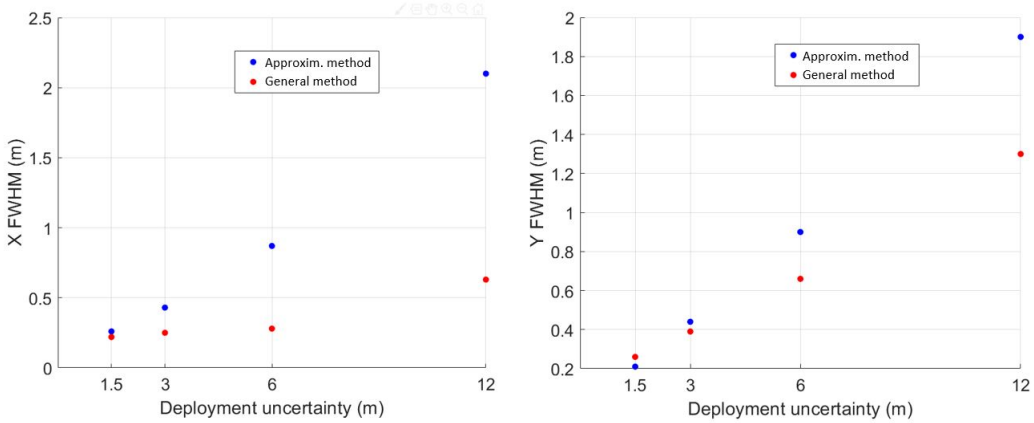

Figure 3.17: x and y reative position error between two lines as a function of the deployment uncertainty - comparison between general and approximate method.

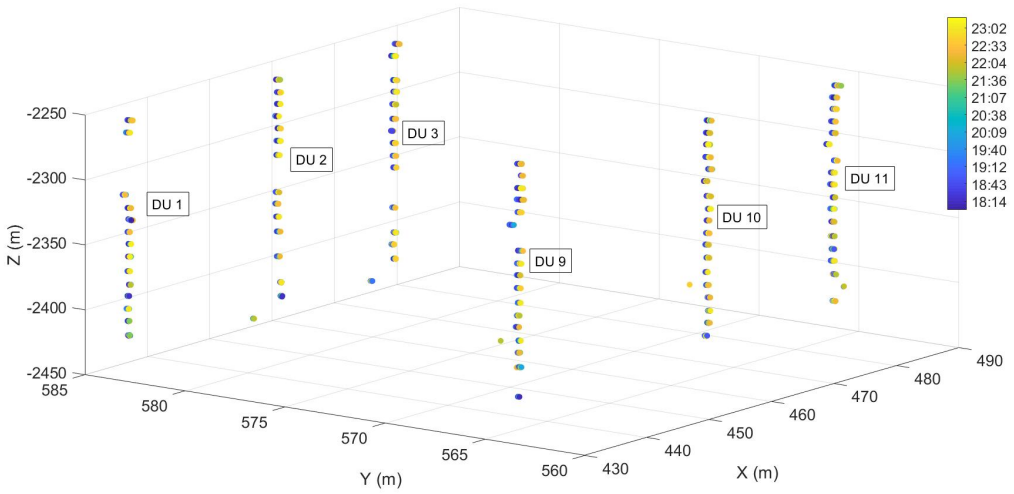

Figure 3.18: Reconstructed positions of 6 ORCA lines during calm sea period (19/03/2020) - The colours represent the time (from dark blue to yellow - 6 hours in total - duration of a run).

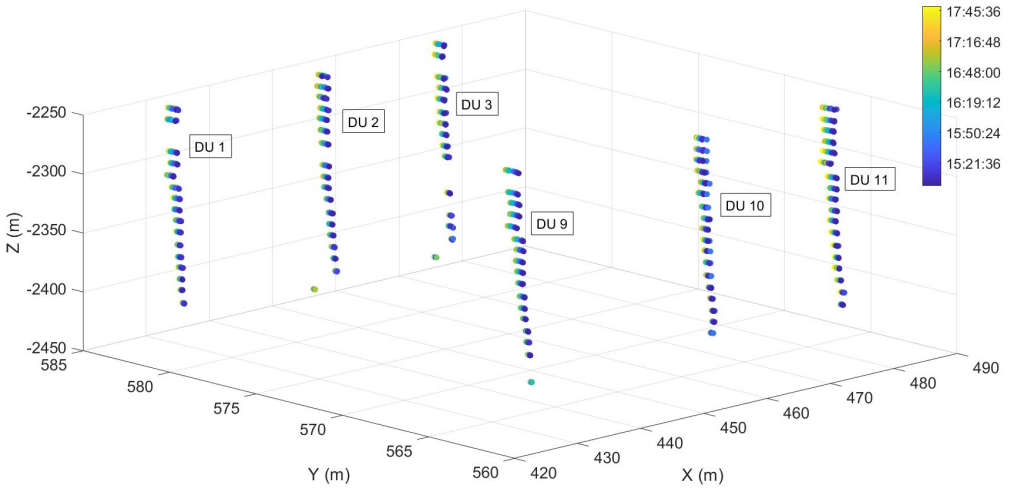

Figure 3.19: Reconstructed positions of 6 ORCA lines during strong sea current period (24/02/2020) - The colours represent the time (from dark blue to yellow - 6 hours in total - duration of a run).

The main approximation made by this algorithm is the calculation of the Times of Emission of the beacons using the nominal positions of hydrophones and emitters (measured during deployment).

In fig. 3.21 we can observe how, by modifying the nominal coordinates of the receivers and beacons within the ORCA uncertainty of 1 m, the solution simply undergoes a shift in the xy plane. As can be seen in fig. 3.22, this effect was predicted by the simulations.

Finally, it is possible to exploit the fixed position of the hydrophones to verify that the error on the measured Times of Arrival is actually 50 μs as estimated in the simulations.

The x and y coordinates of the DU2 hydrophone were reconstructed in the period between 15/08/2019 and 18/08/2019. Then the average was made and the discrepancies between all values and the average were calculated. The resulting distributions are compatible with those obtained with the simulations by setting an error of 50 μs (see fig. 3.23).

This algorithm produced satisfactory results which confirmed the possibility of reconstructing the positions of all the receivers with the necessary accuracy.

3.6.5 Nikhef method

A new version of the algorithm was provided by the KM3NeT group in Nikhef.

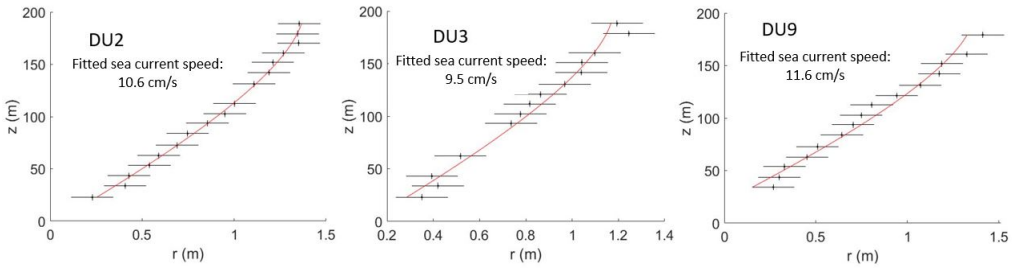

Figure 3.20: Fit of the average positions of the receivers (24/02/2020) - DU2, DU3 and DU9.

A global fit of the acoustic data is performed in which the free parameters are the Times of Emission of the beacons and the tilt angles of each Detection Unit (two for each line).

The other parameters are fixed parameters because in principle they do not vary as a function of time, undergo a tuning process, which exploits the information over time of a selection of runs. They include the coordinates of the bases of the strings, the coordinates of the emitters, the height of each floor of each string, the relative positions of each piezo sensor with respect to the DOM, the relative positions of the hydrophones with respect to the string axis and the parameters which define the variation of the speed of sound as a function of depth.

For small tilt angles, the Times of Arrival can be expressed in terms of a linear dependence on all the free parameters. This allows to obtain a very fast and efficient software.

A comparison between the Approximate method and the Nikhef method was made considering the reconstructed x and y average coordinates of the DOMs. As shown in fig. 3.24 the reconstructed positions with the two different methods are compatible within an uncertainty of 10 cm.

3.7 Conclusions

Different possible approaches to the positioning problem have been tested through simulations and applications to real data providing excellent and satisfying results. As explained in the previous sections, the knowledge of the relative position of the receivers is essential for two different purposes:

- The correct reconstruction of the tracks of the muons that arise from the interactions of neutrinos with the Earth;
- The correct reconstruction of the positions and movements of the cetaceans that emit clicks.

With my algorithm (general method) it was confirmed that the accuracy obtained with the approximate method is sufficient for KM3NeT goals.

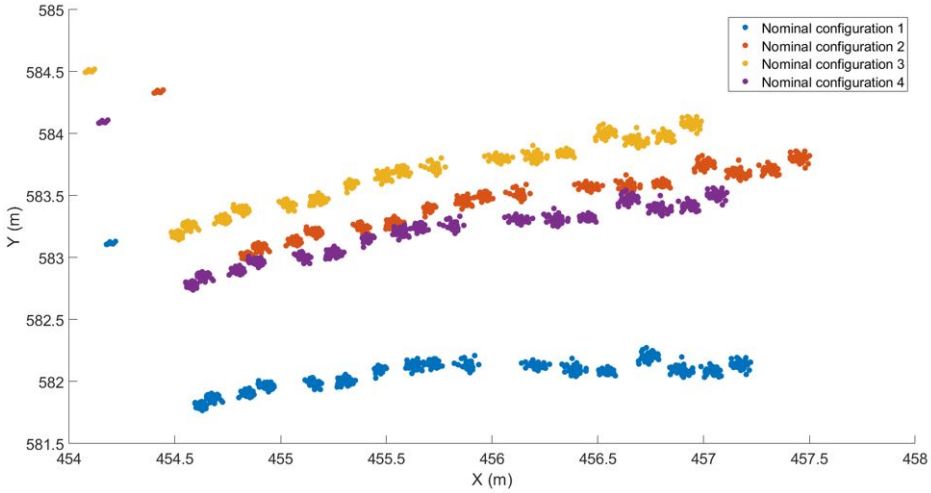

Figure 3.21: DU2 receiver position reconstruction (24/02/2020) using different nominal configuration of hydrophones and beacons extracted within the KM3NeT-ORCA deployment uncertainty of 1 m. The points displaced with respect to the rest of the line represent the position of the hydrophones, which are not aligned with the DU axis.

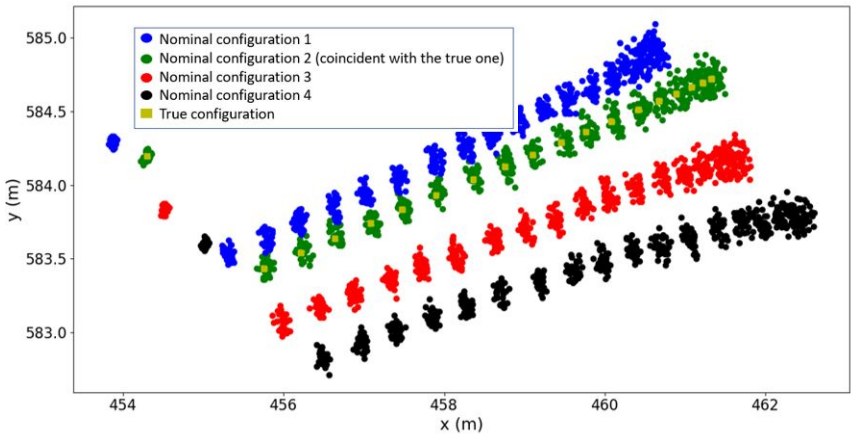

Figure 3.22: DU2 receiver position reconstruction simulation using different nominal configuration of hydrophones and beacons extracted within the ORCA deployment uncertainty of 1 m. The points displaced with respect to the rest of the line represent the position of the hydrophones, which are not aligned with the DU axis.

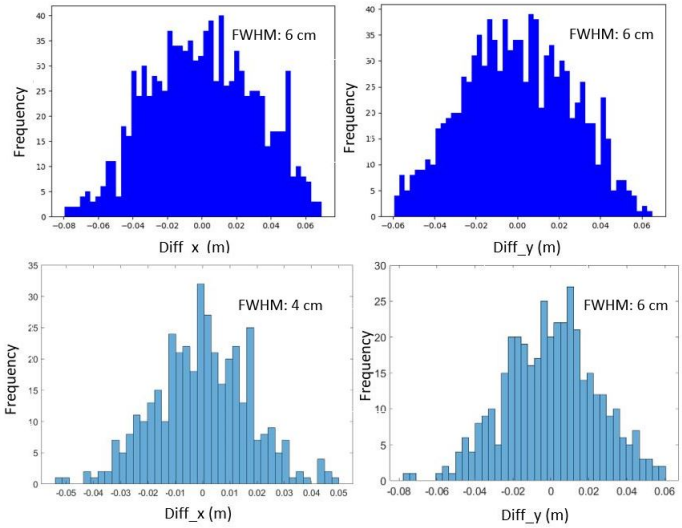

Figure 3.23: Top left and right: respectively X and Y differences between true and reconstructed positions - simulation in which the ToA measurements are affected by 50 μs uncertainty; Bottom left and right: respectively X and Y differences between reconstructed positions and average position in the period between 15/08/2019 and 18/08/2019.

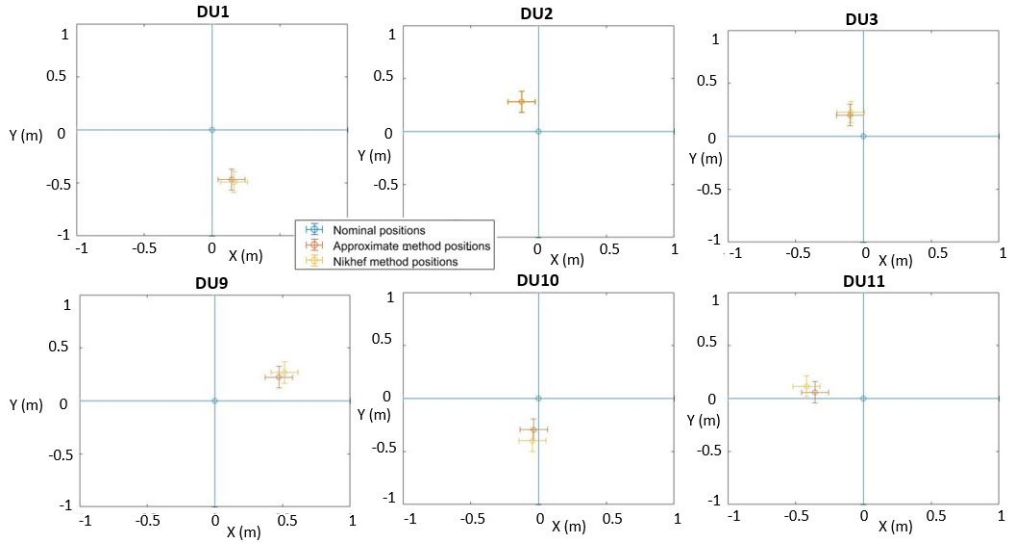

Figure 3.24: Comparison between nominal x and y DOMs coordinates determined during deployment, average x and y DOMs coordinates reconstructed with the approximate method and average x and y DOMs coordinates reconstructed with the Nikhef method during calm sea period (vertical lines).

Chapter 4

Passive Acoustic Monitoring of cetaceans

4.1 Introduction

In this chapter, after an introduction of Passive Acoustic Monitoring of cetaceans, all the research work carried out in the KM3NeT framework to exploit acoustic receivers (hydrophones and piezoelectric sensors) to track and study the behavior of marine mammals will be described.

KM3NeT infrastructure is located in two underwater sites in the Mediterranean Sea, well known for the permanent presence of many species of marine mammals. Each of the numerous Detection Units that will be deployed, as described in sec. 2.2, has on its base a hydrophone capable of detecting acoustic emissions. This feature makes the experiment a great opportunity to study the behavior of these animals, detecting their presence and estimating their position. This kind of study is very important because it could highlight the negative impact that noise pollution and the massive presence of passing ships have on the ecosystem and the habits of these animals.

This chapter will describe the main acoustic characteristics of cetaceans living in the Mediterranean Sea. The correct reception and identification of the sound emissions of marine mammals requires some approximations and presents numerous problems to deal with. I implemented a program for the identification of sperm whale and dolphin clicks using KM3NeT hydrophones. Subsequently, I developed an algorithm to reconstruct the location of the sound source. The simulations necessary for the implementation of the programs and the analysis of the real data of the experiment will be presented.

4.2 Acoustic features of Mediterranean Sea cetaceans

The KM3NeT-ORCA detector is located 40 km offshore the coast of Toulon between the western borders of the Pelagos Cetacean Sanctuary [27] and the Gulf of Lion. This sea area is known to be systematically populated by 9 different cetacean species [28]:

1. fin whale (Balaenoptera physalus),
2. sperm whale (Physeter macrocephalus),
3. long-finned pilot whale (Globicephala melas),
4. striped dolphin (Stenella coeruleoalba),
5. common bottlenose dolphin (Tursiops truncatus),
6. rough-toothed dolphin (Steno bredanensis),
7. cuvier's beaked whale (Ziphius cavirostris),
8. short-beaked common dolphin (Delphinus delphis),
9. risso's dolphin (Grampus griseus).

Cetaceans orient themselves, feed and communicate using a complex system of sound emissions. Thanks to the long sound propagation lengths in water, bioacoustics represents one of the most effective ways to study the behaviour of these animals.

Fin whales typically produce low frequency acoustic emissions that can be divided into two types: descending tones from $21 - 23\,Hz$ to $17 - 18\,Hz$ and constant frequency sounds at around $18 - 20\,Hz$ lasting about $0.8\,s$ [29].

Delphinids (striped dolphin, bottlenose dolphin, Short-beaked common dolphin, Risso's dolphin and Long-finned pilot whale) emit very similar sounds to each other. They can be divided into two main categories: clicks and whistles.

Striped dolphins emit clicks between around $20\,kHz$ and $150\,kHz$ with an interval between them of less than a few tenths of a second. Sometimes these animals also emit very rapid series of clicks, called bursts. The main purposes of the clicks are the orientation and echolocation of the preys. The whistles, on the other hand, have a mainly social and communication purpose between individuals and they present frequencies between a few kHz and more than $20 - 30\,kHz$ [30].

The acoustic behavior of bottlenose dolphins is well known due to the fact that many dolphins of this species are studied in captivity. They emit a wide variety

of whistles and clicks very similar to those of other dolphins and also an impulsive sound called "jaw-clap" (a sound produced by shutting the jaw) [31].

On the contrary, the acoustic emissions of short-beaked common dolphins and rough-toothed dolphins are not much studied due to their rarity, especially in the Mediterranean Sea [30]. Often individuals of short-beaked common dolphins join larger groups of striped dolphins [32]. It is very likely that the sounds emitted are very similar.

The emissions of Risso's dolphins are very similar to those of the other dolphins, but are characterized by a prevalence of clicks also for the communication between the individuals of the group. Clicks are often emitted in very rapid sequences, audible to the human ear as a monotonic sequence [30].

The acoustic behavior of long finned pilot whales is also unknown in detail. There are numerous recordings of clicks for echolocation and whistles that rarely exceed frequencies above $5 - 8\,kHz$ [30].

The acoustic behaviour of Cuvier's beaked whales, belonging to the zyphidae family, is poorly studied. It is known that these cetaceans emit echolocation clicks centered on about $40\,kHz$ when swimming at very high depths [30].

Sperm whales (Physeteridae family) are the cetaceans that emit the most intense sounds (source levels up to $236\,dB\,re:\,1\,\mu Pa\,(rms)$ [33]). It is possible to detect their acoustic emissions and therefore reconstruct position and movements even at very large distances (more than $10\,km$, as shown in sec. 1.3). The sperm whale is the most studied cetacean through Passive Acoustic Monitoring methods and for this reason I will describe its characteristics with more details.

Sperm whales emit clicks for echolocation [34] and communication [35]. During deep dives to get food, these animals emit the so-called "usual clicks", useful for orienting in the search for squid and mesopelagic fish. When they approach a prey, they begin to emit "creacks" [36], which consist of repeated clicks at much shorter intervals of about $20\,ms$ [37]. To communicate with each other, sperm whales emit so-called "codas", which are repetitive clicking patterns [38] and other similar sounds, known as "slow clicks", often coming from adult males.

The most evident physical feature of the sperm whale is the large nasal complex [39] (fig. 4.1), which occupies up to one third of the entire length of an adult male. The whole forehead is widely innervated and it is the part of the animal that has the greatest density of arteries, given the complex system of muscles that control it.

Norris and Harvey [40] hypothesize that the nose of the sperm whale, as for the smaller odontocetes, can be represented as a pneumatic acoustic generator. It consists of a set of cavities, the largest of which is the spermaceti organ [41]. Under the spermaceti organ there is the junk, composed of cavities interspersed with connective tissue. Two nasal passages extend from the separate bony nostrils

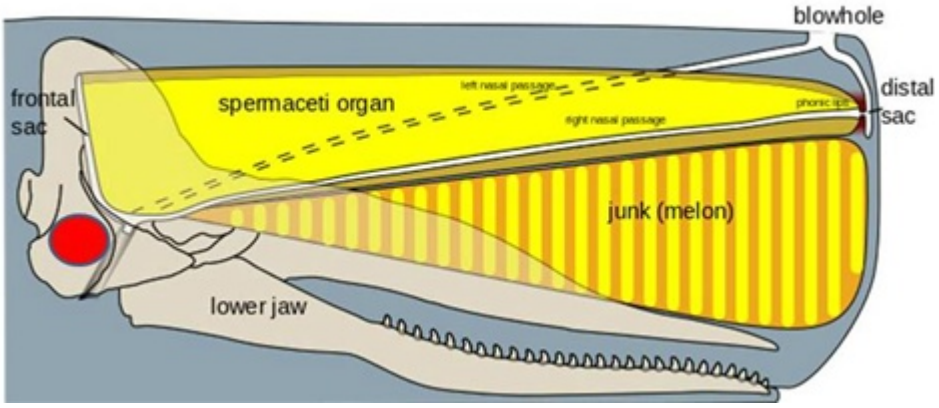

Figure 4.1: Sperm whale nasal complex.

to the vent on the left side of the tip of the nose. The nasal complex of the sperm whale has two air sacs, one on the front of the right duct (distal pouch) and one at the posterior end of the spermaceti organ (frontal pouch). The anterior part of the right nasal passage is surrounded by two flaps of connective tissue, called "monkey lips". This is where the initial sound production takes place. From anatomical observations it was assumed that the initial acoustic generation event is created by pressurized air flowing through the "monkey lips" which slightly open in a short fraction of time. This hypothesis was consistent with the results obtained from numerical models and acoustic recordings [42]. Initially it was thought that most of the sound was transmitted directly into the water in the outgoing direction from the forehead (pulse P0). In the so-called "bent-horn" model [34], only a small fraction of the sound energy of a usual click is released by the animal anteriorly (the P0 pulse). Most of the energy is channeled posteriorly into the spermaceti organ, then reflected on the frontal sac and finally it exits into the water through the junk. This pulse is called P1. The latest studies show that the first sound emission P0 contains only 0.1 % of the energy of the second (P1). A residual part of energy is reflected on the distal sac and crosses the spermaceti organ again, repeating the path. In this way, successive pulses P2, P3, etc. are generated with less and less intensity but at fixed intervals, defining the particular "multi-pulse" characteristic of the sperm whale click (fig. 4.2). The P1 pulse, in addition to being one of the most powerful sounds emitted in the animal world, is strongly directional. The sperm whale's sound generator uses air to get into action. The recycling of the latter allows the animal a continuous emission during the dives. However, the volume of air contained in the internal structures of the animal is reduced as the environmental pressure increases (Boyle's Law: $PV = Constant$). Therefore, the volume of air that can be used for sound production varies considerably with

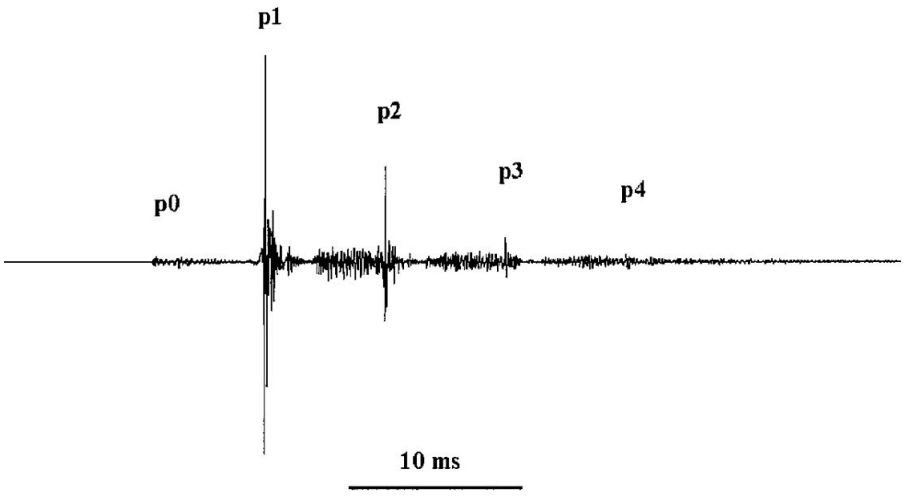

Figure 4.2: Multi-pulse nature of a sperm whale click.

depth.

The distance between two successive pulses of a single click is called "Inter-Pulse Interval" (IPI) and it corresponds to the time that the sound spends to cross the spermaceti organ twice. The IPI is therefore related to the length of the animal. There are two different empirical expressions of this correlation:

Gordon's formula (1987) [43] for small animals ($IPI < 5\,ms$):

$$L[m] = 4.833 + 1.453(IPI[ms]) - 0.009(IPI[ms])^2 \tag{4.1}$$

and Rhinelander and Dawson formula (2004) [44] for larger animals ($IPI > 5\,ms$):

$$L[m] = 17.12 - 2.189(IPI[ms]) + 0.251(IPI[ms])^2 \tag{4.2}$$

The echolocation clicks are emitted with fairly regular sequences. These sequences are typically described by the "Inter-Click Interval" (ICI), which quantifies the temporal separation between clicks emitted by the same animal. For a sperm whale, the ICI has a range that spans from $0.5\,s$ to $2\,s$. Several studies made a frequency analysis of sperm whales clicks, obtaining different results. Watkins (1977) [38] estimated that the energy contained in the sounds emitted by sperm whales was between $100\,Hz$ and $20\,kHz$, with possible peaks between $2\,kHz$ and $6\,kHz$. Other works report frequent peaks around $5\,kHz$ (Backus and Schevill, 1966 [45]), $1\,kHz$ (Bunsel and Dziedzic, 1967 [46]), $2 - 8\,kHz$ (Levenson, 1974 [47]), and $2\,kHz$ (Weilgart and Whitehead, 1988 [48]).

4.3 Cetaceans tracking with KM3NeT hydrophones

Passive Acoustic Monitoring (PAM) techniques are widely used to study the behaviour and estimate the presence and the movements of the cetaceans. As described in sec. 4.2, marine mammals emit a large amount of different sounds. In particular, sperm whale clicks are very directional (source level differences of 35 dB for the same click at different directions were seen [49]) and extremely intense (source levels up to 223 $dB\,re\,1\,\mu Pa\,peRMS$ [49]). For this reason, it is possible to set up acoustic systems composed of hydrophones positioned according to a certain geometry capable of reconstructing the position and movements of these animals.

In this section I will describe the sperm whale and dolphin click identification program that I implemented. Subsequently, the results of the simulations of the KM3NeT-ORCA acoustic system will be presented, aimed at estimating the accuracy of the source position reconstruction with different configurations of the acoustic receivers. Finally, the results of the application of the system to the real KM3NeT-ORCA data will be shown.

4.3.1 Click identifier

Click identifier algorithm

The first phase of the acoustic data analysis for a cetacean Passive Acoustic Monitoring system is the identification of the sounds emitted by the animals.

In particular, the goal of this study is the implementation of a program that is able to identify generic clicks of cetaceans and divide them into two macro-groups: sperm whale clicks and dolphin (striped dolphin, common bottlenose dolphin, short-beaked common dolphin) clicks (see fig. 4.3).

The scientific literature [30] provides the information about the main differences between the clicks emitted by sperm whales and dolphins. The main parameters by which these two categories differ are:

- Inter Click Interval (ICI)
- Click shape and duration
- Frequency range

Typical Dolphin Inter Click Interval varies between a few milliseconds (when hunting and feeding) to $100 - 200\,ms$ (when traveling and socializing) [30] [50]. In contrast, the Inter Click Interval of sperm whales varies between $500\,ms$ and approximately $2\,s$ [51].

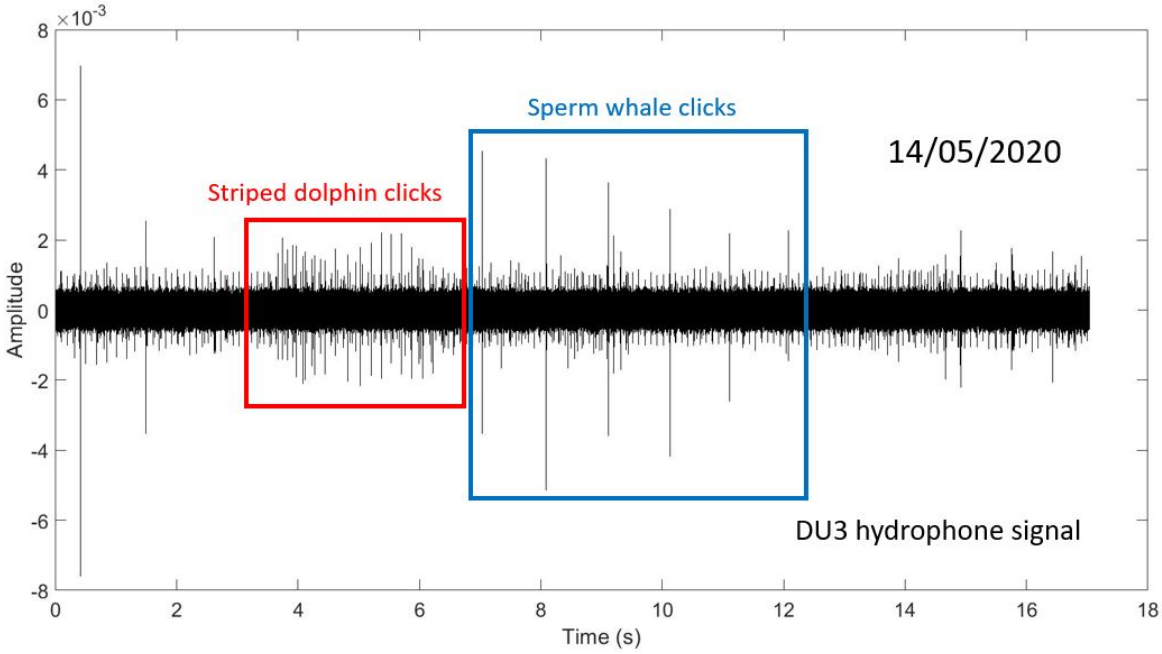

Figure 4.3: Dolphin and sperm whale clicks detected by KM3NeT-ORCA DU3 hydrophone on 14/05/2020.

In fig. 4.4 two examples of striped dolphin and sperm whale clicks trains, recorded by one of the KM3NeT-ORCA hydrophones, are shown.

Sperm whale and dolphin clicks also differ in the shape of the click (see fig. 4.5). In particular, the duration of a dolphin click is generally shorter than that of a sperm whale click. However, this is not the most useful information to distinguish the two types of emissions, as it strongly depends on the quality of the signal reception in relation to the distance and orientation of the animal with respect to the hydrophone.

The most relevant difference in order to discriminate between the two types of clicks is the frequency range [30]. Dolphin clicks present a frequency range between 20 and 150 kHz. On the contrary, sperm whales emit clicks with a typical frequency range between a few kHz and $20 - 30\,kHz$ (see fig. 4.6).

This information was used to implement the cetacean click identification program. The first step consists in evaluating the spectral characteristics of the raw acoustic signal recorded by the KM3NeT-ORCA hydrophones.

As shown in fig. 4.7, the hydrophone signal presents electronic noise bands between 48 kHz and 87 kHz. These almost monochromatic noise sources do not influence the cetacean click detection.

The underwater background noise is concentrated at low frequencies, between 0 and 5 kHz. The signal, however, is dominated by the 50 Hz noise (and multiples:

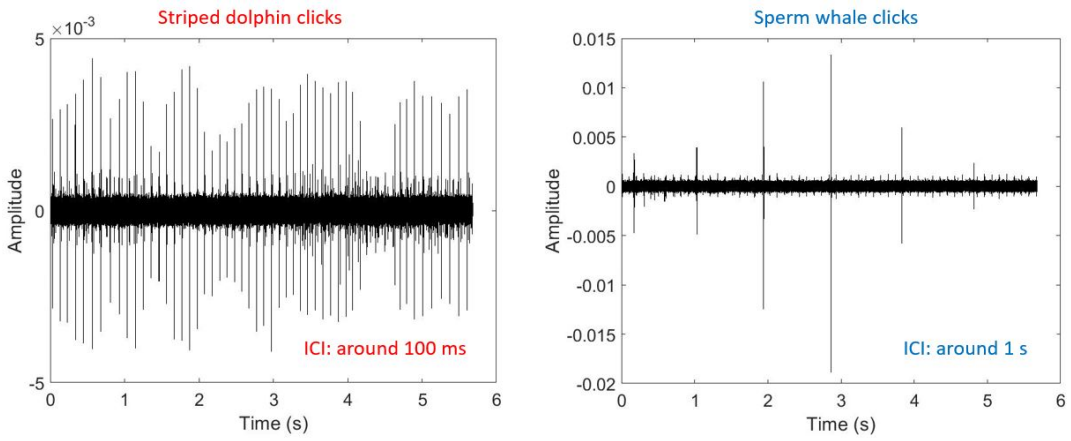

Figure 4.4: Comparison between dolphin and sperm whale clicks trains detected by DU3 KM3NeT hydrophone on 14/05/2020.

100 Hz etc.) caused by the ACDC converter. For these reasons, in order to detect marine mammal clicks with an acceptable signal to noise ratio (SNR), it was necessary to preprocess the acoustic data by applying a high pass filter with a 2 kHz cutoff frequency. The choice of this value is driven by the fact that sperm whale clicks can have energy peaks starting from a few kHz. As we will see in the next paragraph, this parameter, empirically set, represents the best solution to minimize the loss of signals.

The ACDC converter also produces another noise source, visible in fig. 4.7 as vertical lines repeated every $100\,ms$. This is a cross-talk sequence of high and low voltage from the ACDC digital communication line (RS232) polluting hydrophone signal. This background is not a problem for the click identification because it does not exceed the SNR threshold set empirically in the detection program.

The raw acoustic data are stored as $\sim 5\,s$ files. The first action of the click identifier consists of splitting the file into $0.15\,s$ time windows with an overlap of $50\,\%$ in order to avoid losing signals covering two adiacent windows.

The program analyzes each time interval in two consecutive steps:

1. Time domain analysis

2. Frequency domain analysis

For each time window the Signal to Noise Ratio (SNR) as a function of time is calculated, taking as a reference noise the median of the absolute value of the envelope (Hilbert function) of the signal.

In each time window a click is detected if there is a value of SNR greater than 10 times the median of all the SNR values in that time window (SNR threshold).

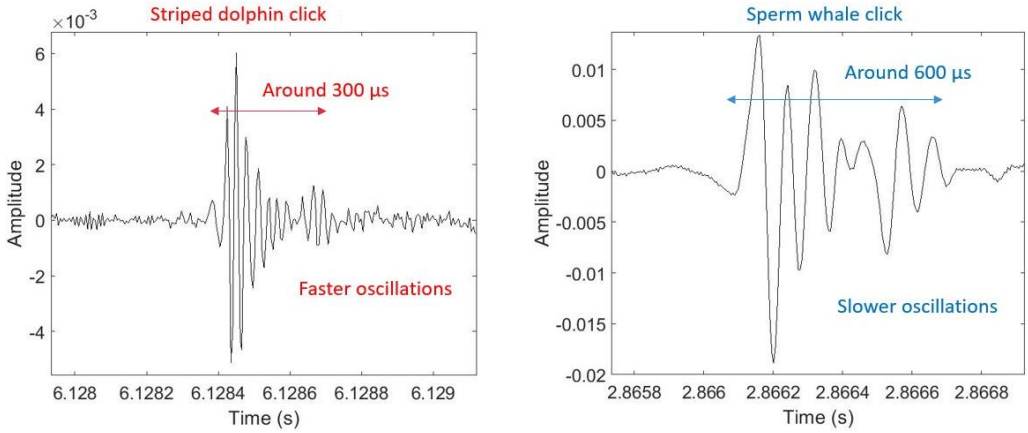

Figure 4.5: Comparison between dolphin and sperm whale single clicks detected by DU3 KM3NeT hydrophone on 14/05/2020.

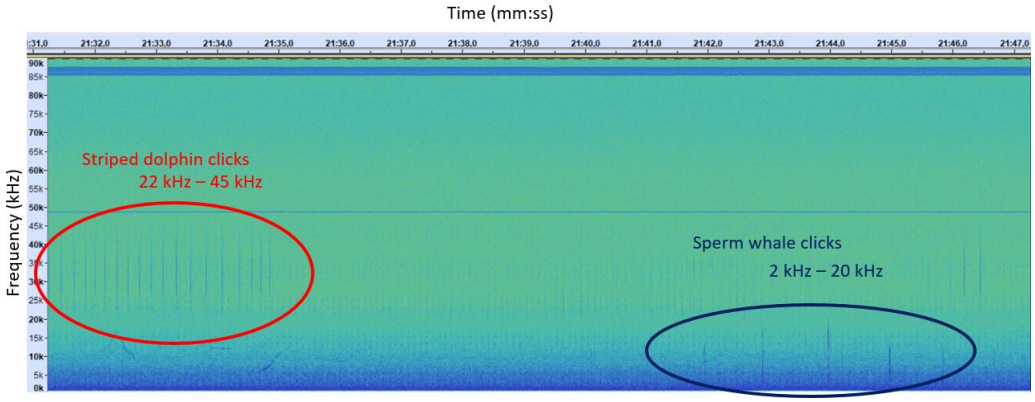

Figure 4.6: Spectrogram of dolphin and sperm whale clicks recorded by DU3 KM3NeT hydrophone on 14/05/2020.

The value of the threshold is empirical. In fig. 4.8 the signal as a function of time of one hydrophone file with some sperm whale clicks is shown. The value of the SNR threshold is over the level of the digital penetrations. The intensity of the clicks is variable and it depends on the species that are emitting the sound and its distance from the hydrophone system. The program was tested on different acoustic files in which clicks of cetaceans with different intensities were detected. By setting this value for the SNR threshold on average only around 10 % of the clicks identified by eye are lost. By reducing the threshold value below the value of 10, the number of detected signals increases, but random peaks of background noise are also wrongly misidentified as clicks.

Thereafter, the time intervals are analyzed in the frequency domain. A segment

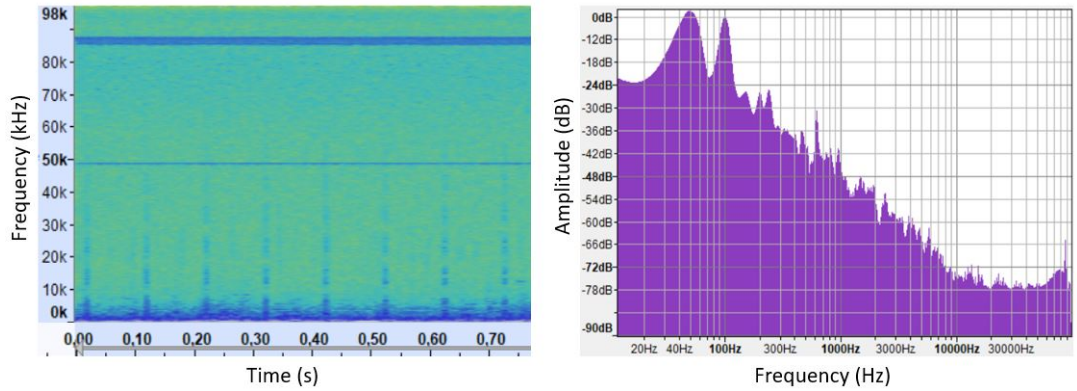

Figure 4.7: At the left the spectrogram of deployed DU3 hydrophone signal is shown. Electronic noise bands at $48\,kHz$ and $87\,kHz$ are visible. The vertical lines every $100\,ms$ are digital penetrations due to the ACDC converter. At the right the spectrum of the deployed DU3 hydrophone signal, calculated in a period of $0.7\,s$, is shown in a logarithmic plot. The $50\,Hz$ and multiples noise is clearly visible.

of the same duration of the time windows, in which only background noise is present, is isolated and the Fast Fourier Transform (FFT) is calculated.

The amplitude of the FFT at the frequencies between $5\,kHz$ and $20\,kHz$ (typical sperm whale frequencies), $20\,kHz$ and $50\,kHz$ (typical striped dolphin frequencies) and between $5\,kHz$ and $50\,kHz$ (generic cetacean clicks) is taken and saved in different arrays. This amplitudes will be used as reference values for the noise thresholds.

The time windows in which the SNR exceeds the threshold are selected and the FFT of the signal is calculated considering the amplitude between 5 kHz and 50 kHz.

The values of the FFT of the signal are compared with the reference amplitudes of the FFT of the noise. If at least 20 % of them are bigger than the noise thresholds at the different frequencies, a click is assumed in that time window. After numerous tests on KM3NeT-ORCA acoustic files containing sperm whales and dolphins signals, a percentage threshold of 20 % was identified as the best compromise to detect the largest possible number of clicks without counting false positives.

The sperm whale and dolphin clicks are distinguished by observing whether the amplitude of the FFT is greater, respectively, between $5\,kHz$ and $20\,kHz$ or between $20\,kHz$ and $50\,kHz$.

After the time domain and frequency domain analysis, additional empirical filters are applied.

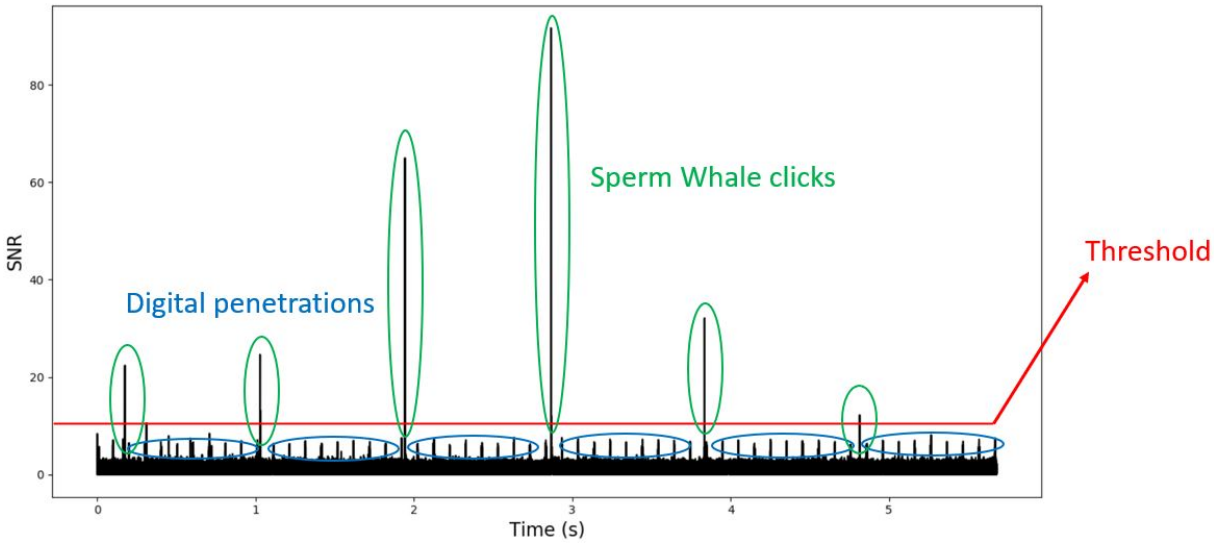

Figure 4.8: SNR as a function of time for the signal of a hydrophone KM3NeT-ORCA file with some sperm whale clicks. The SNR threshold is over the SNR level of the ACDC digital penetrations and allows to detect the most part of the clicks visible by eye.

Each file has a time duration of about 5.5 s. As already illustrated, the typical Inter Click Interval of a sperm whale click is between 0.5 s and 2 s, but, as we will see, most of the clicks observed by KM3NeT have an interclick interval between 0.7 s and 1.5 s. For this reason, in order to exclude possible false positives during noisy runs, I decided to validate only the files with a number of clicks between 3 and 7 (extremes estimated by calculating the ratio between the duration of a file and the minimum and maximum values of the Inter Click Interval).

Moreover, I discard sperm whale clicks if the standard deviation of the Inter Click Intervals is greater than 0.2 s. This is an empirically set value, considering the fact that the clicks typically are very regular over time during echolocation activities (standard deviation of around 0.1s maximum).

On the other hand, I validate dolphin clicks only if we have more than 5 clicks in a file (interclick interval of around $100 - 200\,ms$ or less). I have empirically observed that click sequences with less than 5 pulses can be false positives.

In fig. 4.9 a summary scheme of the click identifier is shown. With this program it has been demonstrated the possibility to detect dolphin and sperm whale clicks with excellent accuracy, as we will see in the next paragraph.

A further filter, in particular for sperm whale clicks, will be the search for the matching signals in the different hydrophones, a useful technique to distinguish real signals from electronic noise.

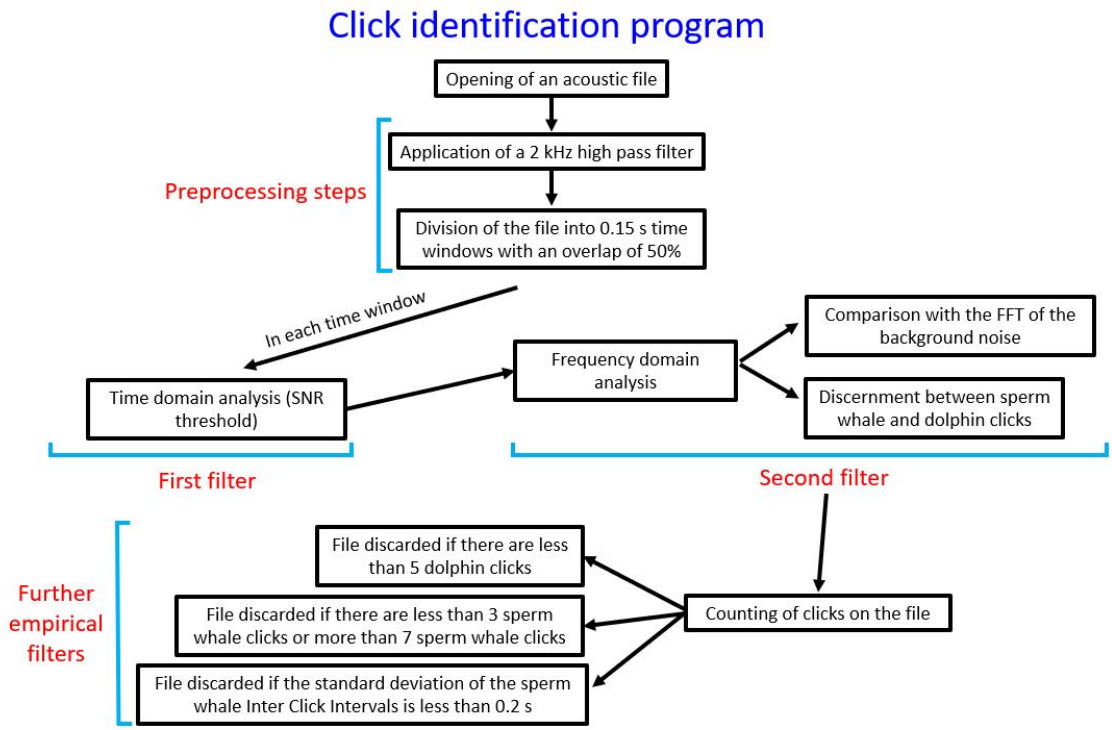

Figure 4.9: Summary scheme of the click identification program.

Furthermore, also the reconstruction of the trajectories of the acoustic sources can be a further discriminating factor in the identification of different sources.

Applications of the click identifier to the real data

The click identifier program was tested on real KM3NeT-ORCA data. As shown in fig 4.10., if we apply the click identifier to a noisy run, which has numerous amplitude spikes, the click identifier correctly does not find cetacean clicks. In fig. 4.11 and fig. 4.12, on the other hand, it is possible to observe the results of the application of the algorithm to two runs in which there are respectively numerous dolphin clicks and numerous sperm whale clicks. The number of clicks identified by the program was compared with the number of clicks counted by eye in different acoustic data sets and an efficiency of approximately 90 % was estimated.

The click identifier program was applied to the KM3NeT-ORCA acoustic data stored between April 2020 and July 2021.

In fig. 4.13 the number of dolphin clicks per hour detected as a function of time is shown. The presence of dolphins in the area is consistent throughout the year. The smaller number of points during the Summer, Autumn and Winter months is due to the less frequent recording of the acoustic data. In fact, where there is

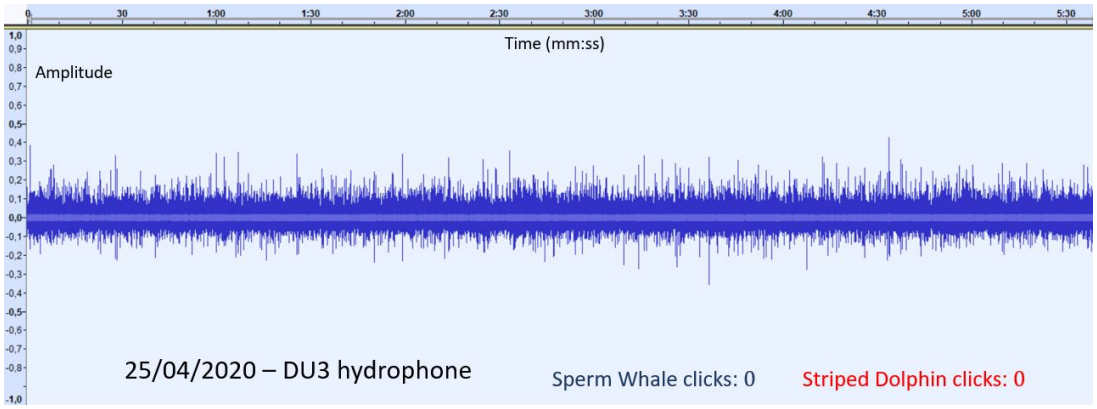

Figure 4.10: Application of the click identifier to a noisy run 5 minutes and 30 seconds period - 25/04/2020

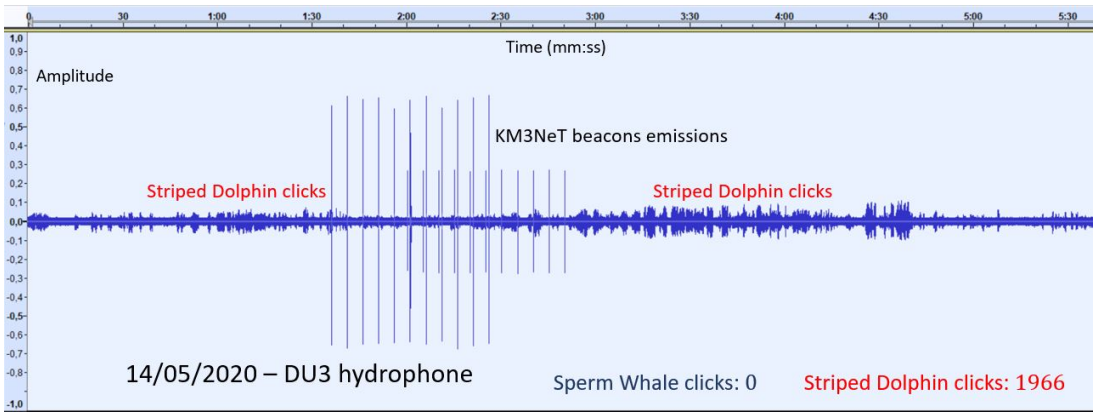

Figure 4.11: Application of the click identifier to a 5 minutes and 30 seconds period with numerous dolphin detections - 14/05/2020

higher data density, the data taking was continuous. In the other periods, however, only two hours a week of data were stored.

In fig. 4.14 the number of sperm whale clicks per hour detected as a function of time is shown. Also in this case we can guess that sperm whales are present throughout the year. There are three evident holes, the first between the end of May and the end of June 2020, the second between the first days of July and the middle of August 2020 and the last one between February and May 2021. However, this is probably due to the data density in those periods. In any case, it is realistic that in some periods the presence of sperm whales in a certain area is less due to the fact that these animals can migrate during the year occupying different areas [52].

We cannot be certain about the presence of cetaceans during the periods when

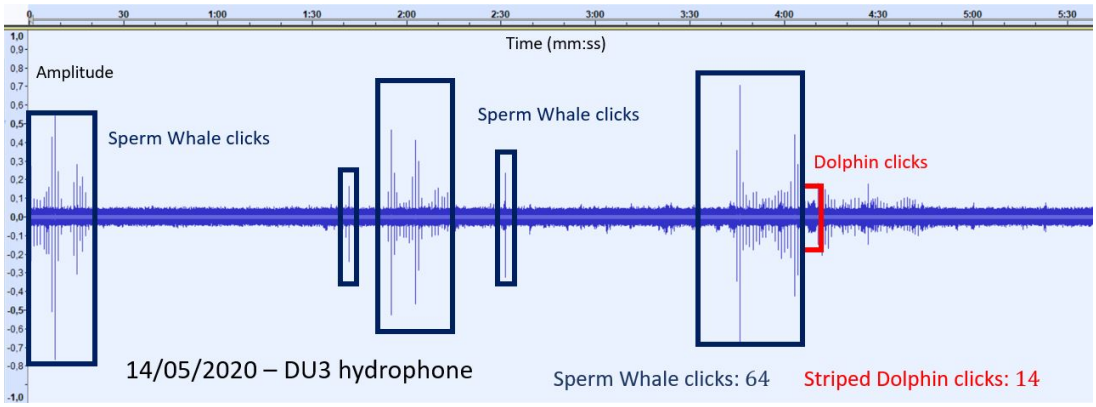

Figure 4.12: Application of the click identifier to a 5 minutes and 30 seconds period with numerous sperm whale detections - 14/05/2020

only 2 hours of datataking per week were saved. However, every time continuous data were set (between April and May 2020, May 2021 and July 2021), sperm whale and dolphin clicks were systematically detected. This result indicates a consistent presence of these cetaceans in the Gulf of Lion area.

Studies in the literature show that echolocation activity through the emission of clicks is mainly concentrated during nighttime for dolphins [53] [54] and during daytime for sperm whales [55].

The acoustic data of KM3NeT confirmed this trend as regards the sound signals emitted by sperm whales (see fig. 4.15, left). On the contrary, the number of dolphin clicks detected as a function of time appears to be distributed more uniformly over the different hours of the day (see fig. 4.15, right). Most likely the amount of available data is not sufficient to highlight the phenomenon.

4.3.2 Position reconstruction simulations

The second phase of a cetacean Passive Acoustic Monitoring system is the reconstruction of the source location.

Sperm whales are the best candidates for this analysis because they emit extremely intense directional clicks.

In this section I will describe the algorithm chosen to reconstruct the position of the animals analyzing the acoustic data and I will show the results of the simulations of the KM3NeT-ORCA receiver system in order to highlight its performance.

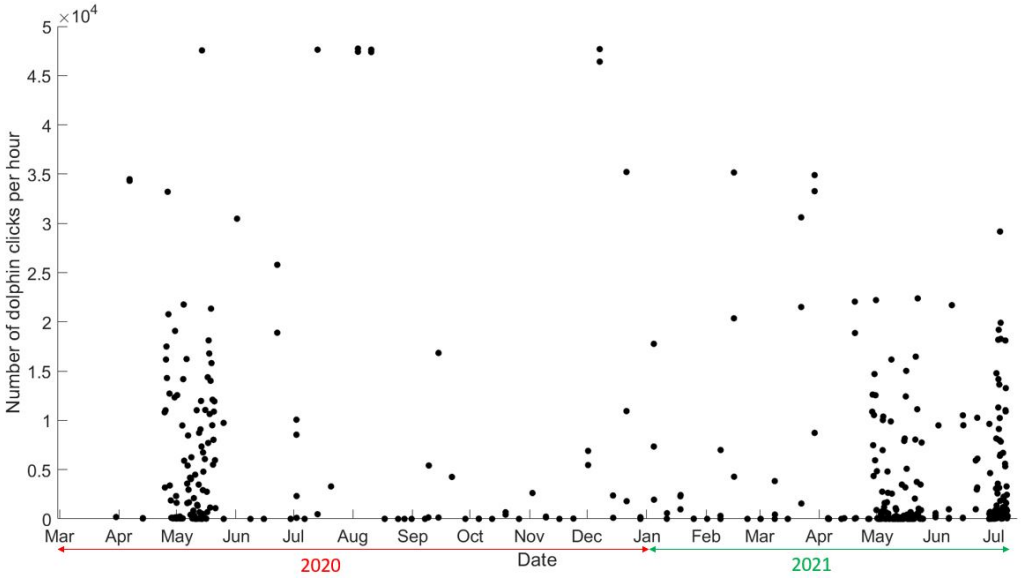

Figure 4.13: Number of dolphin clicks per hour detected between April 2020 and July 2021.

Position reconstruction algorithms

Let us consider a set of hydrophones $h_i, i = 1, \dots M$ at positions $(x_i\, y_i\, z_i)$ and an acoustic source at the coordinates $(x_w\, y_w\, z_w)$. The individual ranges between source and the hydrophones are defined as:

$$R_i = R_0 + \delta R_i \tag{4.3}$$

where R_0 is the distance between the source and a hydrophone chosen as reference and $\delta R_i = c\delta T_i$. δT_i is the time delay between the reception of the signal by the hydrophone i and the reference hydrophone and c is the effective sound speed between the two hydrophones.

We can express in this way the square of the distance between the hydrophones and the whale:

$$R_{wi}^2 = (x_i - x_w)^2 + (y_i - y_w)^2 + (z_i - z_w)^2 \tag{4.4}$$

We therefore get:

$$R_0^2 = x_0^2 - 2x_0x_w + x_w^2 + y_0^2 - 2y_0y_w + y_w^2 + z_0^2 - 2z_0z_w + z_w^2 \tag{4.5}$$

and

$$R_0^2 + 2R_0\delta\ R_i + \delta R_i{}^2 = x_i^2 - 2x_ix_w + x_w^2 + y_i^2 - 2y_iy_w + y_w^2 + z_i^2 - 2z_iz_w + z_w^2 \tag{4.6}$$

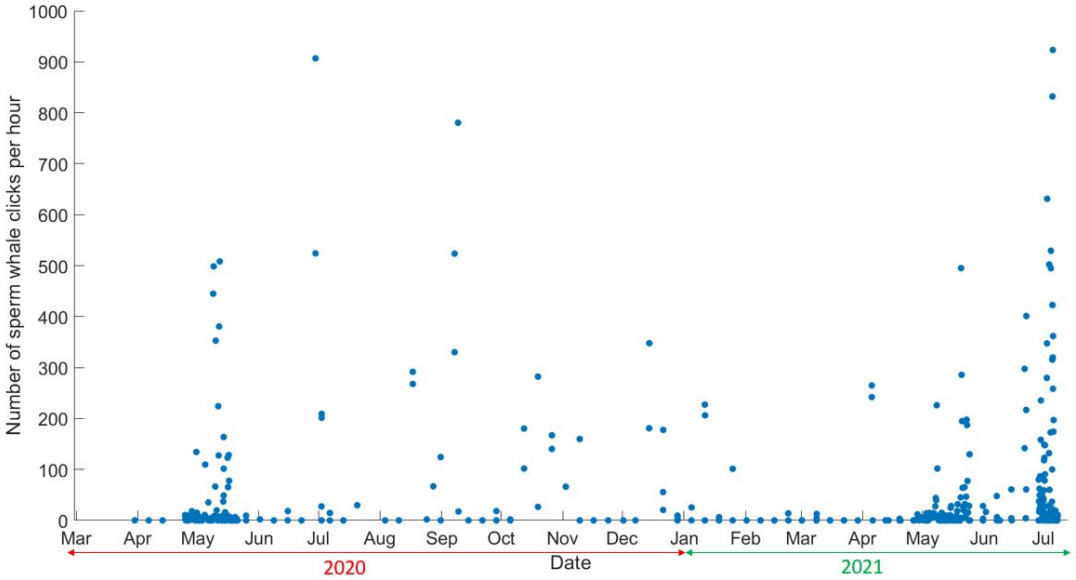

Figure 4.14: Number of sperm whale clicks per hour detected between April 2020 and July 2021.

From eq. 4.5 and eq. 4.6 we obtain:

$$2R_0\delta\, R_i+\delta R_i{}^2 = x_i^2-x_0^2-2\,(x_i-x_0)\,x_w+y_i^2-y_0^2-2\,(y_i-y_0)\,y_w+z_i^2-z_0^2-2\,(z_i-z_0)\,z_w \tag{4.7}$$

Eq. 4.7 has 4 unknowns (R_0, x_w, y_w and z_w) and with 5 hydrophones we can form 4 equations:

$$\begin{pmatrix} (x_1^2-x_0^2)+(y_1^2-y_0^2)+(z_1^2-z_0^2)-(\delta R_1)^2 \\ (x_2^2-x_0^2)+(y_2^2-y_0^2)+(z_2^2-z_0^2)-(\delta R_2)^2 \\ (x_3^2-x_0^2)+(y_3^2-y_0^2)+(z_3^2-z_0^2)-(\delta R_3)^2 \\ (x_4^2-x_0^2)+(y_4^2-y_0^2)+(z_4^2-z_0^2)-(\delta R_4)^2 \end{pmatrix} = 2\begin{pmatrix} \delta R_1 & (x_1-x_0) & (y_1-y_0) & (z_1-z_0) \\ \delta R_2 & (x_2-x_0) & (y_2-y_0) & (z_2-z_0) \\ \delta R_3 & (x_3-x_0) & (y_3-y_0) & (z_3-z_0) \\ \delta R_4 & (x_4-x_0) & (y_4-y_0) & (z_4-z_0) \end{pmatrix} \begin{pmatrix} R_0 \\ x_w \\ y_w \\ z_w \end{pmatrix} \tag{4.8}$$

Actually, the unknown R_0 is dependent on the other 3 unknowns (x_w, y_w and z_w). Its introduction is necessary to have a well suited problem for a Least-Mean-Square (LMS) method.

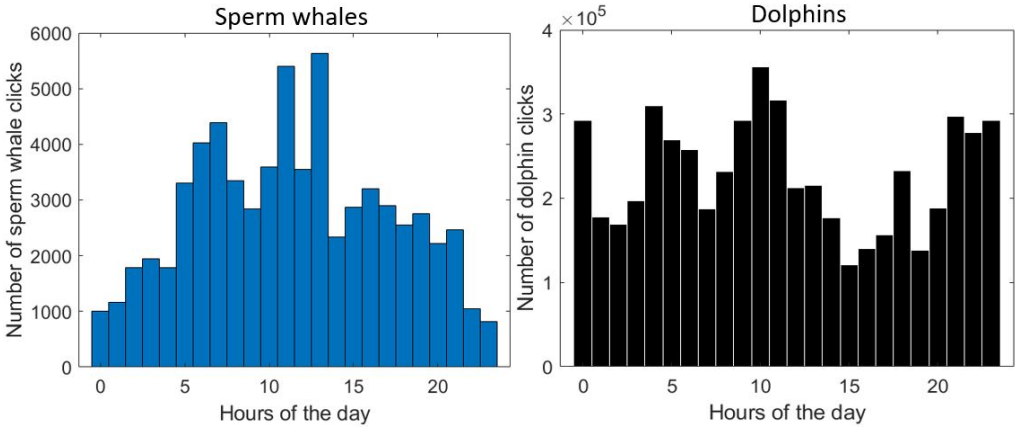

Figure 4.15: At left distribution of the detected sperm whale clicks in the different hours of the day. At right distribution of the detected dolphin clicks in the different hours of the day.

In order to apply this algorithm it is important that not all sensors are at the same depth, otherwise the five hydrophones would not form a strict volumetric array. In the case all sensors are at the same depth, we get:

$$\begin{pmatrix} (x_1^2 - x_0^2) + (y_1^2 - y_0^2) - (\delta R_1)^2 \\ (x_2^2 - x_0^2) + (y_2^2 - y_0^2) - (\delta R_2)^2 \\ (x_3^2 - x_0^2) + (y_3^2 - y_0^2) - (\delta R_3)^2 \end{pmatrix} = 2 \begin{pmatrix} \delta R_1 & (x_1 - x_0) & (y_1 - y_0) \\ \delta R_2 & (x_2 - x_0) & (y_2 - y_0) \\ \delta R_3 & (x_3 - x_0) & (y_3 - y_0) \end{pmatrix} \begin{pmatrix} R_0 \\ x_w \\ y_w \end{pmatrix} \tag{4.9}$$

and we can estimate the whale depth z_w by:

$$z_w = z_0 \pm \sqrt{R_0^2 - (x_w - x_0)^2 - (y_w - y_0)^2} \tag{4.10}$$

This method ensures excellent results if the relative positions between the hydrophones are exactly known. Otherwise, it is possible that the choice of the reference hydrophone has a not negligible influence on the final result, as we will see later by observing the output of the simulations. In KM3NeT-ORCA the relative position between the receivers is known with an accuracy of around 10 cm. For these reasons it was necessary to implement an algorithm that does not depend on the choice of a reference hydrophone, whose position could possibly have been reconstructed not accurately. The following equation has been used, according to which the speed of sound at the seabed multiplied by the delay time between

the reception of the signal by two hydrophones i and j is equal to the difference between the distances of these two hydrophones and the acoustic source:

$$c_s \cdot \Delta t_{ij} = \sqrt{(x_i - x_w)^2 + (y_i - y_w)^2 + (z_i - z_w)^2} - \sqrt{(x_j - x_w)^2 + (y_j - y_w)^2 + (z_j - z_w)^2} \tag{4.11}$$

where the receivers i and j are couples of consecutive hydrophones and the last couple is formed by the last receiver and the first one. In this way we have a number of equations equal to the number of hydrophones and the theoretical minimum number of receivers is reduced to four. This method is more robust than the previous one because it is less dependent on different uncertainties on the hydrophone relative positions. For both the methods the minimization is performed using the LMS function of the scipy Python library [56].

Results of the simulations

Simulations of the position reconstruction algorithms have been performed considerig different geometrical configurations of the receivers and comparing the two methods described in the previous paragraph.

The simulations were carried out considering 3 different geometric configurations of the receivers:

1. The Autumn 2021 configuration of KM3NeT-ORCA, consisting of 5 seabed hydrophones plus a hydrophone on the Calibration Base (CB) at $1.19\,m$ above the seabed (fig. 4.16, left top);

2. The future KM3NeT-ORCA configuration, consisting of 16 seabed hydrophones plus the CB hydrophone (fig. 4.16, left bottom);

3. A geometric configuration consisting of 4 seabed hydrophones and two receivers at different altitudes ($50\,m$ and $100\,m$ with respect to the seabed) (fig. 4.16, right).

Configuration 3 was chosen to investigate the possibility of using some of the less sensitive piezo sensors, which are located at different altitudes on the surface of the DOMs.

The first simulation was exploited to demonstrate that method 2, the algorithm without reference hydrophone, produces better results than method 1 if the position of the reference hydrophone is not estimated accucurately.

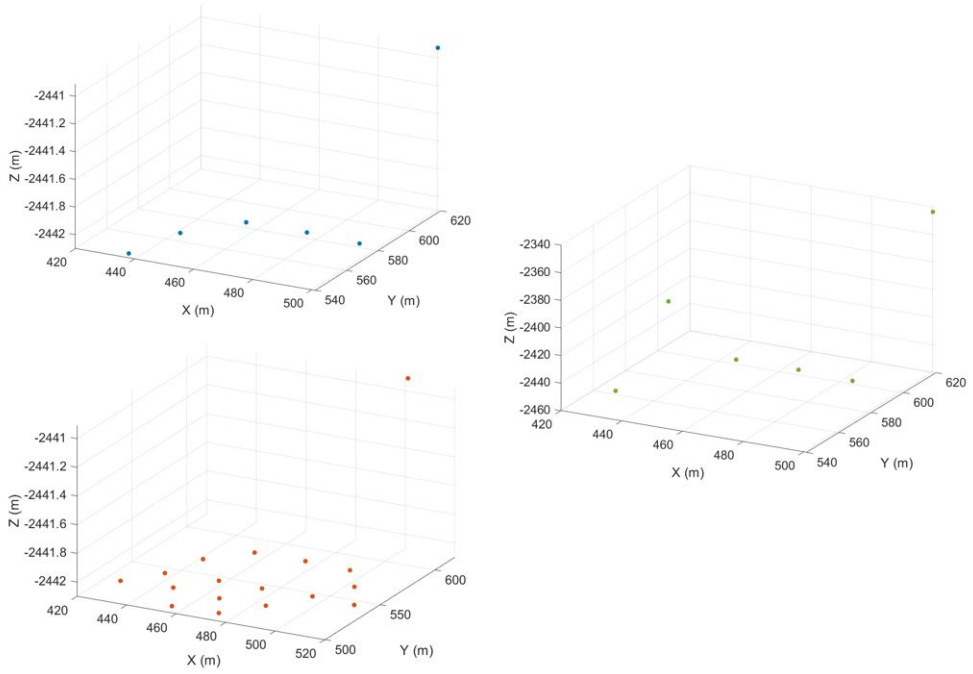

Figure 4.16: Three different geometrical configurations of the receivers tested in simulations.

For this test, the geometric configuration 1 was used and the whale position was fixed at $(x, y, z) = (3000, 1000, -800)\, m$. 1000 different measurements were simulated, extracting for each iteration x, y and z coordinates of the receivers within a $30\, cm$ uncertainty for the reference hydrophone and within a $5\, cm$ uncertainty for the other receivers.

The delay time of the signal reception between all the hydrophones couples was calculated, taking into account the variations of the speed of sound due to the hydrostatic pressure.

Then, the source positions were reconstructed using the two methods described in the previous paragraph and the distributions of the reconstructed x, y and z are plotted in order to compute the corresponding Full Width Half Maximum (FWHM).

As shown in fig. 4.17, the method 2 produces better results (FWHMs 30 % lower with respect to method 1), so it has been chosen for the position reconstruction.

The following simulations were performed in order to estimate the accuracy of the reconstruction algorithm for the three different possible configurations of the receivers presented before.

For this purpose, the azimuth and zenith angles of the source were fixed ($\theta = 85°$, $\varphi = 45°$) and the distance between the acoustic source and the system of

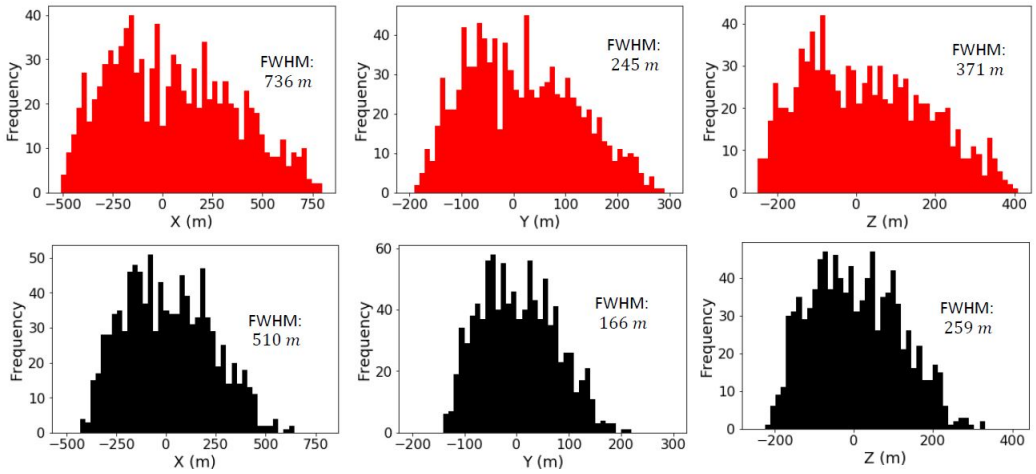

Figure 4.17: Distributions of the 1000 reconstructed x, y and z whale coordinates with method 1, with the reference hydrophone, (in red) and method 2, without the reference hydrophone, (in black). The receiver coordinates are extracted within a 30 cm uncertainty for the reference hydrophone and within a 5 cm uncertainty for the other sensors. The source position is fixed at $(x, y, z) = (3000, 1000, -800)\, m$. The smaller values of the FWHMs of black distributions demonstrate that the method without reference hydrophone is more reliable if the position of one of the receivers is accidentally affected by a larger error.

hydrophones varied between 1000 m and 10000 m.

The position of the source was reconstructed using the second method described before, without using a reference hydrophone, and the percentage error on the distance obtained with the minimization was calculated.

For each source position this process was repeated for 100 different configurations of the receivers, obtained extracting the hydrophones coordinates within the uncertainty of 10 cm, the positioning system accuracy. Then, the average percentage error on the distance was extrapolated.

The results of the simulation are shown in fig. 4.18. It is evident that the configuration 1, composed of only seabed hydrophones, does not provide sufficient accuracy to reconstruct the trajectories of the sperm whales. On the contrary, both by increasing the number of hydrophones positioned on the seabed or by using acoustic receivers at different altitudes and therefore by increasing the three-dimensionality of the system, excellent results are reached (percentage error less than 10 % for a distance of 6 km).

At present (Summer 2021) there are only 3 seabed hydrophones, but there are 108 piezoelectric sensors located at different altitudes on the DOMs.

Piezoelectric sensors are less sensitive than seabed hydrophones. However, the

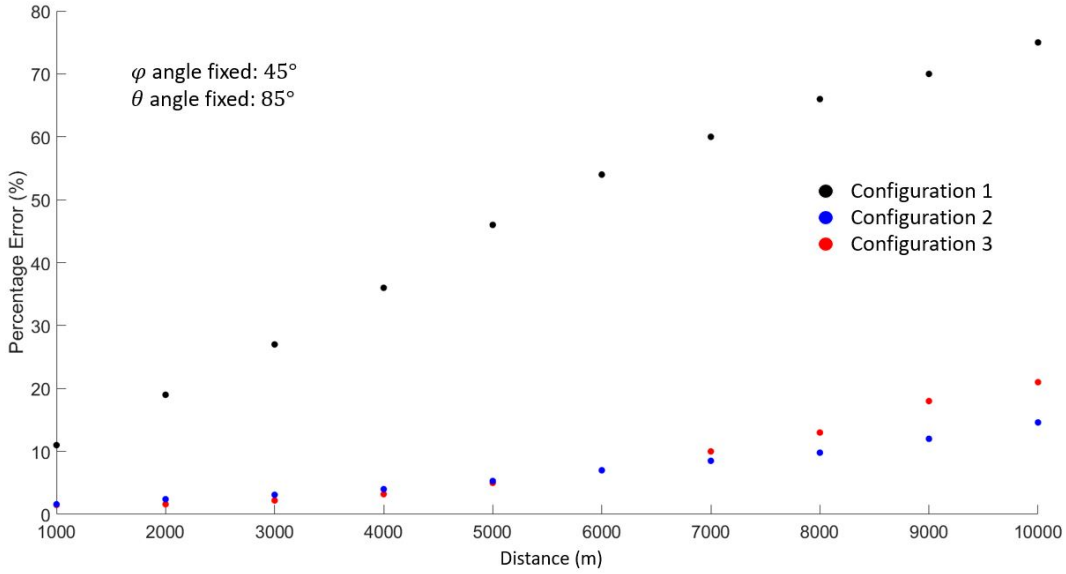

Figure 4.18: Simulation results: percentage error as a function of the distance of the whale (source zenithal and azimuthal angles fixed) for three different configurations. The black points refer to a configuration with 5 seabed hydrophones plus the CB hydrophone, the blue points refer to a configuration with 16 seabed hydrophones plus the CB hydrophone, the red points refer to a configuration with 4 seabed hydrophones plus 2 acoustic receivers at different altitudes (50 m and 100 m with respect to the sea bottom).

most intense sperm whale clicks can also be detected by these receivers.

For these reasons, with the goal to reconstruct the trajectory of the sperm whales present during the Summer of 2021, it was necessary to understand which configuration of hydrophones plus piezoelectric sensors was the most appropriate to reach the best accuracy.

The uncertainty on the reconstruction depends on four different factors:

1. the location of the Detection Units involved,
2. the numbers of receivers,
3. the uncertainty on the position of the receivers,
4. the position of the source.

In principle, the best configuration should be made up of all the available receivers. However, for disk space reasons, we cannot store continuously all the

acoustic data. It was, therefore, necessary to make a selection of piezo sensors to use for the whale position reconstruction.

As a first test, the number of receivers and the DUs involved were keep fixed.

Five different configurations counting twelve receivers were tested, considering the three hydrophones available during Summer 2021 and adding piezo sensors at different altitudes:

1. 3 seabed hydrophones, 1 piezo sensor at an altitude of $28.8\,m$, 4 piezo sensors at an altitude of $113.9\,m$ and 4 piezo sensors at an altitude of $189.0\,m$;

2. 3 seabed hydrophones, 1 piezo sensor at an altitude of $28.8\,m$, 4 piezo sensors at an altitude of $65.5\,m$ and 4 piezo sensors at an altitude of $189.0\,m$;

3. 3 seabed hydrophones, 1 piezo sensor at an altitude of $28.8\,m$, 4 piezo sensors at an altitude of $65.5\,m$ and 4 piezo sensors at an altitude of $113.9\,m$;

4. 3 seabed hydrophones, 1 piezo sensor at an altitude of $28.8\,m$, 4 piezo sensors at an altitude of $170.8\,m$ and 4 piezo sensors at an altitude of $189.0\,m$;

5. 3 seabed hydrophones, 1 piezo sensor at an altitude of $28.8\,m$, 4 piezo sensors at an altitude of $47.2\,m$ and 4 piezo sensors at an altitude of $86.0\,m$;

In the simulation a delay time error of $10\,\mu s$ was considered and 1000 different positions of the receivers were extracted within the $10\,cm$ uncertainty, which is the typical accuracy of the positioning system. The location of the acoustic source was fixed at $(x, y, z) = (3000, -4000, -300)\,m$.

The coordinates of the whale position were reconstructed without using a reference hydrophone (method 2) and the Full Width Half Maximum (FWHM) of the distribution of the 1000 iterations was calculated.

As shown in fig. 4.19, the configuration 1 is the optimal, with a FWHM for x coordinate of around $146\,m$. These notable differences are due to the geometry of the system of receivers. On average, the greater distance between the receivers, the more accurate the reconstruction is. In configuration 1, for instance, the vertical distances between the receivers of the same line are always greater than $75\,m$. This does not happen in the other four configurations, where there are receivers of the same line at shorter distances each other.

Also the dependance on the source position has been investigated. Four different whale locations, arranged symmetrically with respect to the receivers, have been tested, showing that for configuration 1 the accuracy does not depend on the azimuth angle of the source (see fig. 4.20).

Moreover, by increasing the number of receivers up to 24 (adding sensors of different lines at the same altitudes), we do not get a substantial improvement (see fig. 4.21).

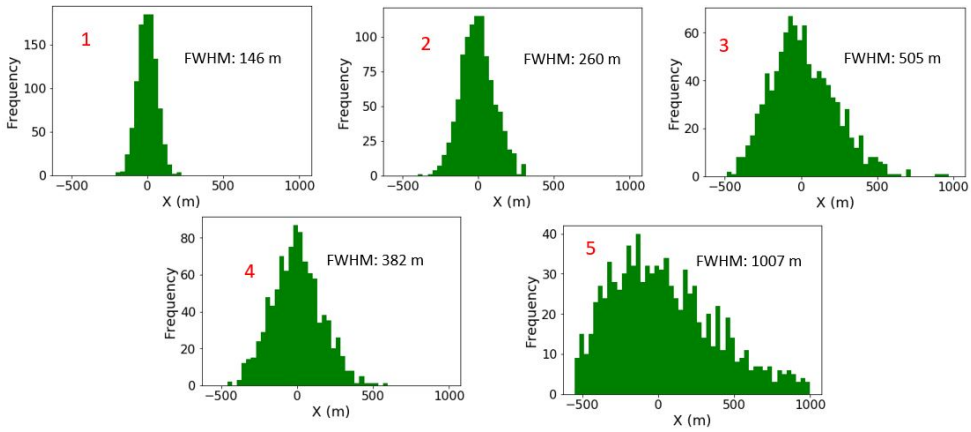

Figure 4.19: Distributions of 1000 reconstructed whale x coordinates. The receiver coordinates are extracted within a 10 cm uncertainty, the acoustic positioning system accuracy. The source position is fixed at $(x, y, z) = (3000, -4000, -300)\, m$. The FWHM is calculated for the five receiver configurations described in this paragraph.

For all these reasons, 2 hours per week of acoustic raw data recorded by the receivers of configuration 1, composed of 12 sensors, was stored during Summer 2021. In sec. 4.3.4, the search of sperm whale signals in this data samples will be presented.

4.3.3 9 September 2020 sea calibration campaign analysis

On 9 September 2020, a sea campaign was organized above the KM3NeT-ORCA site aimed at testing and calibrating the three working hydrophones present at that time.

An emitter was placed under the boat at a depth of approximately 2.3 m. The acoustic emissions consisted of one ping every second ($5 - 15\, kHz$ chirp with a duration of 20 ms, fig. 4.22) for a period of approximately 2 h.

The position of the boat during the acoustic campaign was measured by DGPS (Differential Global Positioning System) with an accuracy of around 0.2 m (fig. 4.23).

The acoustic data recorded by the hydrophones have been used to test the position reconstruction system and verify the reliability of the measured Times of Arrival of the sound waves.

The emitter depth was considered fixed at 2.3 m. The unknown variables of the system, therefore, are only 2, the coordinates x and y of the emitter. For this purpose 3 hydrophones are sufficient to reconstruct the position of the acoustic source, because we restricted 1 degree of freedom (the source depth is known).

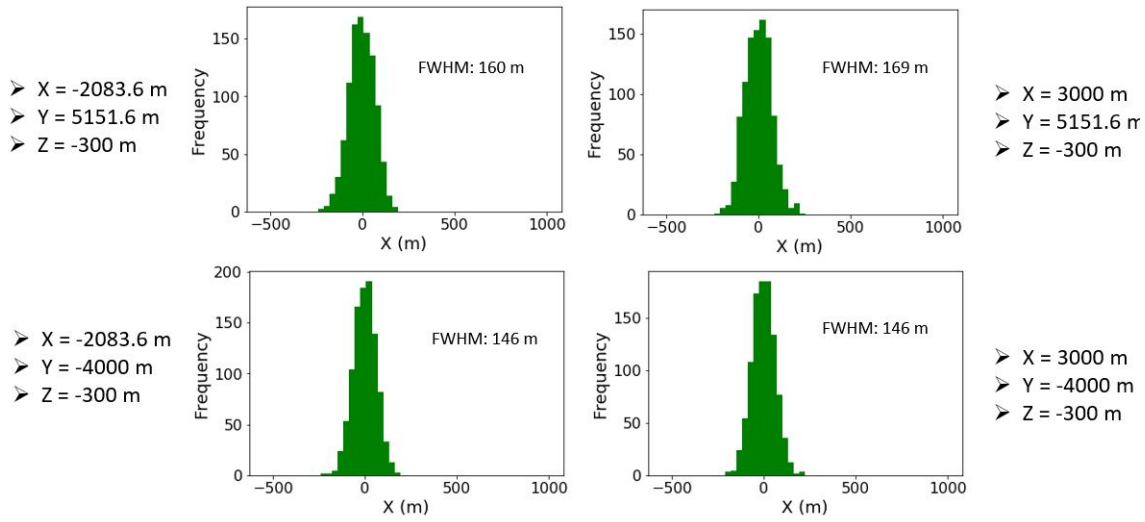

Figure 4.20: Distributions of 1000 reconstructed whale x coordinates. The receiver coordinates are extracted within a 10 cm uncertainty, the acoustic positioning system accuracy. Four different whale positions, arranged symmetrically with respect to the receivers, have been simulated. The FWHM is calculated for the four source locations.

The measurement of the delay times between the arrival of the chirps at the different receivers allows the reconstruction of the source position. The raw acoustic files were divided into time windows of 1 s in which the chirps were recognized using a SNR threshold and a frequency range based threshold (similarly to the click identifier, see sec. 4.3.1). The delay times were calculated by cross correlating the corresponding time windows of the signal of the different hydrophones.

Considering two signals x and y that differ only by a shift on the time axis, the cross-correlation can be calculated to show how much y must be anticipated to make it identical to x. The cross correlation function calculates the integral of the product of the signals for each possible value of the displacement:

$$R_{fg}(t) = \int_{-\infty}^{\infty} f^*(\tau)\, g(t+\tau)\, d\tau \tag{4.12}$$

where x^* is the complex conjugate of the signal x.

When the two signals coincide, the value of the cross correlation function is maximum, since when the waveforms are aligned they contribute only positively to the calculation of the area.

In our specific case the signals do not differ only for a time shift, as they are recorded by different sensors. Despite this, it is possible to use the cross correlation function to evaluate their similarity. In order to calculate the delay

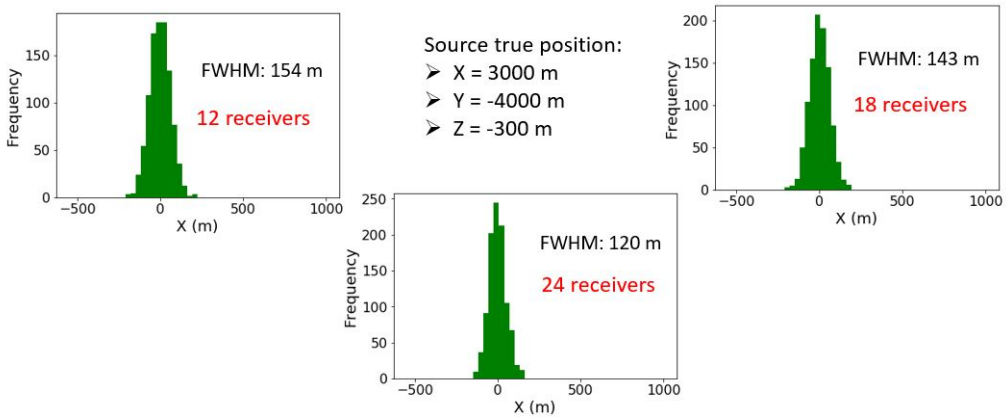

Figure 4.21: Distributions of 1000 reconstructed whale x coordinates. The receiver coordinates are extracted within a 10 cm uncertainty, the acoustic positioning system accuracy. The source position is fixed at $(x, y, z) = (3000, -4000, -300)\, m$. The FWHM is calculated for three different receiver configurations with an increasing number of sensors (12, 18 and 24).

time between the signals, it is sufficient to calculate the distance on the x axis between the maximum of the cross correlation function and the abscissa on which it is centered.

On a practical level we have to calculate:

$$Time\ Delay = \frac{\frac{len(xcorr)}{2} - pos(max_{xcorr})}{sf} \tag{4.13}$$

where $len(xcorr)$ is the number of points in which the cross correlation function is calculated, $pos(max_{xcorr})$ is the abscissa at which the maximum of the cross correlation function is found and sf indicates the sampling frequency of the acoustic data acquisition system.

The value of the maximum of the cross correlation function is taken as Quality Factor and an empirical threshold is set ($qf > 10000$). It has been observed that threshold values below 10000 could validate random correlations of the background noise. On the contrary, there are no correlations between true signals that give a Quality Factor less than 10000.

As input for the position reconstruction algorithm we must use the speed of sound at the seabed ($1546.36\, m/s$) and the coordinates x, y and z of the hydrophones. In order to test the system I used as receiver locations the nominal positions determined during the deployment of the strings, the output of the approximate method (see sec. 3.6.2) and the output of the Nikhef method (see sec. 3.6.5).

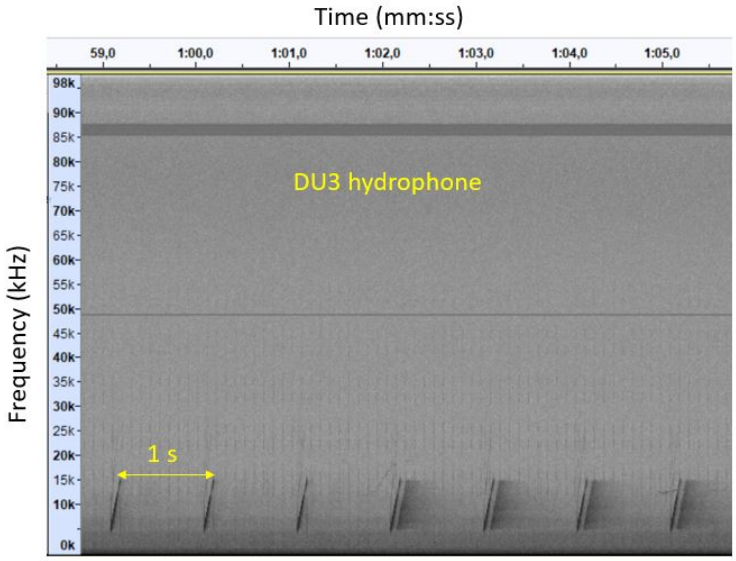

Figure 4.22: Spectrogram, from DU3 hydrophone signal, in which the $5 - 15\,kHz$ chirps emitted during the sea campaign of 09/09/2020 are visible. Starting from 1 minute and 2 seconds also the reflections of the signals on the seabed are present.

The position of the boat was reconstructed using method 2 described in sec. 4.3.2 using the data of the 3 available hydrophones. In fig. 4.24 are shown the results of the reconstruction in the 3 areas highlighted in fig. 4.23 (1, 2 and 3b) and using as input the three different sets of positions of the receivers just presented. As shown in the plots, the closest track to the position of the boat recorded by the GPS is different in the three areas. Each of the three receiver configurations appears to be the best in different areas. This result was obtained because systematic errors (such as ray bending due to the variation of the speed of sound with depth) and measurement errors, due to the accuracy of the positioning system, have not yet been considered.

For these reasons, these effects have been studied. The output of the approximate method of the positioning system was chosen as the reference configuration of the receivers. 100 different receiver positions were chosen by extracting the coordinates x, y and z within the $10\,cm$ uncertainty and imposing a slope of the seabed between $-0.5°$ and $+0.5°$. The results are shown in fig. 4.25 demonstrating that this uncertainty alone is sufficient to obtain a boat track compatible with the track reconstructed with the GPS.

Subsequently, the ray bending effect was also considered. In fig. 4.26 the deviation of the sound rays along the direction on the horizontal plane between source and receiver as a function of the zenith angle of the source is provided.

For each point of the boat track the zenith angle was calculated and the correc-

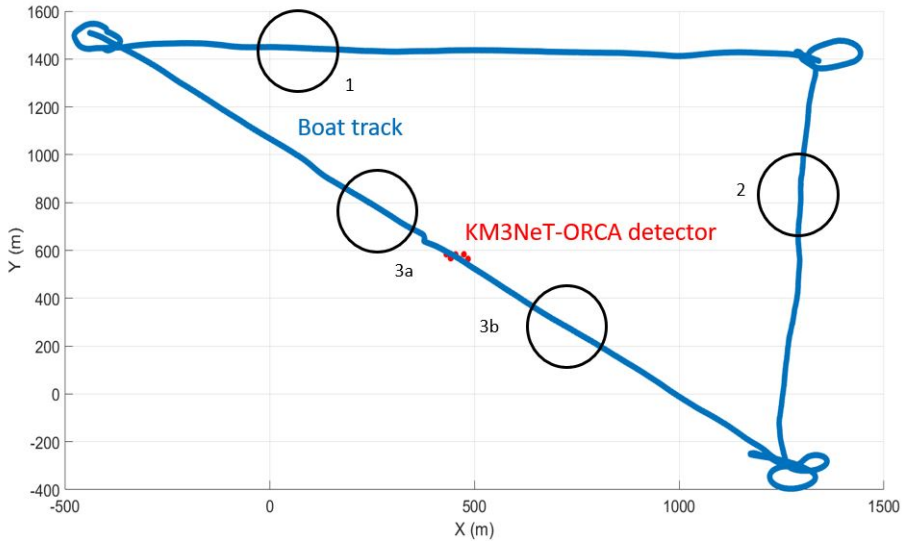

Figure 4.23: x-y plot of the boat track recorded by the DGPS during the sea campaign of 09/09/2020. Circled in black segments in different areas of the boat route chosen for subsequent tests on the position reconstruction through the acoustic signal recorded by the hydrophones.

tion to be applied on the reconstructed positions was extrapolated from the plot in fig. 4.26.

In order to find the correct position of the hydrophones I extracted 10000 configurations of the receivers smearing randomly the x and y coordinates within $10\,cm$, the x and y seabed slope within $0.5°$ and the altitude of the seabed within $10\,cm$ (9 parameters). Then, for each configuration, I reconstructed all the boat positions and I applied the ray bending correction to each point. The best arrangement of the receivers is the one that minimzes the following function:

$$f_{conf} = \sum_{i=1}^{N_{points}} \left[min\left(d_i\right)\right]^2 \tag{4.14}$$

where N_{points} is the number of reconstructed points and $min(d_i)$ is the shortest distance between the reconstructed point i and the GPS boat track.

In fig. 4.27 the results of this analysis are shown. The track reconstructed starting from the best configuration of the receivers, after applying the ray bending correction, coincides with the track of the boat recorded by the GPS with a maximum error of around $5\,m$. The average distance between the reconstructed points and those measured by the GPS is $5.1\,m$ before applying the ray bending correction and $2.5\,m$ after applying the correction. This demonstrates the reliability of the used method. In the area closest to the hydrophone system, as expected,

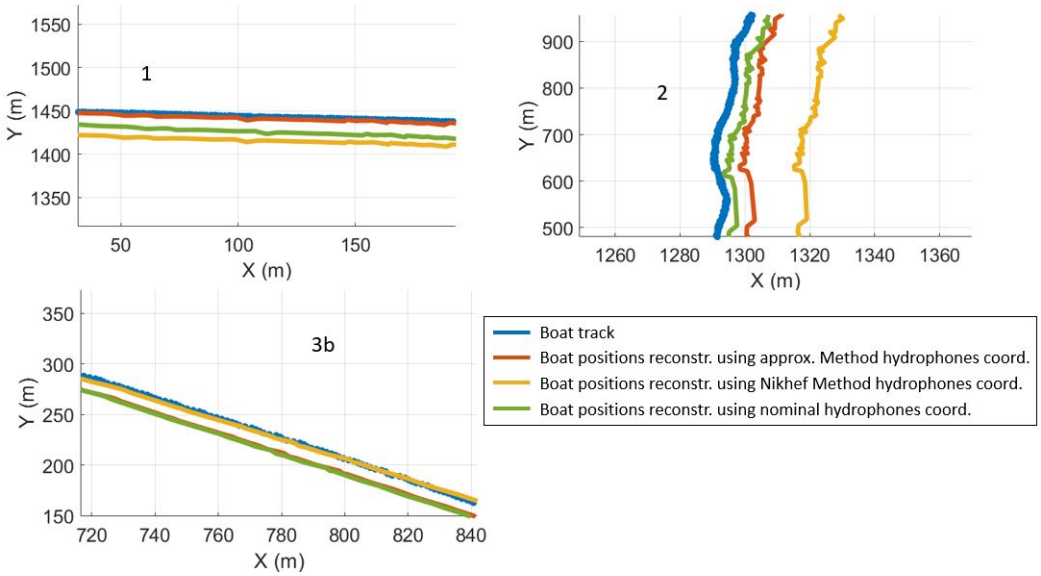

Figure 4.24: Boat positions in three different areas reconstructed using as input three different sets of receiver locations (nominal values, approximate method output, Nikhef method output).

ray bending correction does not affect the measurements. The error in that area probably depends on other systematic factors, such as the measurement error on the Times of Arrival of the sound rays, the sea wave motion and the uncertainty on the emitter depth.

The boat route has been reconstructed with an accuracy of few metres. Consequently, this analysis demonstrated the reliability of the Times of Arrival (ToA) values extrapolated from the signal of the different hydrophones and the functionality of the algorithm that has been implemented for reconstructing the position of an acoustic source. In sec. 4.3.4 we will see the application of this system aimed at reconstructing the position of sperm whales, whose clicks were recorded during the Summer of 2021.

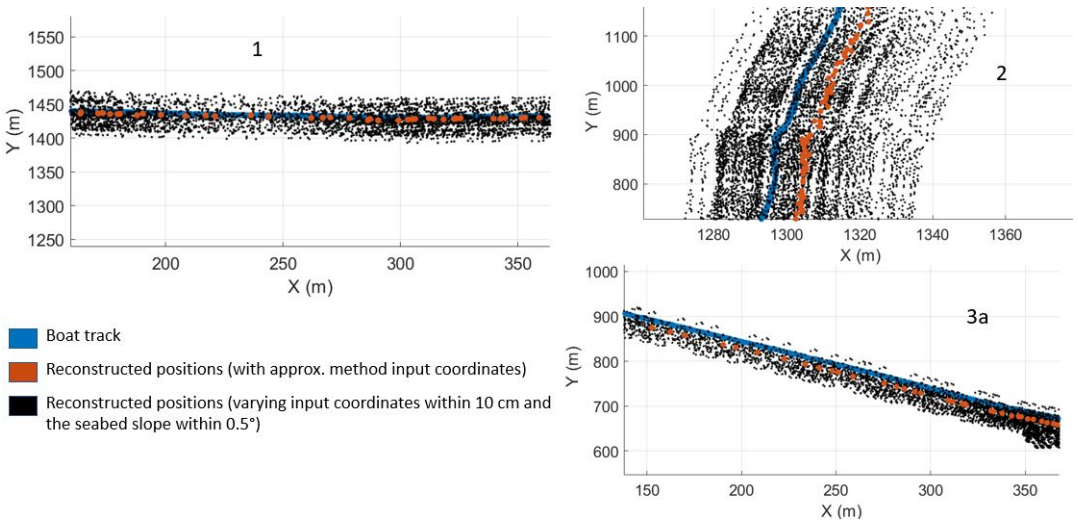

Figure 4.25: Boat positions in three different areas (fig. 4.23 (1, 2 and 3a)) reconstructed using as input 100 different sets of receiver locations obtained extracting the coordinates x, y and z within the $10\,cm$ uncertainty and imposing a slope of the seabed between $-0.5°$ and $+0.5°$.

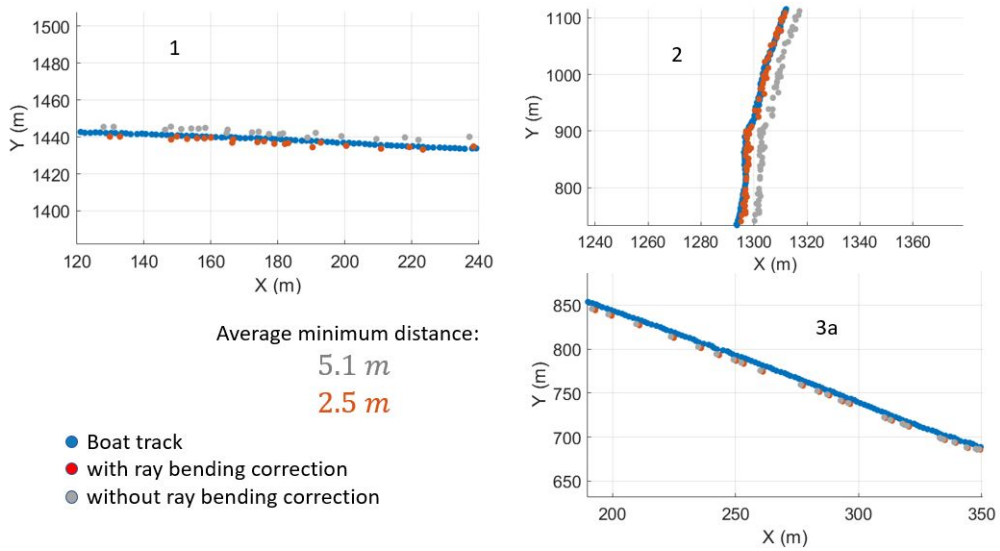

Figure 4.27: Boat positions in three different areas (fig. 4.23 (1, 2 and 3a)) reconstructed using as input the approximate method receiver coordinates. The red track is obtained after applying the ray bending correction. The gray track is obtained without applying the ray bending correction.

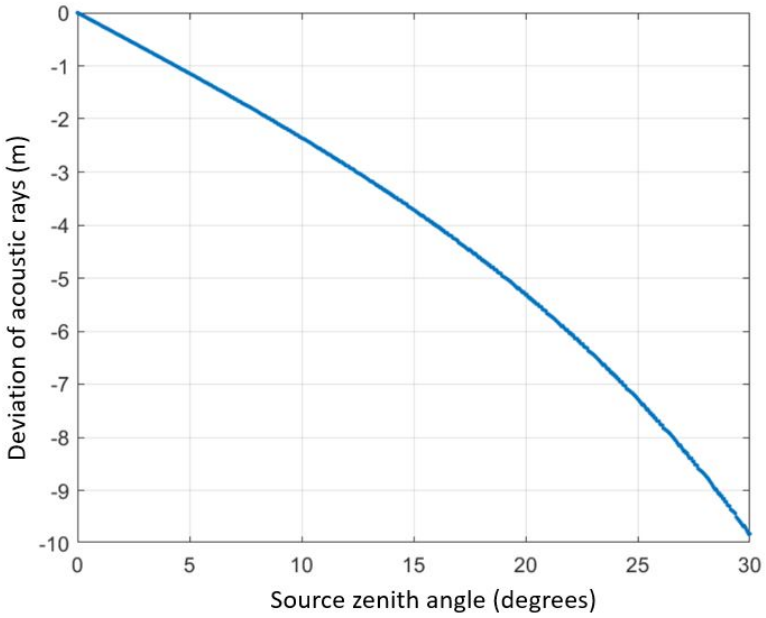

Figure 4.26: Deviation of the sound rays along the direction on the horizontal plane between source and receiver as a function of the zenith angle of the source.

4.3.4 Acoustic raw data analysis

For disk space reasons not all raw data from the KM3NeT acoustic receivers are stored for offline analysis:

- From middle of April 2020 to middle of May 2020 and during May 2021, the data from four 6 hours runs a day with only the hydrophones signal (DU2, DU3 and DU9) has been continuously recorded.
- From middle of May 2020 to middle of December 2020, each week a 10 minute run was saved on disk containing the raw acoustic data of 12 receivers (2 hydrophones and 9 piezoelectric sensors).
- From middle of December to the end of Summer 2021, the data from one 1 hour run a week with the signal of 3 hydrophones (DU2, DU3 and DU9) and 6 piezos (best configuration described in sec. 4.3.2) has been stored.
- Finally, from 28/06/2021 to 12/07/2021 a continuous data taking with the signal of 3 hydrophones (DU2, DU3 and DU9) and 6 piezos (best configuration described in sec. 4.3.2) has been set up.

The click identification program was applied to the entire dataset showing the

number of detected dolphin clicks and sperm whale clicks as a function of time (see sec. 4.3.1).

The large number of clicks trains detected made it possible to perform a statistical analysis on the Inter Click Interval (ICI) of the sperm whale clicks, defined as the temporal distance between two consecutive pulses.

The typical values of the ICI for sperm whale regular clicks are between $0.5\,s$ and $2\,s$ [57]. However, when the animal detects a prey, the frequency of the clicks can increase very quickly. At the same time, usually, the intensity of the clicks decreases. By offline analysis of the acoustic data of KM3NeT-ORCA during the runs in which a high number of clicks have been identified by the automatic program, I noticed that very few clicks have ICI values lower than about $0.4\,s$. This is probably due to the fact that the hydrophones are located at a great depth with respect to the position of the sperm whales and, therefore, only the most intense clicks are detected. I also noticed that there are time periods in which there is an intense background noise that presents multiple peaks at similar frequencies compared to the sperm whale clicks. Not considering all the signals that have an ICI less than $0.4\,s$, I verified that the number of these false positives vanishes, although some bioacoustic signals are probably lost. In fig. 4.28 it is possible to observe the distribution of the ICI values recorded between April 2020 and July 2021. The distribution appears regular and a median value of around $0.8\,s$ has been obtained, in agreement with the results found in the literature [58] [59]. The upper limit of $2\,s$ was set in order to avoid to calculate the ICI for two clicks belonging to distinct sequences.

As illustrated in sec. 4.2, the sperm whale click has a multipulse structure due to the reflections that occur within the spermaceti organ of the animal. As already shown, two empirical formulas have been obtained (eq. 4.1 and eq. 4.2) to reconstruct the size of the individual by studying the characteristics of the Inter Pulse Interval (IPI), defined as the time lag between consecutive pulses being reflected within the whale's head and representing the time taken for sound to travel the length of the spermaceti sac twice.

The aspect of the sperm whale click signal as a function of time strongly depends on the orientation of the animal with respect to the hydrophone [60]. For this reason, it is not always possible to observe the typical multipulse structure (fig. 4.2). We can estimate the value of the IPI following two different methods:

1. finding a group of clicks on axis (animal placed in front of the hydrophone) in which the multipulse structure is clearly recognized and manually estimate the IPI value;

2. applying an automatic program to the entire recording period of clicks, that uses a function to identify similar patterns in the signals.

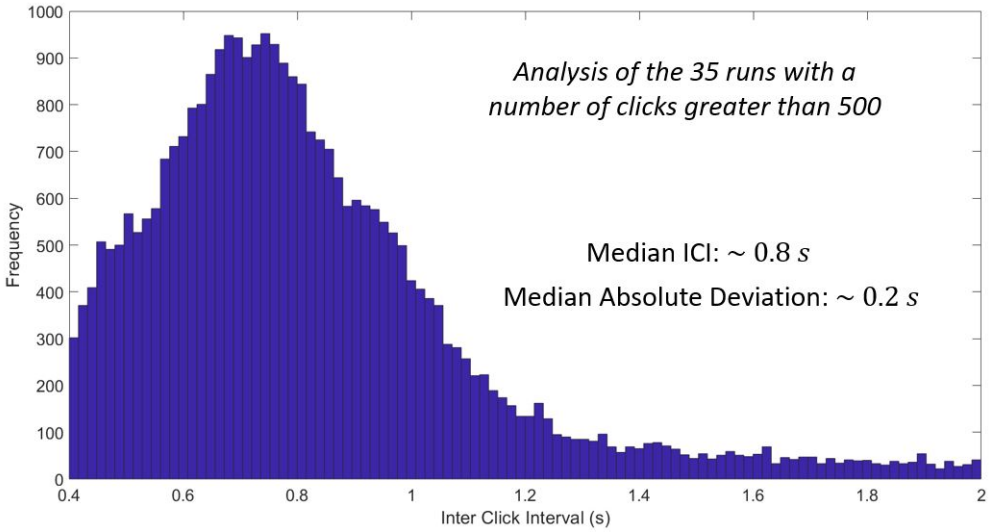

Figure 4.28: Inter Click Intervals (ICI) distribution the 35 runs with a number of clicks greater than 500 between April 2020 and July 2021.

In the second case it is possible to use the Cepstrum analysis [61]. Cepstrum is mathematically defined as follows:

$$C = \left|\left(FFT^{-1}\left(log\left|FFT\left(x\right)\right|\right)\right)\right| \tag{4.15}$$

where FFT is the Fast Fourier Transform and FFT^{-1} is the inverse Fast Fourier Transform. The Cepstrum converts the logarithm of the power spectrum into a time domain function where peaks appear at delay times equal to the time between identical or similar structures in the original time signal. In this particular case the repeating structures are the different pulses emitted by the animal and the original time signal is a time window in which the sperm whale click is contained. The Cepstrum is obtained for each click and, in order to estimate the most correct value of the IPI, the average Cepstrum is performed.

The two methods have been applied, as a preliminary test, to a KM3NeT-ORCA dataset relative to a 6 hours period full of intense sperm whale clicks (11 May 2020 between 6:00 and 12:00).

In fig. 4.29 a sequence of 8 clicks that present a multipulse structure is shown. The IPI has been extrapolated and the size of the animal has been estimated using the Rhinelander and Dawson empirical formula (2004) [44]. A mean value of $12.62\,m$ has been found, probably indicating the presence of a young male.

During the whole 6 hours period 4426 sperm whale clicks have been identified. We could try to use the entire dataset in order to estimate the most realistic IPI, using the Cepstrum analysis.

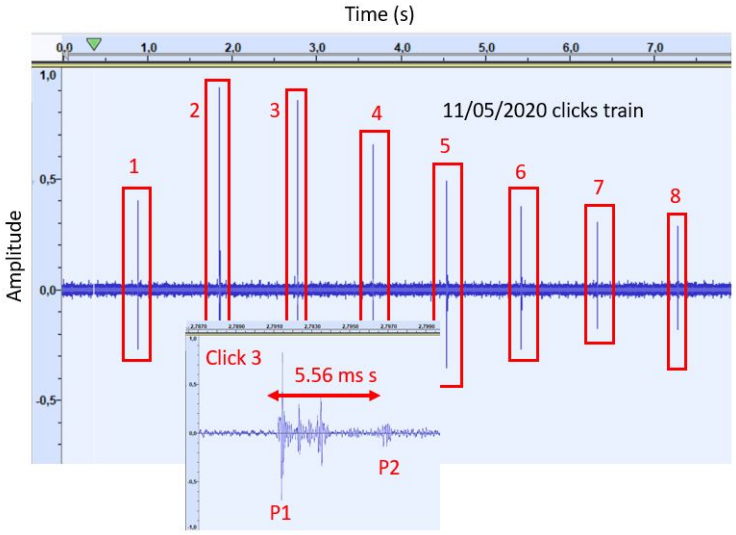

Click	IPI	Size
1	5.33 ms	12.58 m
2	5.45 ms	12.64 m
3	5.56 ms	12.71 m
4	5.42 ms	12.63 m
5	5.31 ms	12.57 m
6	5.33 ms	12.58 m
7	5.30 ms	12.57 m
8	5.45 ms	12.64 m

Mean value: $(12.62 \pm 0.04)\, m$

Figure 4.29: Amplitude versus time representation of a train of 8 clicks, which present a visible multipulse structure. The IPI for each click has been estimated and the related size of the animal has been reconstructed using the Rhinelander and Dawson formula (2004) [44] for large animals ($IPI > 5\, ms$). The two peaks between P1 and P2 visible in the zoom are the result of reflections in the animal's head and their presence is due to the orientation of the sperm whale with respect to the hydrophones.

In fig. 4.30 the Cepstrum function as a function of time (ms) is shown. The peak indicates the time delay between similar patterns identified in the original signals and corresponds to the IPI. Applying the Rhinelander and Dawson formula using the value corresponding to the centre of the peak, we obtain a value of $12.59\, m$ for the sperm whale size, consistent with that found using method 1.

This study is preliminary and the procedure has not yet been applied to other time periods, but it has been shown that the estimation of the sperm whale size through the IPI analysis can be a very powerful tool to study these animals, counting their presence during the year, estimating their average size and understanding when the hydrophones are detecting the same animal.

The final objective of the clicks analysis is the reconstruction of the routes traveled by the sperm whales, using the acoustic data coming from the different hydrophones.

For this purpose I implemented a program to calculate the delay times of the arrival of the acoustic wave between all the couples of receivers whose data is saved to disk.

The click identifier program is applied to the raw acoustic files of the hy-

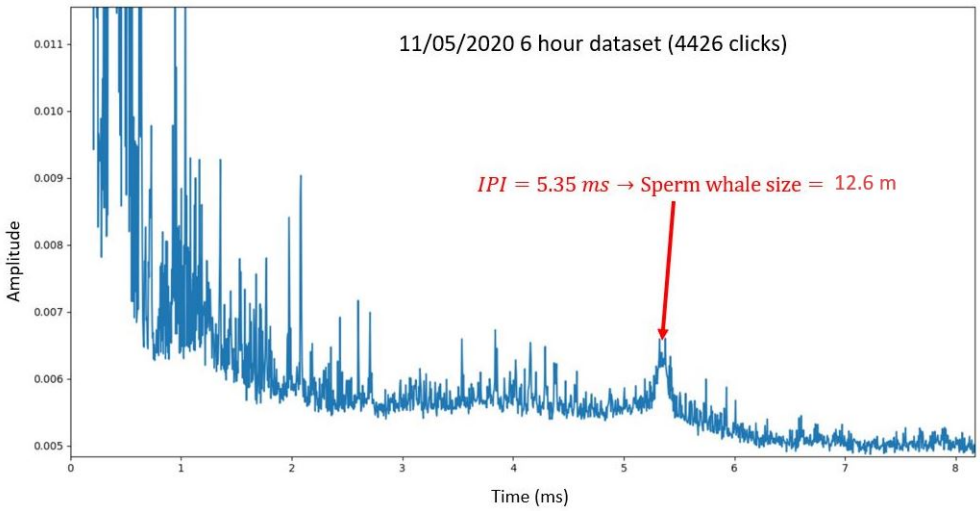

Figure 4.30: Average cepstrum representation of all the clicks detected on 11/05/2020. The peaks at the left represent minor reflections and noise patterns. The peak highlighted in red corresponds to the mean value of the IPI (in ms).

drophone with the best SNR (Signal to Noise Ratio), in order to identify the time windows (duration of 0.15 s) in which a sperm whale click is present.

At this point, for each time window in which a click has been identified, the cross-correlation function between the signal in that window and the signal of the corresponding time windows of all the other receivers is calculated.

The delay times are reconstructed as described by eq. 4.13 in sec. 4.3.3. They are saved in a text file and used as input by another program, which reconstructs the position of the source using the algorithm described in sec. 4.3.2.

As shown in fig. 4.31, during days 29/06/2020 and 07/09/2020 a good number of sperm whale clicks has been identified. In fact, in the corresponding 10 minute runs, 344 sperm whale clicks on 29/06/2020 and 162 sperm whale clicks on 07/09/2020 have been detected. During day 07/09/2020 only the data of one of the two active hydrophones was saved to disk.

In fig. 4.32 it is possible to see a click of a sperm whale detected on 07/09/2020 by all the sensors for which the acoustic data was saved. The delay times calculated with the program I implemented correspond to those deductible from this plot.

In fig. 4.33 the delay times between one of the hydrophones (DU9 hydrophone) and the other receivers are shown as a function of time (07/09/2020 data). Piezoelectric sensors are less sensitive with respect to the hydrophones, so only the most intense clicks are visible in the piezo signal. The coherence between the delay times of the different receivers over time confirms the reliability of the click identifier output.

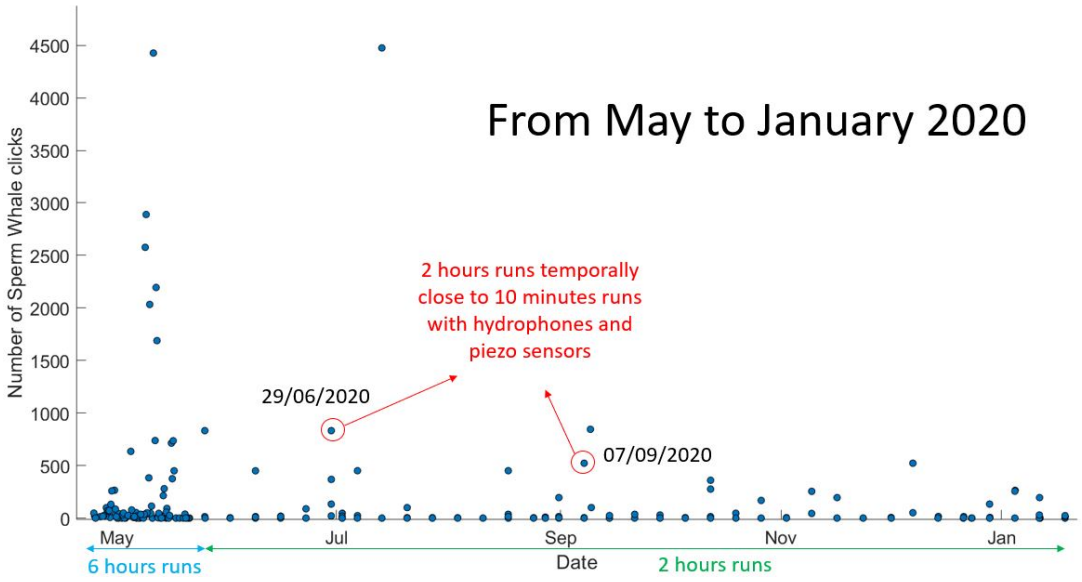

Figure 4.31: Number of sperm whale clicks detected from May to January 2020. Temporally close to the two 2 hors runs circled in red there are two 10 minutes runs with the signal of all the available hydrophones and a set of piezo sensors.

The reconstruction of the position does not give excellent results because we know the coordinates of the receivers just with the deployment accuracy of $1\,m$. The acoustic positioning system, in fact, was not active because in that period there were only two working acoustic beacons due to battery problems.

In fig. 4.34 the reconstructed coordinates of the acoustic sources recorded during 07/09/2020 are shown. The positions were extrapolated assuming the locations of the receivers calculated on 19/03/2020, a period in which all the three autonomous beacons were still active and in which the sea current measured in the area was similar to that of 07/09/2020. Observing the spatial distribution of the points, we can hypothesize the presence of 4 animals. However, the small number of points and the error certainly greater than $10\,cm$ on the position of the receivers make this reconstruction not entirely reliable.

4.3.5 Conclusions

A click identification program has been implemented, that distinguishes the signals emitted by the dolphins and by the sperm whales on the basis of the different frequency range and the typical Inter Click Interval values. The program has been successfully tested on KM3NeT real acoustic data proving its reliability.

In order to evaluate the uncertainty of the animal position, I developed a simulation program for various configurations of hydrophones and piezo sensors. The

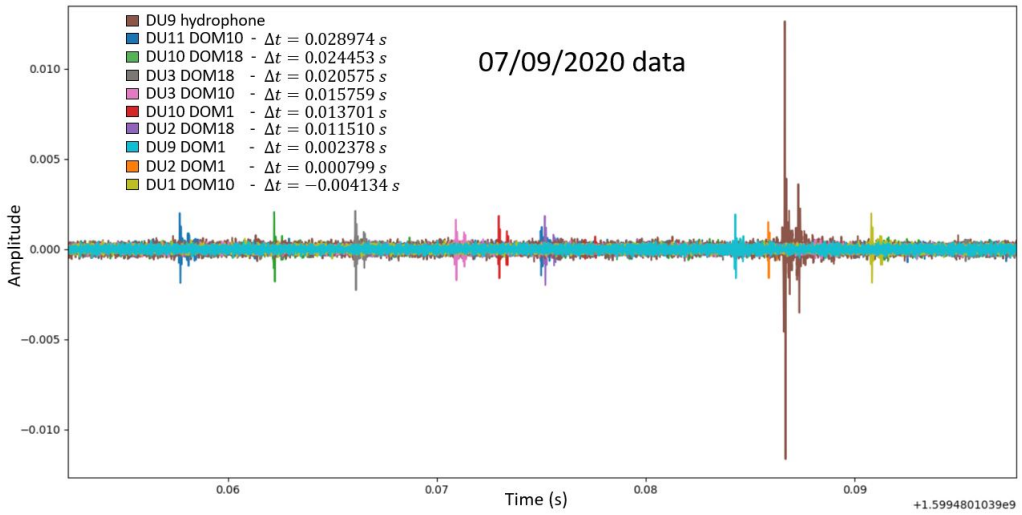

Figure 4.32: Sperm whale click detected by all the active sensors on 07/09/2020. The delay times have been calculated with an automatic program and compared with the values inferable from the plot.

program was checked in the reconstruction of the boat track during the 09/09/2020 sea campaign (three active hydrophones deployed) with encouraging results.

A statistical study has been carried out on the presence of dolphins and sperm whales in the area of the Gulf of Lion, a territory of particular interest from a biological point of view. Possible differences between nighttime and daytime hours with regard to click emission by marine mammals have been investigated. The average Inter Click Interval of the sound emissions of sperm whales has been estimated and is in agreement with previous studies.

The KM3NeT-ORCA acoustic system, at the end of Summer 2021, is composed of 3 operating hydrophones placed on the seabed and numerous piezoelectric sensors placed on the glass spheres of the DOMs. The sensitivity of piezoelectric sensors to sperm whale click frequencies is lower than that of the hydrophones. For this reason, only few very intense clicks are detected by the whole sensors and it was not always possible to use the information of the piezoelectrics to reconstruct the position of the acoustic sources.

Furthermore, the KM3NeT-ORCA acoustic positioning system is not yet online and has not yet reached the 10 cm accuracy required to achieve the best results for the reconstruction. As seen in sec. 4.3.2, the minimum theoretical number of hydrophones needed to obtain a result is 4. However, in order to have an optimal accuracy in determining the trajectory, it is necessary to have about 16 hydrophones positioned on the sea bed.

In the short future, many more strings will be deployed, each having a hy-

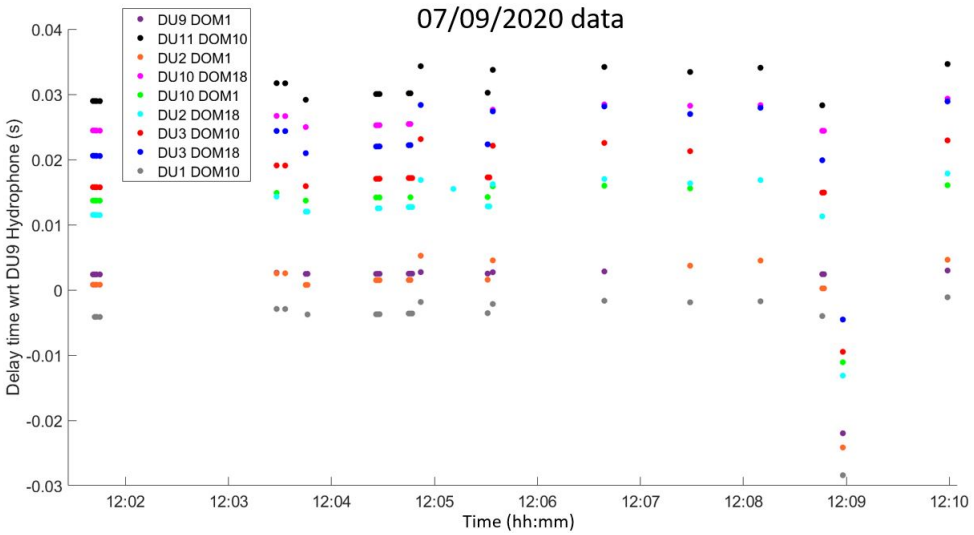

Figure 4.33: Delay times between one of the hydrophones (DU9 hydrophone) and the other receivers (piezo sensors) as a function of time (07/09/2020).

drophone on the base. The foundations were therefore laid to obtain a reliable system to reconstruct the routes of cetaceans in the area of the Gulf of Lion.

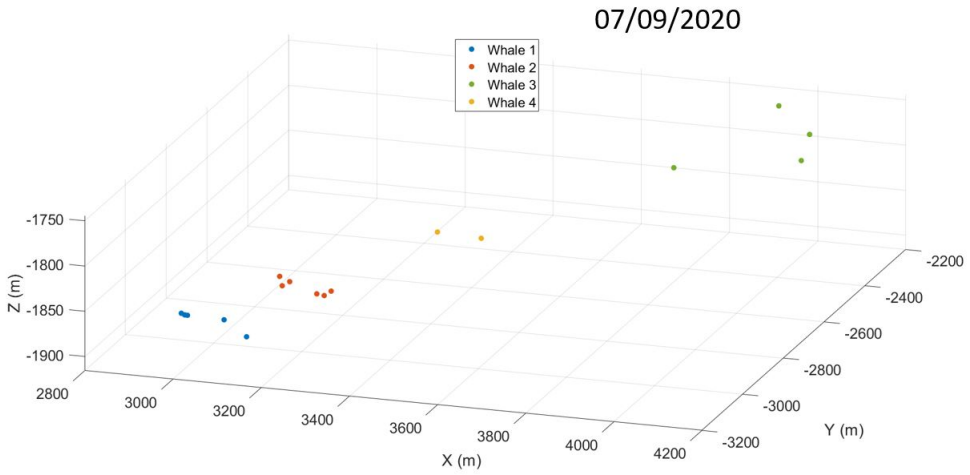

Figure 4.34: Reconstructed positions of acoustic sources recorded on 07/09/2020 10 minutes run. Observing the distribution of the points in the 3D space, we can hypothesize the presence of four distinct animals.

Chapter 5

Appendices

5.1 Cetaceans tracking - WhaleSafe project

5.1.1 Introduction

During the first year of PhD I had the opportunity to analyze the acoustic data of the Whalesafe experiment, a Natura 2000 - LIFE European project aimed at the protection and monitoring of sperm whales in the Ligurian Sea, Italy [62]. The experience I obtained from the study of these data was fundamental for the realization of the KM3NeT click identification system (see sec. 4.3.1) and the implementation of the tracking algorithms with KM3NeT hydrophones (see sec. 4.3.2).

The Whalesafe project was born with the aim of creating a real-time alert system that detects the presence of sperm whales in the Ligurian Sea, 5.3 km off the coast of Bergeggi, Italy, an area where the passage of commercial and tourist ships is considerable.

These cetaceans, in fact, are threatened by the presence of large ships that create a strong noise pollution and risk colliding with the animals.

As we will see in sec. 5.1.2, the system consists of two buoys. The first supports the data acquisition system and the antenna for the transmission of data to the ground. The second supports a system of 4 hydrophones positioned according to a specific geometry and lowered to a depth of around 70 m.

In this section I will describe the analysis of the Whalesafe acoustic data collected during June and July 2018. In particular two days, 12 and 13 July, were identified, in which numerous signals of sperm whales were detected. I developed an offline analysis program that is able to calculate the 3D position and the speed of the animals as a function of time using the information of the arrival angle of the direct acoustic wave and the arrival angle of the wave reflected on the sea surface.

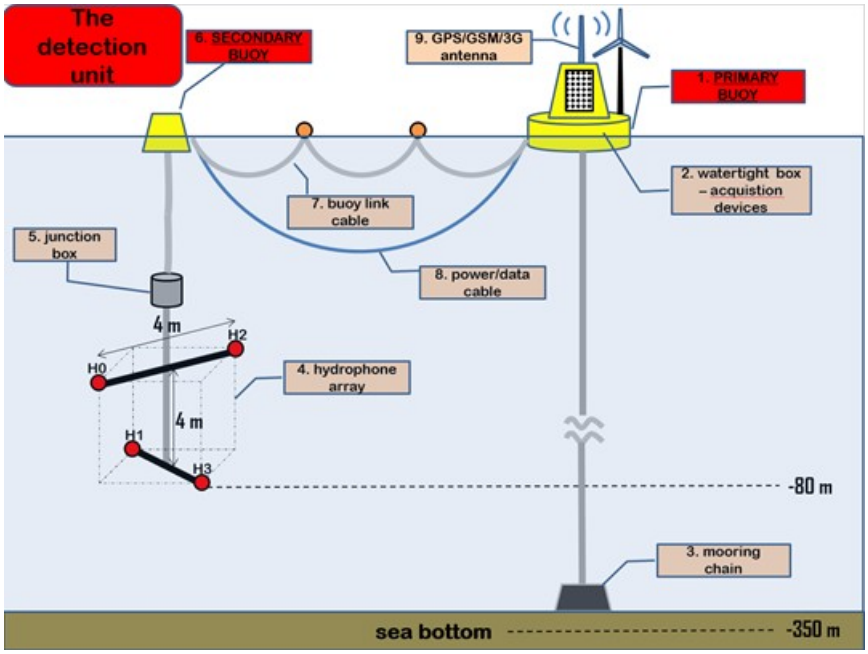

Figure 5.1: Whalesafe system design.

5.1.2 Whalesafe system design and geometry

The Whalesafe system is positioned at a distance of 5.3 km from the Ligurian coast and consists of a primary buoy, anchored to the seabed by a 1500 kg ballast, connected to a secondary buoy by means of a cable for the transmission of the signal and a system of small floating buoys, at a distance of about 50 m (see fig.).

The secondary buoy, supported by a 30 kg ballast, houses a system of 4 hydrophones, lowered to a depth of $\sim$ 70m. The hydrophones are located at the vertices of a parallelepiped with a height of 4 m. Two are placed at a distance of 4 m from each other along the diagonal of the upper face. The others, spaced like the first two, are located on opposite vertices of the lower face of the parallelepiped, forming a tetrahedron. This geometry, as we will see, is ideal for the correct reconstruction of the arrival angle of an acoustic wave.

The primary buoy contains a NI9081 cRIO controller with I/O modules that takes care of acquiring analog signals, converting them into digital signals and sending the data stream to a remote PC where the information can be viewed and saved on disk in real time. A GPS/GSM/3G antenna is also connected to the primary buoy for the location and quick transmission of the signal.

Above the hydrophones there is a Junction Box, which contains an amplifier, an analog/digital converter, 8 ethernet slots, a tilt/compass device with an accuracy of 0.1 ° and a digital thermo-hygrometer.

WhaleSafe uses GP0280M hydrophones, produced by co.l.mar (Colmar web site). They are omnidirectional hydrophones with a sensitivity of $-169\,dB\,re\,1V/\mu Pa$, optimal for a depth up to $1000\,m$.

5.1.3 Reconstruction algorithms

In order to reconstruct the position of the acoustic source with a system of 4 hydrophones placed in a tetrahedron, it is necessary to know the arrival direction of the acoustic wave that directly reaches the hydrophones and the direction of arrival of the wave reflected from the sea surface. The first objective, therefore, is to estimate the arrival direction of a generic sound wave.

As we have seen in sec. 1.2, it is possible to approximately consider the acoustic waves as plane waves, since the distance at which we want to observe the animals is significantly greater than the wavelength.

Furthermore, it is necessary to consider the acoustic source at infinite distance from the receiver, a valid approximation if the distance is much greater than the size of the detection system.

In fig. 5.2 a simplified model with only two hydrophones is shown, useful to understand how to derive the arrival direction of an acoustic wave.

In plane wave approximation, the direction of the acoustic wave is the same for the two hydrophones:

$$\cos\varphi = \frac{\vec{u}\cdot\vec{r}_{ij}}{|\vec{u}|\cdot|\vec{r}_{ij}|} = \frac{\vec{u}\cdot\vec{r}_{ij}}{|r_{ij}|} \tag{5.1}$$

From geometric considerations we get:

$$\cos\varphi = \sin\theta = \frac{ct_{ij}}{|\vec{r}_{ij}|} \tag{5.2}$$

Combining eq. 5.1 and eq. 5.2 we obtain:

$$\vec{u}\cdot\vec{r}_{ij} = ct_{ij} \tag{5.3}$$

Generalizing for a system of 4 hydrophones we obtain:

$$\begin{bmatrix} (x_2-x_1) & (y_2-y_1) & (z_2-z_1) \\ (x_3-x_1) & (y_3-y_1) & (z_3-z_1) \\ (x_4-x_1) & (y_4-y_1) & (z_4-z_1) \end{bmatrix} \begin{bmatrix} u \\ v \\ w \end{bmatrix} = \begin{bmatrix} ct_{12} \\ ct_{13} \\ ct_{14} \end{bmatrix} \tag{5.4}$$

where $x_{1,2,3,4}$,, $y_{1,2,3,4}$, and $z_{1,2,3,4}$ are the coordinates of the 4 hydrophones, c is the speed of sound and t_{ij} is the delay time between the arrival of the sound wave sound wave to hydrophone i and hydrophone j.

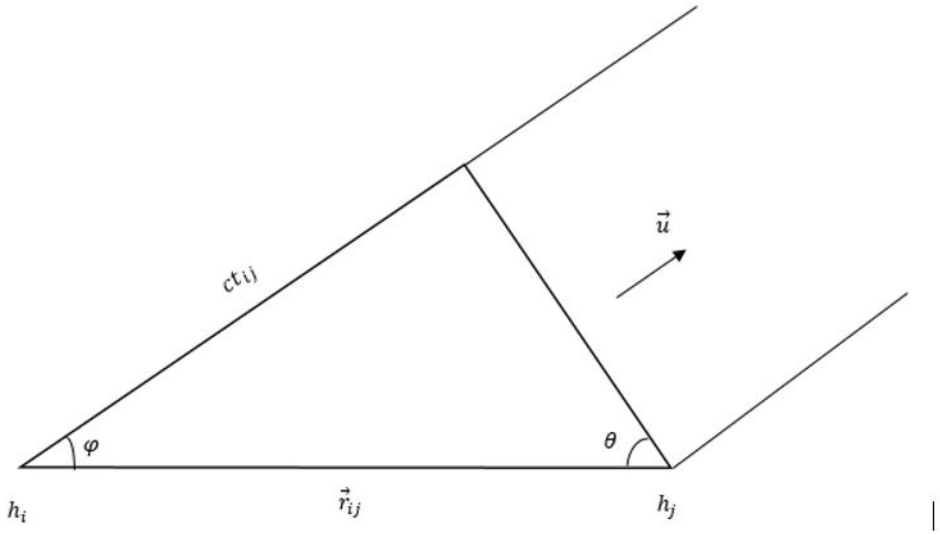

Figure 5.2: Simplified model (with just two hydrophones) to determine the direction of a sound source of plane waves at infinite distance from the receivers. h_i and h_j represent the two hydrophones; $\vec{r}_{ij}$ is a vector that represents the distance between the two receivers; c is the speed of sound, assumed constant; t_{ij} is the delay time between the arrivals of the sound wave at the two hydrophones; $\vec{u}$ is the arrival direction of the acoustic wave.

$\begin{bmatrix} u \\ v \\ w \end{bmatrix} = \begin{bmatrix} \sin\theta\cos\varphi \\ \sin\theta\sin\varphi \\ \cos\theta \end{bmatrix}$ is the versor that indicates the arrival direction of the generic sound wave.

In this way we obtained the arrival direction of the sound and the angles θ and φ (zenith and azimuth), but we still have to find the distance between the acoustic source and the system of hydrophones.

In fig. 5.3 it is possible to see the geometrical scheme of the system.

There are two different methods to reconstruct the distance between the acoustic source and the hydrophones:

1. We can use the four measured angles, zenithal and azimuthal direct and reflected angles (θ_D, θ_R, φ_D, φ_R). The program saves in a file the direct and reflected θ and φ angles for the signals recognized as sperm whale clicks only if both direct and reflected wave are detected. Direct θ_D and φ_D angles and reflected θ_R and φ_R angles define two directions in the 3D space. If $\varphi_D = \varphi_R$ were equal, as expected theoretically, the two lines would intersect in one point, the position of the source. However, direct and reflected φ are not exactly equal, due to the measurement uncertainties, and the two lines

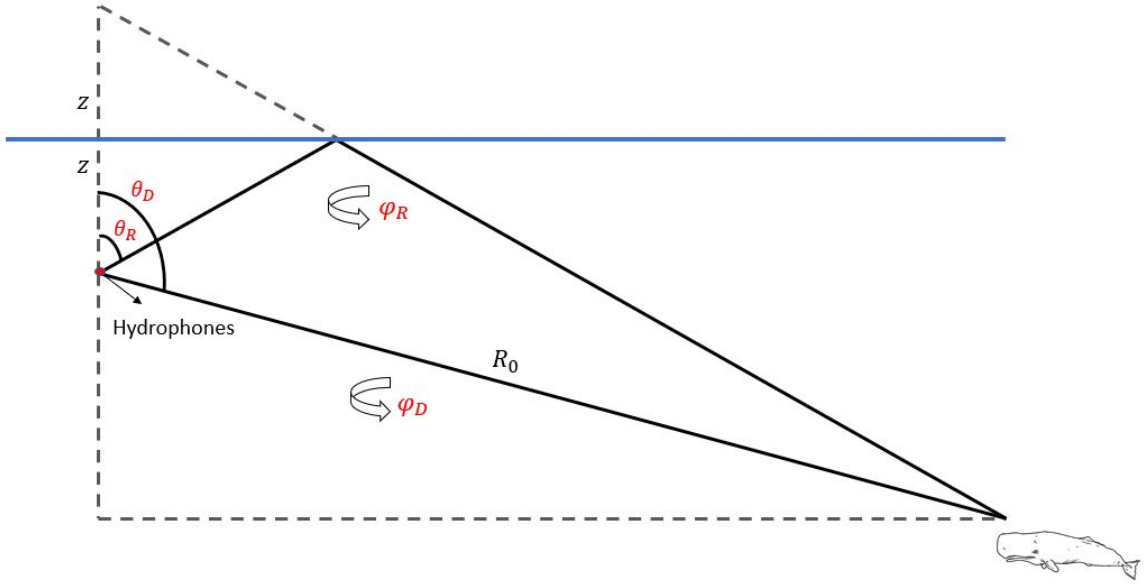

Figure 5.3: Whalesafe system geometry. (θ_D and φ_D are the zenithal and azimuthal direct angles; θ_R and φ_R are the zenithal and azimuthal reflected angles; z is the depth of the hydrophone system ($\sim 70\,m$) and R_0 is the distance between the hydrophones and the acoustic source.

do not intersect. In order to solve this issue we can calculate the segment of minimum distance between the two lines and then we can choose the midpoint of this segment as an estimate of the sperm whale position.

2. We can use the arrival angle of the direct wave (θ_D) and the delay time between the arrival of the direct wave and the arrival of the reflected wave at one reference hydrophone (Δt), neglecting the fact that the measured φ angles are not equal:

$$R_0 = \frac{4z^2 - c^2\Delta t^2}{2c\Delta t - 4z\cos\theta_D} \tag{5.5}$$

As we have seen in sec. 1.4, the sound velocity depends on pressure, temperature and salinity. The thermocline layer (below which the speed of sound depends only on the pressure) in the Mediterranean sea is at around $\sim 70\,m$ and this is the reason why the hydrophones are deployed at that depth. However, in order to reconstruct the distance between the whale and the hydrophones we have to use the information from the acoustic wave reflected by the sea surface which crosses the thermocline layer twice. For this reason it was necessary to carry out a simulation

(see sec. 5.1.4) to verify which parameters are less dependent on the passage of the acoustic wave in the thermocline layer.

5.1.4 Position reconstruction simulations

In order to estimate the dependance of the reflected angles and the delay time between direct and reflected wave on the passage in the thermocline layer, I performed a simulation in which the sea was divided into $1\,m$ layers from the sea surface to $2000\,m$.

The oscillation of hydrophones due to marine wave motion has been considered. In physical oceanography the significant wave height is defined as the mean wave height of the highest third of the waves. In this simulation a $50\,cm$ significant wave height was considered.

Observing ARPAL public data (ARPAL web site) a $4.5\,s$ average period for waves of significant height between 40 and $60\,cm$ was identified.

The position of the hydrophones is known and the position of the sperm whale can be fixed. In this case a depth of $700\,m$ and a horizontal distance with respect to the buoy of $1075\,m$ were chosen.

In the simulation 600 measurements of sperm whale click emissions have been generated (time window of $60\,s$ - one click every $0.1\,s$). I roughly considered that the whale remained stationary during this period of time. Using Snell's law and a July (month in which the dependence on salinity and temperature is usually very accentuated) Summer sound velocity profile recorded in western Ligurian Sea in 2014, the arrival angle of the direct wave, the arrival angle of the reflected wave and the delay time between direct and reflected wave have been evaluated (first step). A measurement error of $1\,\mu s$ has been considered for the delay times and a measurement error of $0.1°$ has been considered for the arrival angles.

At this point, another simulation was performed, in which for each of the 600 measurements of the arrival angle of the direct wave, the arrival angles of the reflected wave and the delay times that would be measured for a source of variable depth between $70\,m$ and $2000\,m$ have been calculated considering a Summer sound velocity profile and a constant sound speed (second step).

The depth of the source, for each simulated measurement of direct angle, was reconstructed using four different methods:

- Depth calculated with the constant velocity profile that corresponds to the measured delay time simulated in the first step;
- Depth calculated with the constant velocity profile that corresponds to the measured angle of reflected wave simulated in the first step;

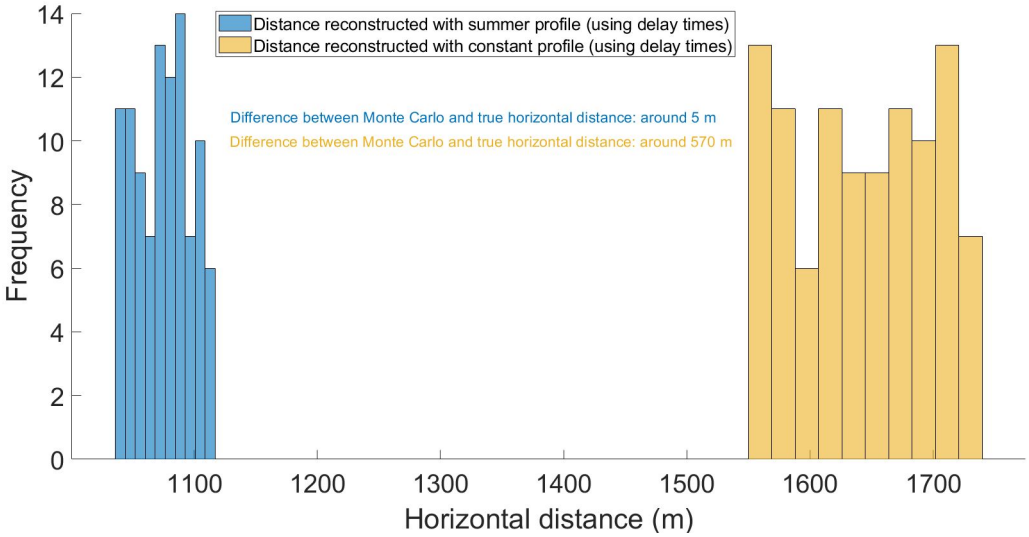

Figure 5.4: Distribution of distances (600 measurements) reconstructed with a Summer profile (blue) and with constant sound speed (yellow), in both cases extrapolated from the delay time. The source is located at a depth of 700 m and at a distance from the buoy of 1075 m horizontally.

- Depth calculated with the Summer velocity profile that corresponds to the measured delay time simulated in the first step;
- Depth calculated with the Summer velocity profile that corresponds to the measured angle of reflected wave simulated in the first step.

Merging the information of the reconstructed depth and the measurement of the direct angle we can evaluate for each of the 600 simulated clicks the horizontal distance between the system of hydrophones and the acoustic source.

In fig. 5.4 and fig. 5.5 we can see respectively the distributions of the reconstructed horizontal distance for a fixed position of the whale using the delay times and the reflected angles.

We can notice that the angles of the reflected wave affect slightly the calculation of the position of the animal. On the other hand the delay times strongly affect the reconstruction. Therefore, the right variables to use, if we want to ignore the sound velocity profile, are the arrival angles of the reflected wave, θ_R and φ_R (method 1 in sec. 5.1.3).

5.1.5 Whalesafe data analysis

The Whalesafe system was operational during the Summer of 2018, especially in the months of June and July. In particular, numerous sperm whale clicks were

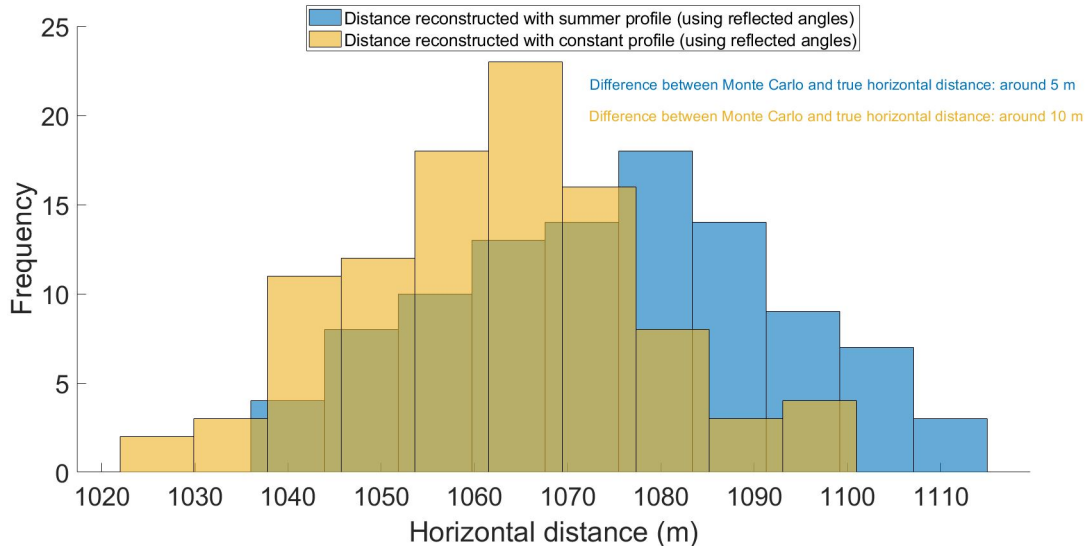

Figure 5.5: Distribution of distances (600 measurements) reconstructed with a Summer profile (blue) and with constant sound speed (yellow), in both cases extrapolated from the reflected angle. The source is located at a depth of 700 m and at a distance from the buoy of 1075 m horizontally.

detected by the hydrophones on 12 and 13 July 2018. For this reason, a sighting campaign was conducted on 13 July 2018 in order to spot the animals during emersions and subsequent immersions. The comparison between the reconstructed tracks and the sighting locations has been useful to calibrate the system.

In fig. 5.6 an example of a sperm whale click detected by all the four hydrophones is shown. The figure shows very well how it is possible to calculate the delay times of the sound wave arrival at different hydrophones.

A total of 1308 sperm whale clicks were analysed. The program that processes the raw acoustic data identifies the sperm whale clicks and saves the arrival angles of the direct and reflected acoustic waves and the delay time between the two [62]. As shown in fig. 5.3, if the arrival angle is larger than 90° it means that the sound comes from below the hydrophones level and, therefore, we are receiving the direct wave. On the contrary, if the arrival angle is below 90°, the sound comes from above and we are detecting the wave that is reflected on the sea surface.

The position of the sperm whale is reconstructed point by point using method 1 described in sec. 5.1.3, which uses the measurements of the four angles: direct and reflected θ and φ.

The acoustic data selected by the program must be filtered to reject noise contributions. The following three conditions were chosen:

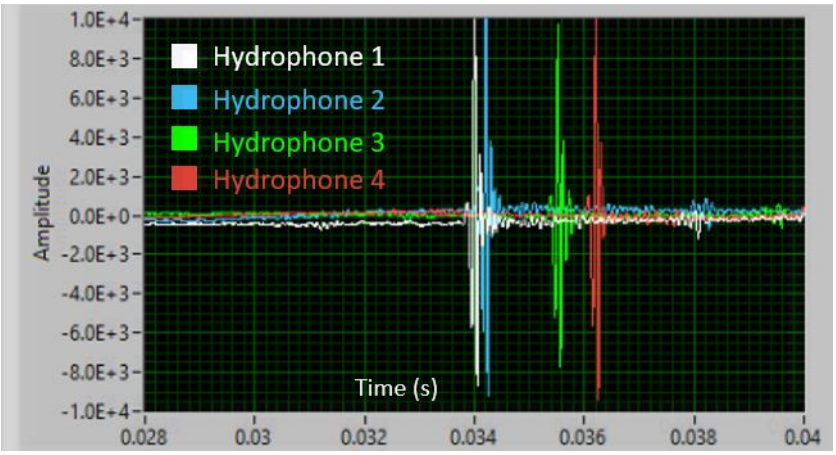

Figure 5.6: Amplitude vs time plot of a sperm whale click recorded by four Whale-safe hydrophones.

$$\theta_D + \theta_R < 180^\circ \tag{5.6}$$

$$\theta_D > 90^\circ \tag{5.7}$$

$$|\varphi_D - \varphi_R| < 2^\circ \tag{5.8}$$

Looking at fig. 5.3 we can clearly see the geometric reasons why the condition of eq. 5.6 must be verified. Condition of eq. 5.7 is useful to select only sources that come from below the system of hydrophones. It is known, in fact, that sperm whales do not emit clicks when they are very close to the sea surface, both in descent and in ascent. Finally, the direct and reflected φ angles, in principle, should be equal, but we should take in account measurements uncertainties. Eq. 5.8 is used to exclude data for which the difference between the direct and reflected φ angles is too large, so they does not corresponds to the same source.

In fig. 5.7 we can observe all the signals measured during 12 and 13 July already filtered according to conditions 5.6, 5.7 and 5.8. The tracks of many animals can be seen observing the specular trend of the direct and reflected θ angles. Furthermore, observing the φ angles, we can confirm the simultaneous presence of two or more sperm whales in different time intervals. This would not be possible by looking only at θ angles, as the animals usually emit clicks at similar depths. In fig. 5.7 we can also see the correspondence between the sighting times and the tracks.

The source positions can be reconstructed fitting with polynomial functions the measurements over time of the four angles (see for instance fig. 5.8) and then calculating the position of the source using as input the points along the fit curves.

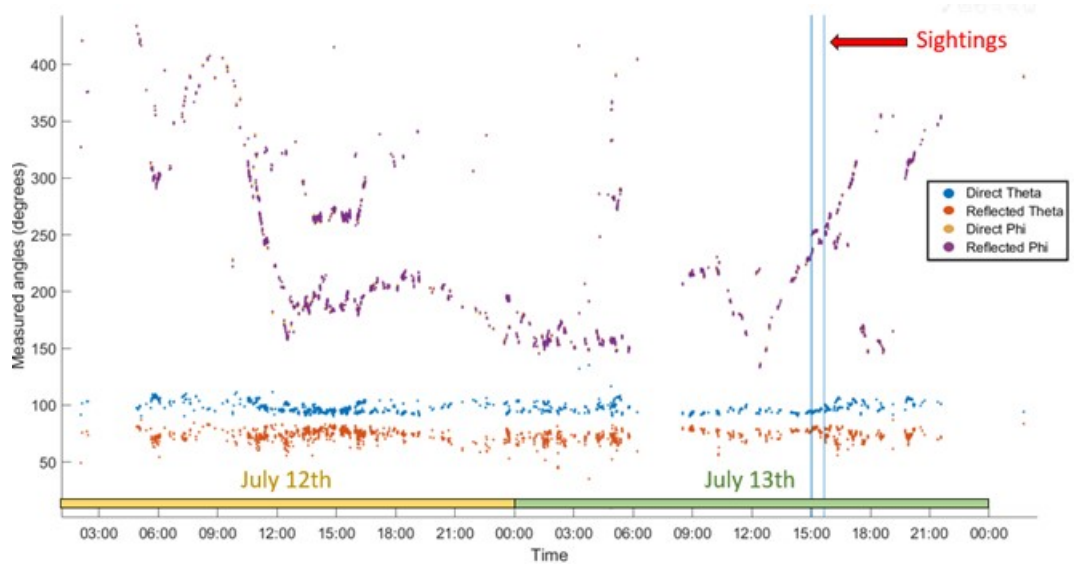

Figure 5.7: All filtered measured angles on 12 and 13 July 2018 by Whalesafe system. The blue points represent the direct θ measurements, the red ones the reflected θ measurements, the yellow ones the direct φ measurements and the violet ones the refletcted φ measurements.

Twenty remarkable time intervals were selected, in which there are enough data to reconstruct the tracks of the acoustic sources. For each of these tracks the trend of the three coordinates (x, y and z) as a function of time, the three-dimensional track of the animal and the module of the speed of the sperm whale as a function of time were calculated. In fig. 5.9 the angles measured from 13:50 to 14:10 of 12 July 2018 are shown as an example. Observing the φ angles, we can deduce that two animals have been detected in the same time.

In fig. 5.10 a three-dimensional representation of the tracks of the two sperm whales of fig. 5.9 is shown. The colours represent the module of the animal's speed. Looking at the different tracks, a relationship between whale speed and its ascendent or descendent movement was not observed.

The real data analysis allow us to verify if, as shown by the simulations, the reflected angle measurment is less affected by the error due to the sound velocity profile with respect to the delay time measurement. For this purpose the position of the sperm whales have been reconstructed using four different combinations:

1. using delay time measurements and a constant velocity profile;

2. using delay time measurements and a Summer velocity profile measured in the Ligurian Sea during July 2014;

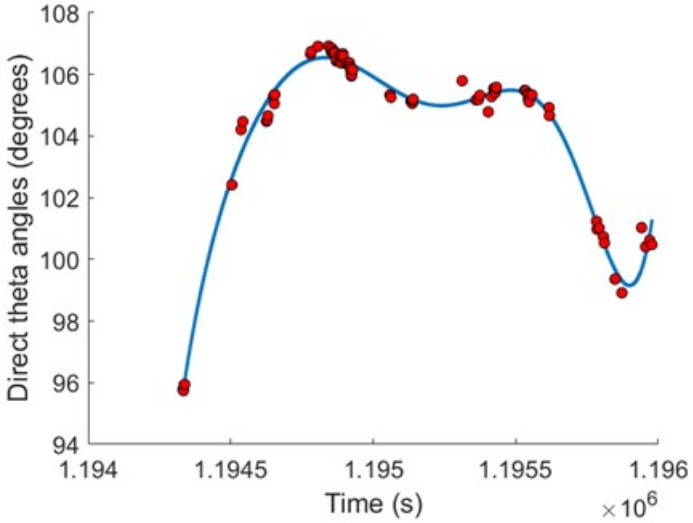

Figure 5.8: Polynomial fit of direct theta angles for a sperm whale track in the time interval from 19:40 to 20:16 of 13/07/2018.

3. using reflected angle measurements and a constant velocity profile;

4. using reflected angle measurements and a Summer velocity profile measured in the Ligurian Sea during July 2014.

In order to reconstruct the position of the acoustic source using a non-constant speed profile, a program was implemented, conceptually similar to the simulations (see second step in sec. 5.1.4), but this time the input data are the real data measured by the Whalesafe system.

In fig. 5.11 we can see the depth of one of the animals reconstructed using the delay time method (method 2 in sec. 5.1.3) using a constant velocity profile or a Summer velocity profile. We can notice how there is a consistent difference between the two cases. The depths calculated with the constant velocity profile are more spread.

In fig. 5.12, instead, we can see the depth of the same animal reconstructed using the reflected angle method (method 1 in sec. 5.1.3) using differently a constant velocity profile or a Summer velocity profile. As the simulation had shown, we can see how in this case the two reconstructions are closer each other. This result confirm that the reflected angle measurement is more reliable because less affected by the sound velocity profile variations.

Similar results can be observed by applying the same procedure to the other tracks that were identified on 12 and 13 July 2018.

All reconstructed sperm whale tracks have been represented on a bathymetric plot, as shown in fig. 5.13 (green tracks). As expected, the animals move along

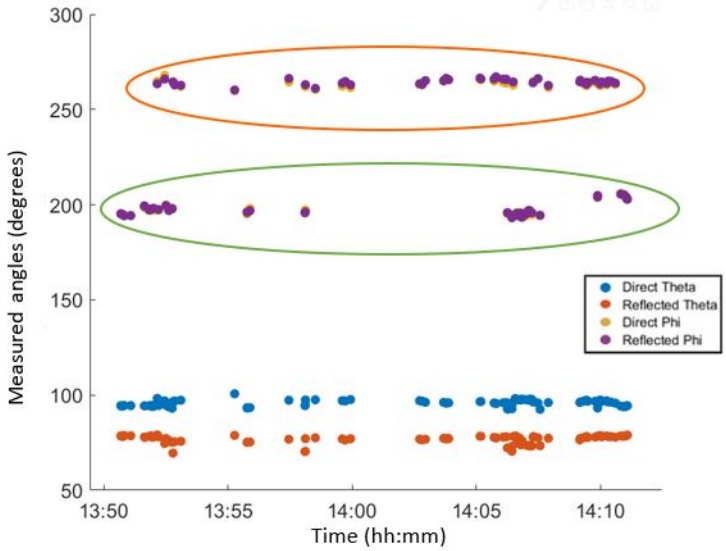

Figure 5.9: Measured angles of the sperm whale track in the time interval from 13:50 to 14:10 of 12/07/2018.

the underwater ridge, looking for food through the canyons, where it is easy to find shrimps and other animals predated by sperm whales. However, we observed an anomalous behaviour. The movement of the animals does not seem to develop along the underwater ridge. This could be due to calibration issues, it is likely that the tracks need a counterclockwise rotation. We can exploit the comparison between tracks and sightings of 13 July 2018 to confirm the assumption.

The animals were sighted between 14:40 and 16:00 on 13 July 2018. In that time interval, four different sperm whale tracks were identified, as we can see in fig. 5.14.

Track number 1 can certainly be excluded as at the time of sightings the sperm whale was at a depth of about $200\,m$. Tracks number 2, 3 and 4 could, instead, correspond to the sperm whales that have been sighted. We can consider an uncertainty of a few minutes on the sighting time and, as a precaution, we can consider a circumference of $400\,m$ radius around the sighting points, because they were guessed by eye as distance from the GPS position of the boat.

As shown in fig. 5.15, if we assume a rotation of the tracks of 38 degrees (empirically found), we can see how they approximately coincide with the sighting areas. We can guess that the sperm whale was a single individual who travelled along the track number 2, emerged at 15:01, immerged at 15:02, followed the track number 3, emerged and was sighted at 15:42, and then continued along the track number 4.

If we consequently rotate all the reconstructed tracks during 12 and 13 July

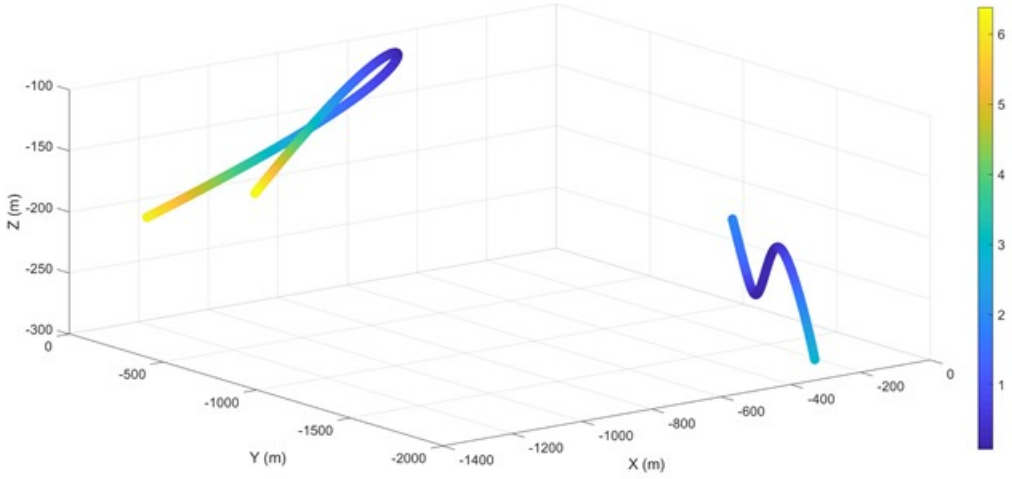

Figure 5.10: Three-dimensional tracks of the two sperm whales in the time interval from 13:50 to 14:10 of 12/07/2018. The colours represent the speed of the animals.

2018, as shown in fig. 5.13, red tracks, sperm whales seem to move as expected, along the ridge of the underwater mountain. It can also be deduced that the animals, while emitting clicks in search of food in this area, move to an average depth ranging from 200 to 600 m below the sea surface level. Moreover, the tracks were detected only in the valley to the west of the underwater ridge, likely indication of a larger presence of crustaceans and other small animals, typical food of sperm whales.

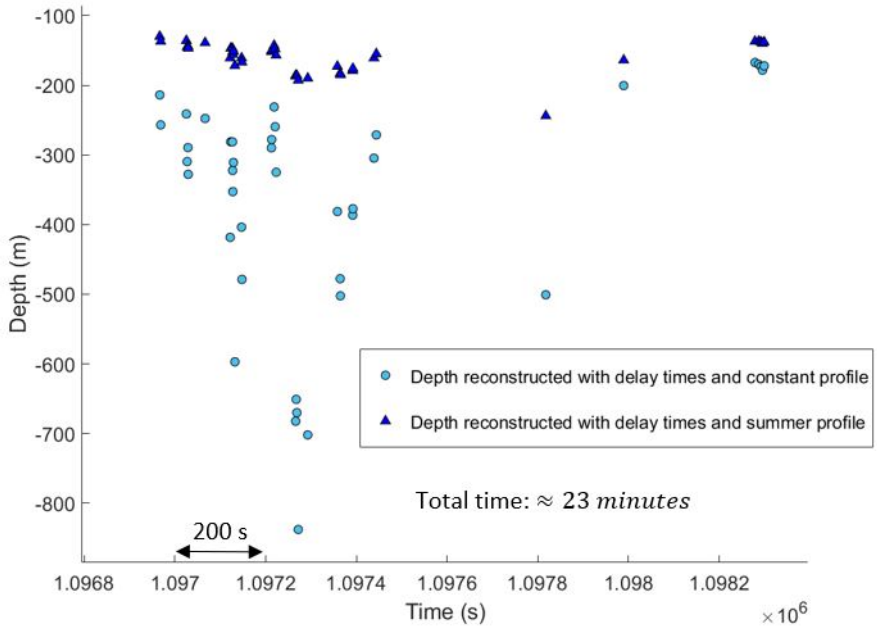

Figure 5.11: Depth reconstructed using delay times measurements with two different sound velocity profiles (constant and Summer) for the track recorded on 12 July 2018 from 16:42 to 17:05.

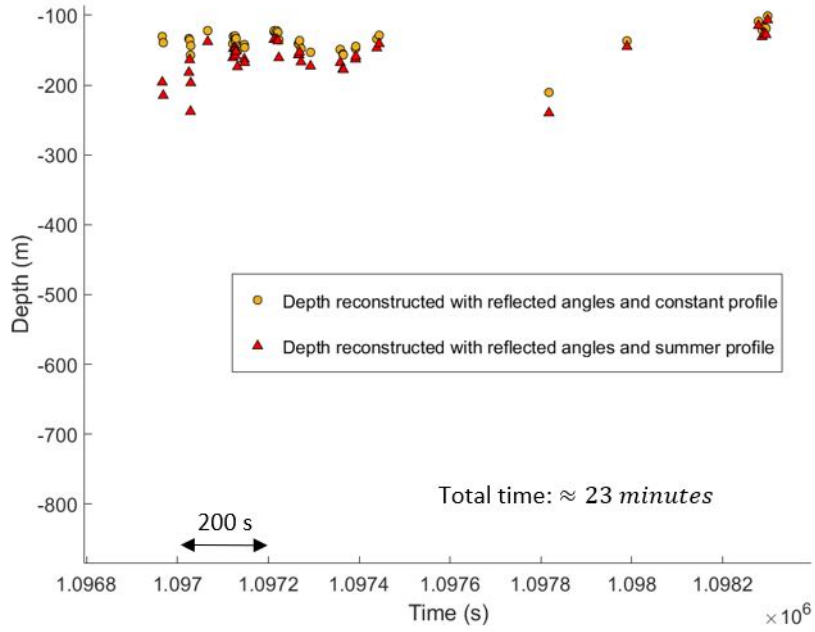

Figure 5.12: Depth reconstructed using reflected angle measurements with two different sound velocity profiles (constant and Summer) for the track recorded on 12 July 2018 from 16:42 to 17:05.

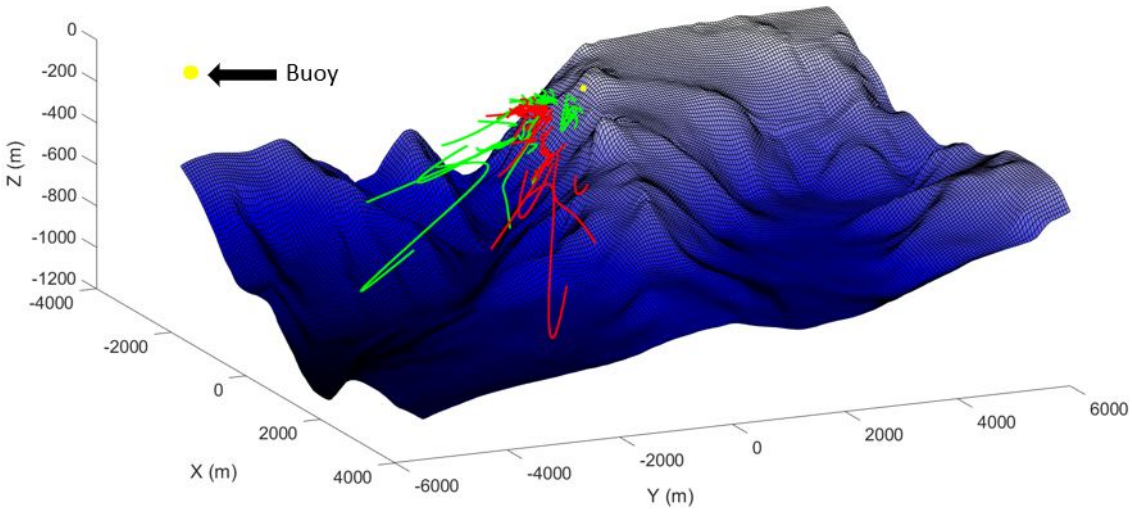

Figure 5.13: Bathymetric plot with all the sperm whale tracks reconstructed during 12 and 13 July 2018. The green tracks are not rotated. The red tracks are rotated by 38 degrees.

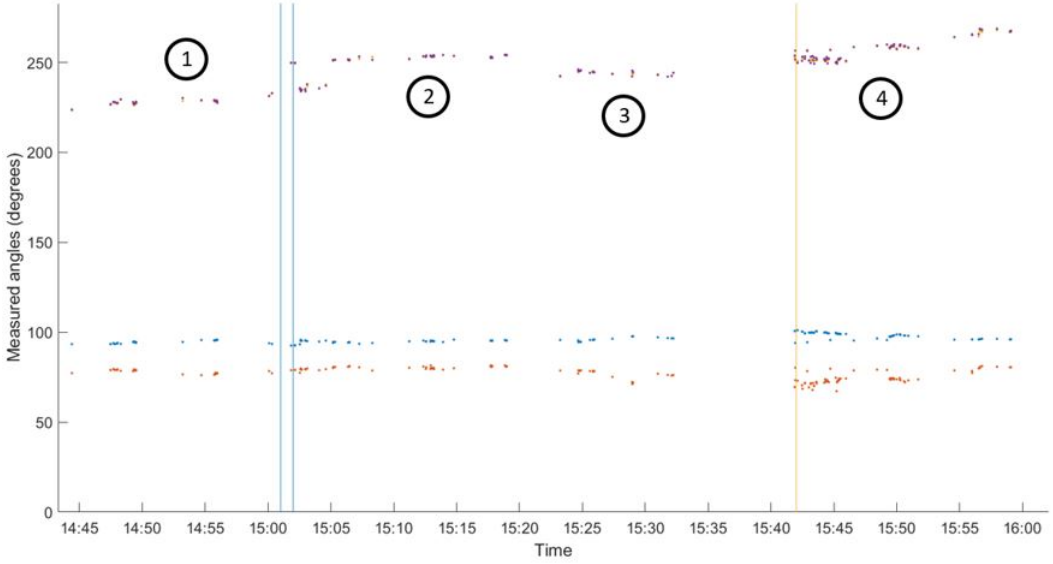

Figure 5.14: Measured angles in the time interval in which the animals were spotted (between 14:45 and 16:00 of 13 July 2018).

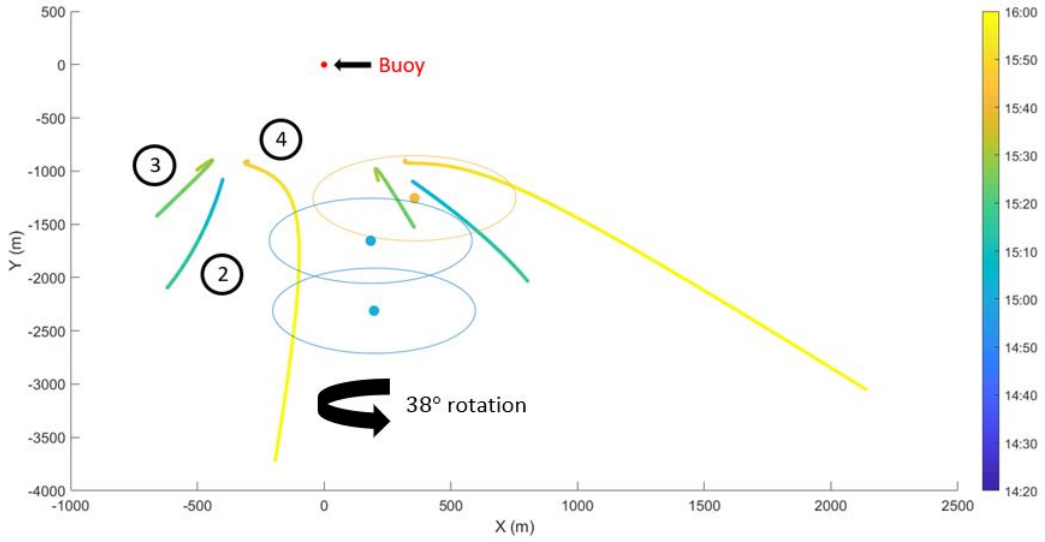

Figure 5.15: 2D plot with the sighting points and the four sperm whale tracks in the same time interval. The colours represent the time. The circles represent the uncertainty on the sighting position guess by eye.

5.1.6 Conclusions

An effective method was found to calculate the arrival direction of a sound wave using a system of four hydrophones placed on a tetrahedron.

Different methods were investigated to reconstruct the distance of the acoustic source. It is possible to use θ_D and φ_D angles and θ_R and φ_R angles or to use θ_D and φ_D angles and the delay time between the arrival of the direct wave and the arrival of the reflected wave at a reference hydrophone.

Due to the presence of a sound velocity profile, it was necessary to implement a simulation in order to understand which method is less dependent on the variations of sound speed in the surface layer above the so-called thermocline. Through these simulations it was possible to conclude that the positions reconstructed using θ_R and φ_R angles depend slightly on the sound velocity profile.

Twenty remarkable time intervals, identified during 12 and 13 July 2018, have been analysed, in which many sperm whales emissions were detected in the area. Reconstructing the tracks, using the methods described above, real data confirmed that the calculation of the position of the acoustic source using the reflected angles is more reliable.

Observing the tracks on the bathymetry it was noticed that, differently from what was expected, the animals did not move along the underwater ridge in order to search for food. So, a systematic calibration shift has been assumed.

In order to calibrate the system, therefore, the sightings of 13 July 2018 were exploited. By comparing the reconstructed tracks and the sightings in the same time interval, it was possible to correct the reconstructed tracks assuming a systematic rotation of 38 degrees. In this way the sperm whales move, coherently with what is expected, along the mountain ridge.

The area of largest occupation of sperm whales is located west of the ridge and the average depth of the routes is between 200 and 400 m.

The results of the Whalesafe project lay solid foundations for future reliable cetacean tracking systems in the Ligurian Sea.

5.2 Analysis of Genova killer whale's sounds

5.2.1 Introduction

From 01/12/2019 to 18/12/2019 four killer whales (Orcinus orca) (in the initial days even a cub) were present inside the port of Genova Pra', Italy. On 6-8-9-11/12/2019 the University of Genoa and the INFN of Genoa collected acoustic data using one hydrophone connected to a sound card and a portable PC. The catalog of sounds and a brief analysis is available at the following INFN page: Acoustic studies of the killer whale pod in Genoa

From 11:29 on 2019/12/07 to 11:12 on 2019/12/11 Tethys Research Institute collected acoustic data from a system with one fixed hydrophone (produced by NAUTA scientific) positioned on the seabed at a depth of around 10 m.

Killer whales can emit a large variety of different vocalizations (different kinds of whistles, echolocation clicks, pulsed calls, low-frequency pops and jaw claps) [63]. The acoustic signals are emitted by moving air masses between the nasal sacs in the area close to the blowhole.

These animals exploit the sound emissions for three main purposes: communication, orientation and identification of preys.

This study presents a statistical analysis of the sounds recorded by the Nauta Scientific hydrophone and the compilation of a catalog in which the acoustic emissions have been divided into three categories: simple, compound and pattern sounds.

5.2.2 Statistical analysis

1326 five minutes Acoustic Files have been saved. 217 files contain killer whale's sounds. They have been divided in four categories based on the amount of found emissions:

- Quality 1 ($1-5$ killer whale's emissions)
- Quality 2 ($6-15$ killer whale's emissions)
- Quality 3 ($16-30$ killer whale's emissions)
- Quality 4 (>30 killer whale's emissions or short but very intense conversations)

Around 16.4 % of the files contains orca's emissions.

As shown in fig. 5.16, there are three time windows in which no killer whale sounds were detected. During the night there are no sightings that can testify the presence in the port of the killer whales (as for example during the first time

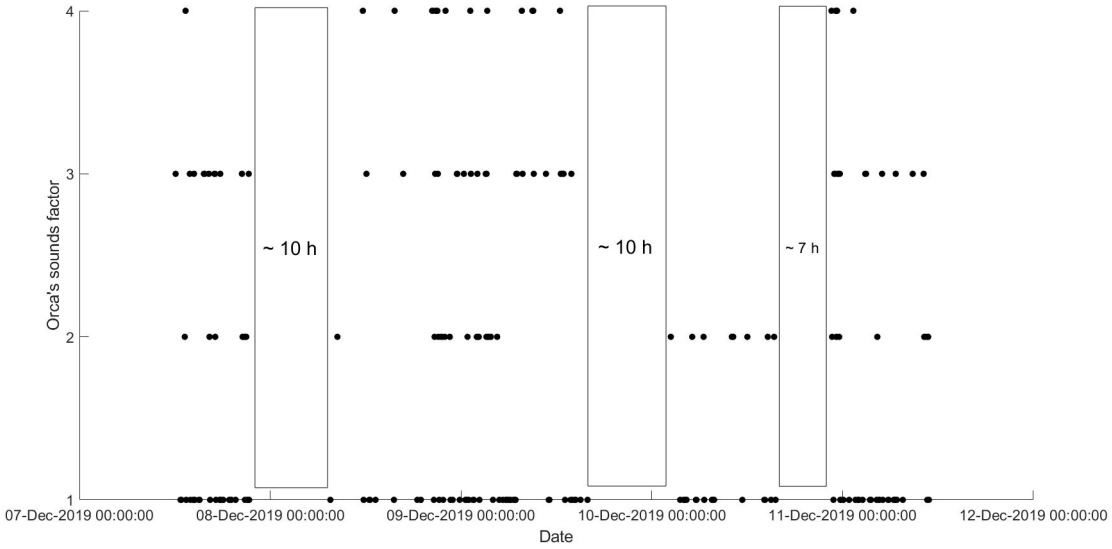

Figure 5.16: Orca's sound factor as a function of time: the rectangles indicate the periods in which there were no killer whale's emissions.

window highlighted in the plot). On the other hand, during the day sometimes they have been observed leaving the port, probably in search of food. The biologists of Genoa Whale Watching have seen the killer whales leaving the port at around 3:00 pm on December 9th and around 4:00 pm on December 10th, corresponding to the start of the second and the third time windows visible in the plot, in which no sound emissions were detected.

This is comforting and confirms the fact that there are no very long periods during which killer whales have been present in port without emitting any sound.

It is possible to estimate the average interval between two "conversations". In order to achieve this purpose, two series of sound emissions are considered separate if the time interval between them is greater than 5 minutes, the length of each file.

In fig. 5.17 the distribution of the time intervals between two "conversations" (considering only those longer than 5 minutes) is shown. Most of the breaks are less than an hour. It is likely that during these time intervals the killer whales were actually present in the port, but did not really emit any sound. During the day, in fact, they have been constantly spotted by different Whale-watching groups. Furthermore, during the last data taking by the INFN group (2019/12/11) the killer whales were visible in the harbour area for over an hour but no sound was recorded by the hydrophone, despite the spatial proximity of the animals.

Excluding the most extreme values of the distribution, which correspond to the periods in which the killer whales left the port, it is possible to calculate the median of the distribution of the intervals. A value of around 23 minutes is obtained.

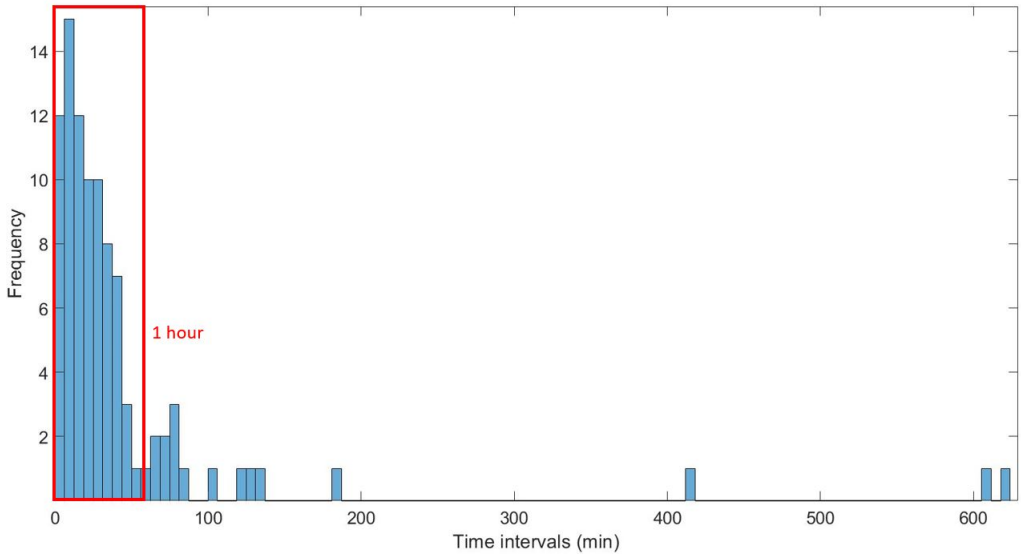

Figure 5.17: Distribution of the Time Intervals longer than 5 minutes.

5.2.3 Killer whale sounds classification

Killer whale sounds can be classified in:

- Simple sounds (distinguishable unique emission)
- Composite sounds (two or more consecutive different emissions)
- "Pattern" (recognizable pattern formed by two or more sounds separated by a certain time)

17 simple sounds, 16 composite sounds and 5 patterns have been identified and classified. In fig. 5.18, fig. 5.19 and fig. 5.20 are shown examples of simple, composite and pattern spectrograms, respectively.

All the acoustic files with a great number of killer whale emissions (in total 30 five minutes file, around 2 hours and 30 minutes of intense "conversations") have been analysed looking at the spectrogram and counting the number of the sounds of each category.

Most of the sounds that have been recorded are different types of whistles, sounds useful to these animals for communication at a short distance between individuals of the same pod [64].

During the period in which the orcas were present in the port of Genoa, only a few times they emitted clicks, useful for the orientation and location of preys. This is consistent with the fact that the presence of fish in the port area is very limited. Most likely the animals ate during the sporadic outings in the open sea.

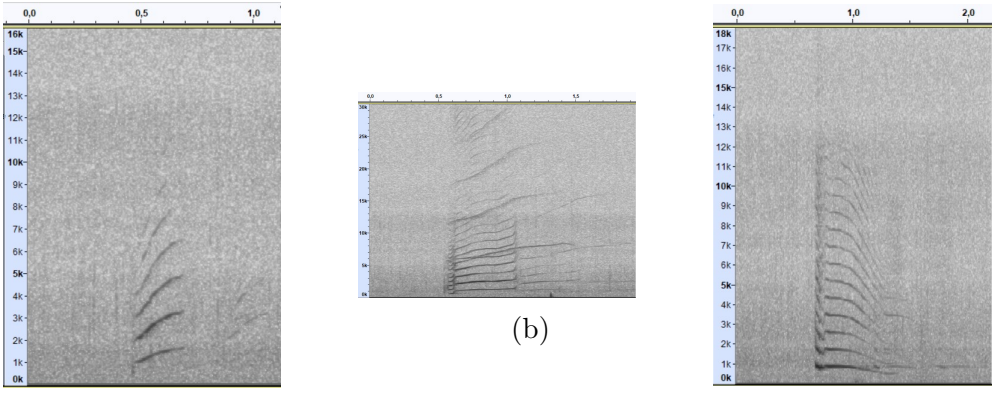

(a) (b) (c)

Figure 5.18: Examples of simple sounds spectrograms.

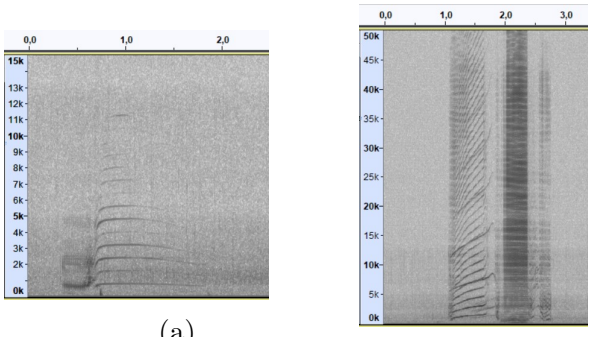

(a) (b)

Figure 5.19: Examples of compound sounds spectrograms.

In fig. 5.21 and in fig. 5.22 the distributions of the various categories of sounds that have been classified, for simple and compound sounds respectively, are shown.

Simple sounds are 60.6 % of the 1402 analyzed signals, showing a slight predominance of this type of emissions.

Furthermore, it is possible to divide the sounds into monophonic and biphonic emissions, in which two emissions of different frequency overlap simultaneously (see for example fig. 5.18b). 53.5 % of the detected sounds are monophonic emissions. This shows that the proportion between the two different types of sounds is not biased in favor of one or the other.

It is possible to notice that in both cases (very evidently for simple sounds) there are categories that are very present and others that are much rarer. This could indicate that killer whales use some acoustic emissions with a generic meaning and others with a more specific meaning.

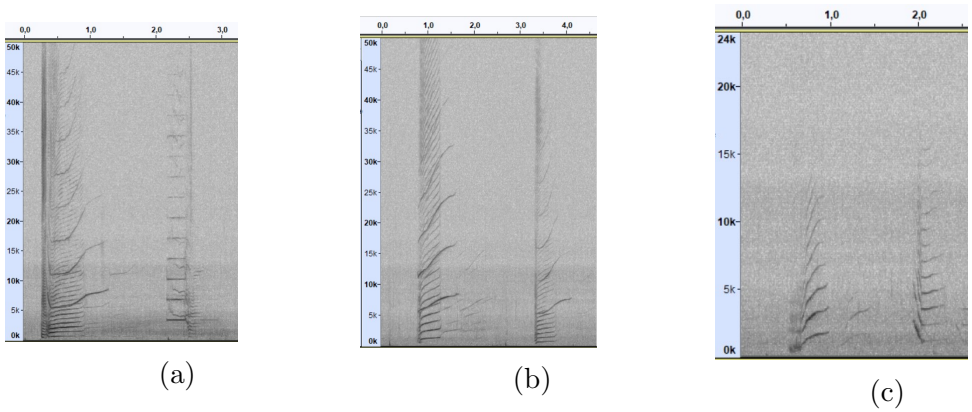

Figure 5.20: Examples of patterns spectrograms.

5.2.4 Conclusions, hypotheses and future steps

NAUTA Scientific Acoustic Data have been analyzed and divided in categories based on the ammount of killer whale sounds. The emissions have been classified looking at the spectrogram shape (frequency over time) and directly hearing the sounds.

Some sounds are more frequent, while others are rarer. Less frequent sounds may have a more specific meaning, referring to some particular situation.

The emissions have been divided in simple, compound, monophonic and biphonic categories. Repeated sound patterns have been observed. They could be complex sentences or conversations between different killer whales.

A comparison with the online catalogs of Icelandic and other origin orcas could be very important in order to verify if there are emissions typical of the different areas of the world.

Further studies are in progress to confirm, through the automatic cross correlation between the spectrograms, the reliability of the selected categories.

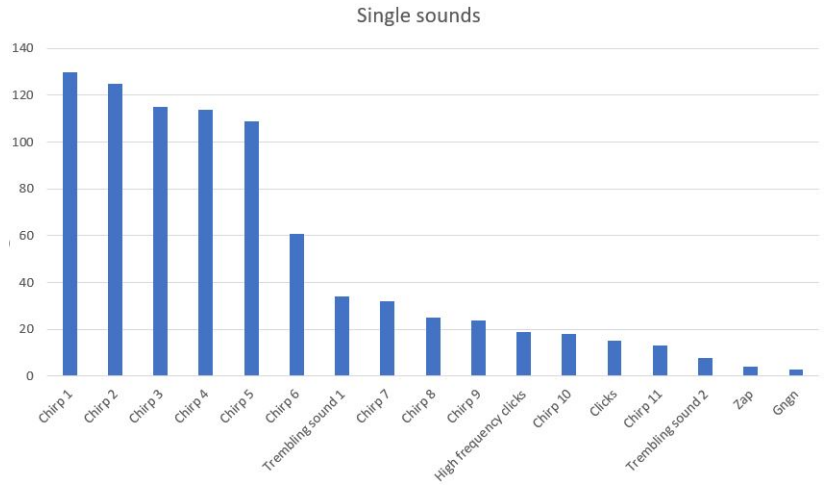

Figure 5.21: Distribution of single killer whale sounds. The sounds have been divided into different categories, some already existing in the literature (for example chirps # are different types of chirps, distinguishable by observing the trend in time and frequency in the spectrogram, and clicks are typical emissions for echolocation) and others with onomatopoeic (zap, gngn) or evocative (trembling sound) names.

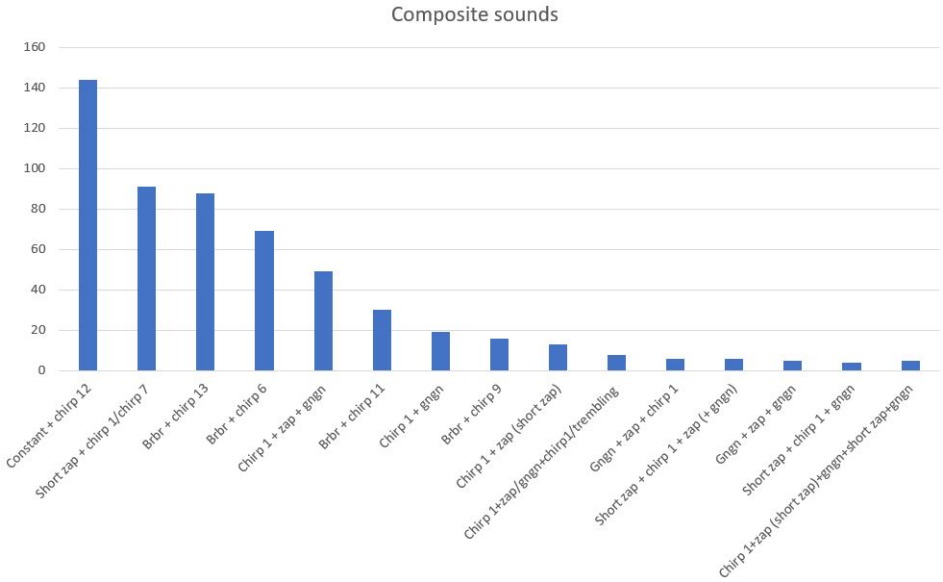

Figure 5.22: Distribution of composite killer whale sounds. Composite sound names consist of sum of different single sound names (see fig. 5.21). Some chirps are only present within composite sounds.

Conclusions

The KM3NeT infrastructure represents an important opportunity, not only for research on neutrino physics and for the identification of astrophysical neutrino sources, but also for the study of marine mammals present in the area of the Pelagos Cetacean Sanctuary, the Gulf of Lion and in the Ionian sea in front of Capo Passero. The presence of fixed hydrophones positioned at great depths allows to detect the sounds emitted by cetaceans and to study their behavior and the impact of anthropic activity on their habits.

During my PhD I demonstrated how it will be possible for KM3NeT to become one of the main reference point for estimating the presence and passage of cetaceans in the area. A preliminary work was carried out aimed at determining the position of all the acoustic elements of the system, useful both for the reconstruction of the muon tracks and for the estimation of the position of the sperm whales, using the delay times between the different hydrophones. A method has been optimized determining the position of all elements of the system with an accuracy of about $10\,cm$, sufficient for the purposes mentioned above. The method has been tested through Monte Carlo simulations and on real data.

A dolphin and sperm whale click identification program has been successfully implemented and tested on real KM3NeT-ORCA data.

Subsequently, an algorithm was developed for an efficient reconstruction of the routes of the sperm whales using the delay times between couples of hydrophones. Simulations were developed, which highlighted the minimum number of hydrophones in order to obtain sufficient accuracy to observe coherent trajectories (16 seabed hydrophones).

During Summer 2021 only three hydrophones were deployed and working in the KM3NeT-ORCA infrastructure. This number is not sufficient to reconstruct the position of the animals. For this reason, the piezoelectric sensors housed in each DOM were used as a preliminary test. The sensitivity of these receivers is lower with respect to that of the hydrophones and only the most intense clicks are detected. Furthermore, the positioning system is not yet online due to technical problems with one of the acoustic beacons positioned around the detector. For all these reasons the trajectories obtained through the reconstructions are not yet

completely reliable. However, it has been demonstrated, through simulations, that in the near future, when the number of deployed hydrophones will be sufficient, it will be possible to obtain reliable reconstructions of the routes of the sperm whales passing through the area.

The click identification program was applied to the real KM3NeT data showing the periods of presence of dolphins and sperm whales between April 2020 and July 2021, distinguishing night and day acoustic activity.

A statistical study was carried out on the Inter Click Interval (ICI) of the signals emitted by sperm whales and the size of an individual was estimated through the Inter Pulse Interval (IPI) study (see sec. 4.3.4).

The work carried out on the acoustic data of KM3NeT has demonstrated the enormous potential of the infrastructure for the study of marine mammals.

In parallel to this activity, during my PhD, I worked on the analysis of the acoustic data collected in 2019 by the Whalesafe experiment. Through the use of four hydrophones placed in a tetrahedron and lowered to a depth of 70 m in the Ligurian Sea, it was possible to reconstruct numerous routes of sperm whales by exploiting the delay times between the receivers to estimate the arrival angles of the direct acoustic wave and wave reflected from the sea surface. The experience deriving from this study was fundamental to implement the KM3NeT click identification program and to perfect the positioning algorithm.

Finally, given the exceptional presence of killer whales in the port of Genoa during December 2019, some marine campaigns were conducted to collect acoustic data, analysed in order to create a catalog of sounds emitted by killer whales.

The experience within this thesis has shown how in science it is possible to combine studies belonging to very distant fields, creating a synergistic and fruitful relationship.

Acknowledgements

The experience I had during my three years as a PhD student allowed me for the first time to understand the technical and relational complexity of an international experiment. I would like to thank, first of all, Mauro Taiuti and Paschal Coyle, directors of the PhD thesis. A big thank you goes to Marco Anghinolfi and Vincent Bertin, who have followed in a constant and thorough way all the phases of my work with passion and interest. A special thanks goes to Matteo Sanguineti and Vladimir Kulikovskiy, who have continuously contributed with fundamental advices, suggestions and teachings during the whole PhD path. Of fundamental importance was the collaboration with all the members of the Genova KM3NeT group (in particular, in addition to those already mentioned, Alba Domi, Barbara Caiffi and Sandra Zavatarelli), the Marseille KM3NeT group (in particular, in addition to those already mentioned, Alexander Enzenhöfer and Jürgen Brunner), the Catania KM3NeT group (Giorgio Riccobene and Salvo Viola) and the Valencia KM3NeT group (Didac Diego Tortosa). A final thanks goes to the coordinators of the KM3NeT calibration group Robert Lahmann and Dorothea Samtleben.

Bibliography

[1] R. E. Francois and G. R. Garrison. "Sound absorption based on ocean measurements: Part I: Pure water and magnesium sulfate contributions". In: *The Journal of the Acoustical Society of America* 72.3 (1982), pp. 896–907. DOI: 10.1121/1.388170. eprint: https://doi.org/10.1121/1.388170. URL: https://doi.org/10.1121/1.388170.

[2] R. E. Francois and G. R. Garrison. "Sound absorption based on ocean measurements. Part II: Boric acid contribution and equation for total absorption". In: *The Journal of the Acoustical Society of America* 72.6 (1982), pp. 1879–1890. DOI: 10.1121/1.388673. eprint: https://doi.org/10.1121/1.388673. URL: https://doi.org/10.1121/1.388673.

[3] Nicolò Socrate Falzoi. "Studio delle prestazioni di un sistema acustico passivo per il tracciamento del capodoglio nel Mar Ligure". MA thesis. Università degli studi di Genova - Dipartimento di Fisica, 2010.

[4] C. C. Leroy. "Development of Simple Equations for Accurate and More Realistic Calculation of the Speed of Sound in Seawater". In: *The Journal of the Acoustical Society of America* 46.1B (1969), pp. 216–226. DOI: 10.1121/1.1911673. eprint: https://doi.org/10.1121/1.1911673. URL: https://doi.org/10.1121/1.1911673.

[5] Claude Leroy, Stephen Robinson, and M. Goldsmith. "A new equation for the accurate calculation of sound speed in all oceans". In: *The Journal of the Acoustical Society of America* 124 (Dec. 2008), pp. 2774–82. DOI: 10.1121/1.2988296.

[6] S Adrián-Martínez et al. "Letter of intent for KM3NeT 2.0". In: *Journal of Physics G: Nuclear and Particle Physics, 43 (8), 084001, 2016* (). DOI: 10.1088/0954-3899/43/8/084001.

[7] Aaron C. Vincent et al. "Analysis of the 4-year IceCube high-energy starting events". In: *Phys. Rev. D 94, 023009 (2016)* (). DOI: 10.1103/PhysRevD.94.023009.

[8] Xinheng Guo et al. "A Precision measurement of the neutrino mixing angle θ_{13} using reactor antineutrinos at Daya-Bay". In: (Jan. 2007). arXiv: hep-ex/0701029.

[9] F.P. An et al. "Observation of electron-antineutrino disappearance at Daya Bay". In: *Phys. Rev. Lett.* 108 (2012), p. 171803. DOI: 10.1103/PhysRevLett.108.171803. arXiv: 1203.1669 [hep-ex].

[10] F.P. An et al. "New measurement of θ_{13} via neutron capture on hydrogen at Daya Bay". In: *Phys. Rev. D* 93.7 (2016), p. 072011. DOI: 10.1103/PhysRevD.93.072011. arXiv: 1603.03549 [hep-ex].

[11] J.K. Ahn et al. "RENO: An Experiment for Neutrino Oscillation Parameter θ_{13} Using Reactor Neutrinos at Yonggwang". In: (Mar. 2010). arXiv: 1003.1391 [hep-ex].

[12] E. Aslanides et al. "A deep sea telescope for high-energy neutrinos". In: (May 1999). arXiv: astro-ph/9907432.

[13] G. Riccobene et al. *TDR Positioning system for the KM3NeT Telescope*. 2019.

[14] Renata Zukanovich Funchal, Benoit Schmauch, and Gaëlle Giesen. *The Physics of Neutrinos*. 2013. arXiv: 1308.1029 [hep-ph].

[15] Mário João Martins De Angelis Alessandro ; Pimenta. *Introduction to particle and astroparticle physics : questions to the Universe*. Milan: Springer, 2015.

[16] Spurio Maurizio. *Particles and Astrophysics*. Milan: Springer, 2014.

[17] Kohta Murase. "Active Galactic Nuclei as High-Energy Neutrino Sources". In: *Neutrino Astronomy: Current Status, Future Prospects*. Ed. by Thomas Gaisser and Albrecht Karle. 2017, pp. 15–31. DOI: 10.1142/9789814759410_0002. arXiv: 1511.01590 [astro-ph.HE].

[18] Katsuaki Asano and Kohta Murase. "Gamma-Ray Bursts as Multienergy Neutrino Sources". In: *Adv. Astron.* 2015 (2015), p. 568516. DOI: 10.1155/2015/568516.

[19] Kohta Murase, Markus Ahlers, and Brian C. Lacki. "Testing the Hadronuclear Origin of PeV Neutrinos Observed with IceCube". In: *Phys. Rev. D* 88.12 (2013), p. 121301. DOI: 10.1103/PhysRevD.88.121301. arXiv: 1306.3417 [astro-ph.HE].

[20] Rosa Coniglione et al. "KM3NeT Time Calibration". In: *PoS* ICRC2019 (2019), p. 868. DOI: 10.22323/1.358.0868.

[21] Miguel Ardid. "ANTARES: A System of Underwater Sensors Looking for Neutrinos". In: Nov. 2007, pp. 192 –197. ISBN: 978-0-7695-2988-2. DOI: 10.1109/SENSORCOMM.2007.4394920.

[22] Dídac D. Tortosa. "Mechanical Line Fit Model to Monitor the Position of KM3NeT Optical Modules from the Acoustic and Compass/Accelerometer Sensor System Data". In: *Proceedings* 42.1 (2019), p. 33. ISSN: 2504-3900. DOI: 10.3390/ecsa-6-06583. URL: http://dx.doi.org/10.3390/ecsa-6-06583.

[23] Andrea Barberis. "Calcolo del coefficiente di resistenza per un sensore di neutrini posizionato nei fondali marini del Golfo del Leone". MA thesis. Università degli studi di Genova - scuola politecnica, 2019.

[24] C. Guidi. "Simulation of the Performance of the Acoustic Positioning System of the Underwater KM3NeT Neutrino Telescope". In: *2019 Sixth International Conference on Internet of Things: Systems, Management and Security (IOTSMS)*. 2019, pp. 586–590. DOI: 10.1109/IOTSMS48152.2019.8939166.

[25] *iminuit web site*. https://iminuit.readthedocs.io/en/latest/.

[26] *ERDDAP web site*. https://erddap.osupytheas.fr/erddap/tabledap/Emso_Ligure_Ouest_MII_Aquadopp_NetCDF.graph?time,Speed_mean,Direction_std&.draw=markers&.marker=5%7C5&.color=0x000000&.colorBar=%7C%7C%7C%7C%7C&.bgColor=0xffccccff&time%3E=2020-02-01T00:00:00Z&time%3C2020-03-01T00:00:00Z&.timeRange=1,month(s).

[27] *Pelagps Sanctuary web site*. https://www.sanctuaire-pelagos.org/en/.

[28] Daniela Pace, Raffaella Tizzi, and Barbara Mussi. "Cetaceans Value and Conservation in the Mediterranean Sea". In: *Journal of Biodiversity & Endangered Species* S1: (Oct. 2015). DOI: 10.4172/2332-2543-S1-004.

[29] Virginia Sciacca et al. "Annual Acoustic Presence of Fin Whale (Balaenoptera physalus) Offshore Eastern Sicily, Central Mediterranean Sea". In: *PLoS ONE* 10 (Nov. 2015), e0141838. DOI: 10.1371/journal.pone.0141838.

[30] *The voices of marine mammals of the Mediterranean Sea*. http://www-9.unipv.it/cibra/edu_dolphins_uk.html.

[31] Brittany Jones et al. "Sounds produced by bottlenose dolphins (Tursiops): a review of the defining characteristics and acoustic criteria of the dolphin vocal repertoire". In: *Bioacoustics* 29.4 (2020), pp. 399–440. DOI: 10.1080/09524622.2019.1613265. eprint: https://doi.org/10.1080/09524622.2019.1613265. URL: https://doi.org/10.1080/09524622.2019.1613265.

[32] Alexandros Frantzis and Denise Herzing. "Mixed-species associations of striped dolphins (Stenella coeruleoalba), short-beaked common dolphins (Delphinus delphis), and Risso's dolphins (Grampus griseus) in the Gulf of Corinth (Greece, Mediterranean Sea)". In: *Aquatic Mammals* 28 (Jan. 2002).

[33] Bertel Møhl et al. "The monopulsed nature of sperm whale clicks". In: *The Journal of the Acoustical Society of America* 114 (Sept. 2003), pp. 1143–54. DOI: 10.1121/1.1586258.

[34] Bertel Møhl et al. "The monopulsed nature of sperm whale clicks". In: *The Journal of the Acoustical Society of America* 114 (Sept. 2003), pp. 1143–54. DOI: 10.1121/1.1586258.

[35] Linda Weilgart and Hal Whitehead. "Coda vocalizations in sperm whales (Physeter macrocephalus) of the Galapagos Islands". In: *Canadian Journal of Zoology* 71 (Feb. 2011), pp. 744–752. DOI: 10.1139/z93-098.

[36] P. Miller. "Swimming gaits, passive drag and buoyancy of diving sperm whales Physeter macrocephalus". In: *Journal of Experimental Biology* 207 (May 2004), pp. 1953–1967. DOI: 10.1242/jeb.00993.

[37] P Madsen et al. "Sperm whale sound production studied with ultrasound time/depth-recording tags". In: *The Journal of experimental biology* 205 (Aug. 2002), pp. 1899–906.

[38] William A. Watkins and William E. Schevill. "Sperm whale codas". In: *The Journal of the Acoustical Society of America* 62.6 (1977), pp. 1485–1490. DOI: 10.1121/1.381678. eprint: https://asa.scitation.org/doi/pdf/10.1121/1.381678. URL: https://asa.scitation.org/doi/abs/10.1121/1.381678.

[39] Ted Cranford. "Cranford T. W. — The sperm whale's nose: sexual selection on a grand scale? Marine Mammal Science 15". In: *Marine Mammal Science* 15 (Aug. 2006), pp. 1133 –1157. DOI: 10.1111/j.1748-7692.1999.tb00882.x.

[40] Kenneth S. Norris and George W. Harvey. "a Theory for the Function of the Spermaceti Organ of the Sperm Whale (physeter Catodon L)". In: *NASA Special Publication*. Vol. 262. 1972, p. 397.

[41] William K. ; Raven; Henry Cushier Gregory. *The spermaceti organ and nasal passages of the sperm whale (Physeter catodon) and other odontocetes*. New York, NY 10024: American Museum of Natural History, 1933.

[42] Magnus Wahlberg et al. "Click production during breathing in a sperm whale (Physeter macrocephalus)". In: *The Journal of the Acoustical Society of America* 118.6 (2005), pp. 3404–3407. DOI: 10.1121/1.2126930. eprint: https://doi.org/10.1121/1.2126930. URL: https://doi.org/10.1121/1.2126930.

[43] J. C. D. Gordon. "Sperm whale groups and social behavior observed off Sri Lanka". In: *Report of the International Whaling Commission* (1987).

[44] Marcus Rhinelander and Stephen Dawson. "Measuring sperm whales from their clicks: Stability of interpulse intervals and validation that they indicate whale length". In: *The Journal of the Acoustical Society of America* 115 (May 2004), pp. 1826–31. DOI: 10.1121/1.1689346.

[45] W.A. Watkins and W.E. Schevill. "Sperm whales (Physeter catodon) react to pingers". In: *Deep Sea Research and Oceanographic Abstracts* 22.3 (1975), pp. 123–129. ISSN: 0011-7471. DOI: https://doi.org/10.1016/0011-7471(75)90052-2. URL: https://www.sciencedirect.com/science/article/pii/0011747175900522.

[46] Dziedzic A. Busnel R. G. "Observations sur le comportement et les emissions acoustiques du cachalot lors de la chasse". In: *Bocagiana, Museu Municipal do Funchal* 14 ().

[47] Coleman Levenson. "Source level and bistatic target strength of the sperm whale (Physeter catodon) measured from an oceanographic aircraft". In: *The Journal of the Acoustical Society of America* 55.5 (1974), pp. 1100–1103. DOI: 10.1121/1.1914660. eprint: https://doi.org/10.1121/1.1914660. URL: https://doi.org/10.1121/1.1914660.

[48] Linda Weilgart and Hal Whitehead. "Distinctive vocalizations from mature sperm whales (Physeter macrocephalus)". In: *Canadian Journal of Zoology* 66 (Feb. 2011), pp. 1931–1937. DOI: 10.1139/z88-282.

[49] B Møhl et al. "Sperm whale clicks: Directionality and source level revisited". In: *The Journal of the Acoustical Society of America* 107 (Feb. 2000), pp. 638–48. DOI: 10.1121/1.428329.

[50] Javier Tellechea. "Echolocation inter-click interval variation among specific behaviors in free-ranging bottlenose dolphins in coast of Uruguay". In: *Journal of Cetacean Research and Management* 21 (Aug. 2020). DOI: 10.47536/jcrm.v21i1.192.

[51] Lesley Douglas, Stephen Dawson, and Nathalie Jaquet. "Click rates and silences of sperm whales at Kaikoura, New Zealand". In: *The Journal of the Acoustical Society of America* 118 (Aug. 2005), pp. 523–9. DOI: 10.1121/1.1937283.

[52] Violaine Dulau. "Movements of sperm whale in the western Mediterranean Sea: Preliminary photo-identification results". In: *Journal of the Marine Biological Association of the United Kingdom* 87 (Feb. 2007), pp. 195 –200. DOI: 10.1017/S0025315407054860.

[53] Francesco Caruso et al. "Long-Term Monitoring of Dolphin Biosonar Activity in Deep Pelagic Waters of the Mediterranean Sea". In: *Scientific Reports* 7: 4321 (June 2017). DOI: 10.1038/s41598-017-04608-6.

[54] Mike van der Schaar et al. "Acoustics in water: synergies with marine biology". In: *EPJ Web Conf.* 135 (2017). Ed. by S. Buitnik et al., p. 06008. DOI: 10.1051/epjconf/201713506008.

[55] M. André et al. "Sperm whale long-range echolocation sounds revealed by ANTARES, a deep-sea neutrino telescope". In: *Scientific Reports* 7, 45517 (Apr. 2017), p. 45517. DOI: 10.1038/srep45517.

[56] *SciPy.org*. https://docs.scipy.org/doc/scipy/reference/generated/scipy.optimize.least_squares.html.

[57] Walter M. X. Zimmer et al. "Three-dimensional beam pattern of regular sperm whale clicks confirms bent-horn hypothesis". In: *The Journal of the Acoustical Society of America* 117.3 (2005), pp. 1473–1485. DOI: 10.1121/1.1828501. eprint: https://doi.org/10.1121/1.1828501. URL: https://doi.org/10.1121/1.1828501.

[58] P. T. Madsen et al. "Sperm whale sound production studied with ultrasound time/depth-recording tags". In: *Journal of Experimental Biology* 205.13 (July 2002), pp. 1899–1906. ISSN: 0022-0949. DOI: 10.1242/jeb.205.13.1899. eprint: https://journals.biologists.com/jeb/article-pdf/205/13/1899/1240975/1899.pdf. URL: https://doi.org/10.1242/jeb.205.13.1899.

[59] Christophe Laplanche et al. "Male sperm whale acoustic behavior observed from multipaths at a single hydrophone". In: *The Journal of the Acoustical Society of America* 118.4 (2005), pp. 2677–2687. DOI: 10.1121/1.2033567. eprint: https://doi.org/10.1121/1.2033567. URL: https://doi.org/10.1121/1.2033567.

[60] V. Teloni et al. "Consistent acoustic size estimation of sperm whales using clicks recorded fom unknown aspects". In: *Journal of Cetacean Research and Management* (2007). DOI: 10.1121/1.2033567.

[61] A.V. Oppenheim and R.W. Schafer. "From frequency to quefrency: a history of the cepstrum". In: *IEEE Signal Processing Magazine* 21.5 (2004), pp. 95–106. DOI: 10.1109/MSP.2004.1328092.

[62] M. Sanguineti et al. “An automated passive acoustic monitoring system for real time sperm whale (Physeter macrocephalus) threat prevention in the Mediterranean Sea”. In: *Applied Acoustics* 172 (2021), p. 107650. ISSN: 0003-682X. DOI: https://doi.org/10.1016/j.apacoust.2020.107650. URL: https://www.sciencedirect.com/science/article/pii/S0003682X20307544.

[63] Anna Selbmann et al. “A catalogue of pulsed calls produced by killer whales (Orcinus orca) in Iceland 2008-2016”. In: (Apr. 2019).

[64] Frank Thomsen, Dierk Franck, and John Ford. “On the communicative significance of whistles in wild killer whales (Orcinus orca)”. In: *Die Naturwissenschaften* 89 (Oct. 2002), pp. 404–7. DOI: 10.1007/s00114-002-0351-x.